ScuDo
Scuola di Dottorato ~ Doctoral School
WHAT YOU ARE, TAKES YOU FAR

Doctoral Dissertation
Doctoral Program in Structural Engineering (29^{th}cycle)

Progressive collapse induced by fire and blast

From the material characterisation to the structural response

By

Daniele Forni

******

Supervisor(s):
Prof. Dr Bernardino Chiaia, Supervisor
Prof. Dr Ezio Cadoni, Supervisor

Doctoral Examination Committee:
Prof. Dr Mirone Giuseppe, Referee, Università degli studi di Catania
Dr Solomos George, Referee, European Commission - Joint Research Center
Prof. Dr Cornetti Pietro, Politecnico di Torino
Prof. Dr Lacidogna Giuseppe, Politecnico di Torino
Dr Parisi Fulvio, Università Federico II di Napoli

Politecnico di Torino
2017

This page intentionally left blank.

Declaration

I hereby declare that, the contents and organization of this dissertation constitute my own original work and does not compromise in any way the rights of third parties, including those relating to the security of personal data.

Daniele Forni
2017

* This dissertation is presented in partial fulfillment of the requirements for **Ph.D. degree** in the Graduate School of Politecnico di Torino (ScuDo).

This page intentionally left blank.

I would like to dedicate this thesis to my wife and my parents

This page intentionally left blank.

Acknowledgements

I would like to express my sincere gratitude to both my supervisors Prof. Bernardino Chiaia and Prof. Ezio Cadoni for giving me the opportunity to conduct this research under their guidance, recommendations and suggestions. I would like to express my sincere gratitude to Matteo Dotta for his precious collaboration in performing the tests and Gianmario Riganti for his help in interpreting the constitutive model results. I would especially like to thank my family for all of the sacrifices they made on my behalf. I would also like to thank all of my friends who supported me during these three years. Lastly, and most importantly, I would like express appreciation to my wife Mara for her strong support and understanding during the tough moments. All our dreams can come true, if we have the energy to pursue them.

This page intentionally left blank.

Abstract

Comprehensive finite element modelling of key elements is essential to improve the robustness assessment of structures subjected to a coupled effect of fire and blast. Focusing the attention on steel structures, a method for a realistic multi-hazard approach is presented. The problem has been investigated at the material level first and then at the structural level.

The material level was studied performing a detailed experimental investigation in a wide range of strain rates and temperatures. A typical structural steel, namely S355, has been studied. A Split Hopkinson Tensile Bar equipped with a water-cooled induction heating system was used for the mechanical characterisation at high strain rates ($300\,s^{-1}$, $500\,s^{-1}$ and $850\,s^{-1}$) and in a wide range of temperatures (20°C, 200°C, 400°C, 550°C, 700°C and 900°C). A Hydro-Pneumatic machine and a universal electromechanical testing machine were used for intermediate ($5\,s^{-1}$ and $25\,s^{-1}$) and quasi-static ($10^{-3}\,s^{-1}$) strain rate tests at room temperature, respectively. Results showed that the S355 structural steel is strain rate sensitive, keeping its strain hardening capacity with increasing strain rates. The temperature effect was studied by means of the reduction factors for the main mechanical properties. Results at high strain rates highlighted also the blue brittleness phenomenon between 400°C and 550°C.

The link between the material and the structural level is a material constitutive law able to take into account the strain rate sensitivity and the thermal softening. The widely used constitutive law proposed by Johnson and Cook was calibrated using the experimental results. A critical review of this material model highlighted a perceptible variation of the thermal softening parameter at different temperatures. Following a fitting approach, a modification of the dimensionless temperature (T^*) has been proposed.

The structural level was numerically investigated adopting the calibrated material model. Explicit non-linear dynamic analyses of a steel column under fire conditions and followed by an explosion were performed. The commercial code LS-DYNA was used. A method for a realistic multi-hazard approach has been proposed by studying the residual load bearing capacity. The results can be also of great interest to establish the initial conditions that could potentially lead to the onset of progressive collapse in steel framed structures under a combined effect of fire and blast. As expected, the results indicated that the load bearing capacity is influenced by the stand-off distance, the charge size as well as the column boundary conditions. The time of fire loading at which an explosion is triggered is a critical parameter as well.

Contents

List of Figures **xv**

List of Tables **xxi**

1 Introduction **1**

1.1 The engineering motivation 1

1.2 Objectives of this research 5

1.3 Organisation of the manuscript 5

2 Structural robustness to progressive collapse **7**

2.1 Accidental actions 8

2.2 Progressive collapse, approaches and analysis methods 11

2.2.1 Approaches 13

2.3 Research works on progressive collapse 17

2.4 Knowledge gaps and key points in progressive collapse analysis . . 20

2.4.1 Choice of the analytical procedure 20

2.4.2 Influence of choices 21

2.4.3 Structural response under coupled effects 21

2.4.4 Material modelling 22

3 Mechanical characterisation of materials **27**

3.1 Material: the S355 structural steel 28
3.2 Dynamic material testing methods 29
3.3 A brief history 31
3.4 The modified Hopkinson bar for testing at high strain rates 34
3.4.1 Functioning of the Split Hopkinson Tensile Bar 34
3.4.2 Dynamic tests at high temperatures 39
3.5 The Hydro-Pneumatic Machine for testing at medium strain rates . . 42
3.6 Static tests 43

4 Experimental results **45**
4.1 Introduction 46
4.1.1 Mechanical tensile properties 48
4.2 The strain rate influence at room temperature 51
4.3 Mechanical behaviour at high strain rates in a wide range of temperature 55

5 Constitutive model **63**
5.1 Introduction 64
5.2 Johnson-Cook constitutive model 65
5.2.1 Isotropic hardening 66
5.2.2 Strain rate hardening 67
5.2.3 Thermal softening 69
5.2.4 Modification of the thermal softening term 76

6 Blast effects on steel columns under fire loading **79**
6.1 Introduction 80
6.2 Engineering approach 80
6.3 Numerical simulation: a detailed model 82
6.3.1 Model geometry and boundary conditions 82

6.3.2 Axial loading 84
6.3.3 Blast under fire loading 85
6.3.4 Material modeling 90
6.3.5 Validation of the numerical model 91
6.4 Example study 93
6.4.1 Eurocode approach 95
6.5 Results and discussion 97
6.5.1 Comments concerning the strain rate 104

7 Conclusions and future developments 107
7.1 Conclusions 108
7.2 Future developments 111
7.2.1 From the material point of view 111
7.2.2 From the structural point of view 112

References 113

Appendix A Dynamic test results 131
A.1 Results at room temperature 132
A.2 Results at high temperatures 136

This page intentionally left blank.

List of Figures

1.1 Global Terrorism Database World Map: 45 Years of Terrorism. From [6]. 2

1.2 Number of incidents from 1970 to 2015 with explosives, bombs or dynamite. From [6]. 3

1.3 Progressive collapse papers in the last fifty years (from the Scopus database, updated on October 2016). 3

1.4 Levels of investigation. Experimental set-ups (a) for the mechanical characterisation in a wide range of strain rates and temperatures, example of material properties (b) and numerical model (c). 4

2.1 Famous examples of accidental actions. (a) World Trade Center terrorist attacks, New York City, U.S., 11 September 2001. (b) Deepwater Horizon disaster, Gulf of Mexico, U.S., 20 April 2010. (c) Pirelli Tower airplane crash, Milan, Italy, 18 April 2002. 8

2.2 Ronan Point progressive collapse, London (1968). 10

2.3 BASF headquarters disaster (Ludwigshafen, 17 October 2016). . . . 13

2.4 Different ties to provide structural integrity. Image from [7]. 16

3.1 Prismatic sample 7x7 mm cross section and sample after turning. . . 28

3.2 Geometry of the sample. Dimensions in mm. 29

3.3 Metallography. 29

3.4 Microhardness measurements and 2 points of measure. 30

3.5 Kolsky bar original design [117], from [113]. 31

3.6 Bertram Hopkinson's original apparatus, from [118]. 32

3.7 Volterra's split Hopkinson bar apparatus. Figure from [119]. 33

3.8 Schematic of the SHTB used for the mechanical characterisation at room temperature, from [8]. 36

3.9 Incident, reflected and transmitted pulses. 38

3.10 Schematic of the SHTB used for the combined high strain rate and temperature testing, from [9]. 39

3.11 Setup for the high strain rate tests at elevated temperatures, from [9]. 40

3.12 Distribution of the temperature along the whole specimen at 550 $^{\circ}C$, from [9]. 40

3.13 Hydro-Pneumatic Machine used for the characterisation at intermediate strain rates. 42

4.1 Preloading conditions. 46

4.2 Stress and strain rate versus time at 20 °C. 47

4.3 Post-mortem examination of two samples tested at 500 s^{-1}. 50

4.4 Representative stress-strain diagrams at 20 °C. 51

4.5 (a) Y4-S3 Motion Pro Camera and (b) eight frames during the failure process of a sample tested at 850 s^{-1} [8]. 52

4.6 Ductility indexes: (a) $f_u/f_{p,0.2\%}$ ratio and reduction of area at failure and (b) DIFs for ultimate tensile strength and yield strength. 52

4.7 Strain energies in function of the strain rate. 54

4.8 Representative stress-strain diagrams ($\dot{\varepsilon}^* = 300\,s^{-1}$ at 20°C). 55

4.9 Representative stress-strain diagrams ($\dot{\varepsilon}^* = 500\,s^{-1}$ at 20°C). 56

4.10 Representative stress-strain diagrams ($\dot{\varepsilon}^* = 850\,s^{-1}$ at 20°C). 56

4.11 Effective strain rate at increasing temperatures. 57

4.12 Comparison of reflected pulses at increasing temperatures. 57

4.13 Reduction factors for: proof strength (a), ultimate tensile strength (b), effective yield strength at 0.5% (c), 1.0% (d). 59

4.14 Reduction factors for effective yield strength at 2.0% (a), 5.0% (b), 10.0% (c) and 15.0% (d). 60

4.15 Trend of ductility indexes at high temperatures. 61

4.16 Strain energies for different temperatures. 62

5.1 Isotropic hardening fitting model. 67

5.2 Fitting data for the strain rate sensitivity parameter, from [8]. 68

5.3 Example of the Johnson-Cook fit at three different strain rates, from [8]. 68

5.4 Integration interval in Eqs. 5.8-5.9. 70

5.5 Thermal softening parameter evaluated at two different high strain rates. 72

5.6 Johnson-Cook fit at different temperatures and testing conditions. . . 73

5.7 Comparison of the thermal softening factors obtained experimentally, with a fixed single values of m and by applying the proposed modification of the Johnson-Cook constitutive law. 75

5.8 Comparison between the traditional and the modified homologous temperature. 77

5.9 Comparison of the thermal softening factors obtained experimentally (R^*) and the proposed modification of the Johnson-Cook constitutive law (Eq.5.11). 77

6.1 Coordinate system of the (a) FE column model and for the (b) HEB260 cross section (H = 260 mm, B = 260 mm, t_f = 17.5 mm and t_w = 10 mm). 82

6.2 Bucking lengths l_{fi} of columns in a braced frame [70]. 83

6.3 Buckling length for the three column configurations: Fixed-Fixed (left), Fixed-Hinged (center) and Hinged-Hinged (right). 83

6.4 Blast and fire loading timeline. 86

6.5 Time versus temperature curve for an unprotected (4 sides) HEB260 steel section. 87

6.6 Free ideal airblast wave pressure profile. 87

6.7 Distance influence on blast wave. 88

6.8 Blast charge positioning: (a) 3D view of the FE column model and (b) cross section view. 90

6.9 Numerical and experimental horizontal displacement. 92

6.10 Timeline of the numerical simulations. The $N_{b,fi,t,Rd}$ value is selected accordingly to the column configuration (Table 6.1). 95

6.11 Stress versus strain curve for carbon steel at elevated temperatures [70]. 96

6.12 Residual load bearing capacity versus time. Fixed-Fixed column configuration and stand-off distance of 10 meters. 97

6.13 Residual load bearing capacity versus time. Fixed-Hinged column configuration and stand-off distance of 3 meters. 98

6.14 Residual load bearing capacity versus time. Hinged-Hinged column configuration and stand-off distance of 5 meters. 99

6.15 Frames acquired during a numerical simulation (FF, 20kg of eq. TNT at 1 m and 550°C). 99

6.16 Fixed-Fixed ends 102

6.17 Fixed-Hinged ends 102

6.18 Hinged-Hinged ends 103

6.19 Scaled distance range in which blast loads are expected to generate a rate of deformation from $10^2\,s^{-1}$ to $10^3\,s^{-1}$ within steel columns. . 106

A.1 Results in quasi-static conditions (20 °C) 132

A.2 Results at $5\,s^{-1}$ (20 °C) 132

A.3 Results at $25\,s^{-1}$ (20 °C) 133

A.4 Results at $300\,s^{-1}$ (20 °C) 133

A.5 Results at $500\,s^{-1}$ (20 °C) 134

A.6 Results at $850\,s^{-1}$ (20 °C) 134

A.7 Results for preloading condition v_1 (200 °C) 136
A.8 Results for preloading condition v_2 (200 °C) 136
A.9 Results for preloading condition v_3 (200 °C) 137
A.10 Results for preloading condition v_1 (400 °C) 137
A.11 Results for preloading condition v_2 (400 °C) 138
A.12 Results for preloading condition v_3 (400 °C) 138
A.13 Results for preloading condition v_1 (550 °C) 139
A.14 Results for preloading condition v_2 (550 °C) 139
A.15 Results for preloading condition v_3 (550 °C) 140
A.16 Results for preloading condition v_1 (700 °C) 140
A.17 Results for preloading condition v_2 (700 °C) 141
A.18 Results for preloading condition v_3 (700 °C) 141
A.19 Results for preloading condition v_1 (900 °C) 142
A.20 Results for preloading condition v_2 (900 °C) 142
A.21 Results for preloading condition v_3 (900 °C) 143

This page intentionally left blank.

List of Tables

4.1 Testing conditions at high strain rates. 47

4.2 Scheduled tensile test campaign of this research. 48

5.1 Isotropic hardening parameters. 66

5.2 Johnson-Cook thermal softening sensitivity parameters at different temperatures and strain rates. 71

5.3 Parameters for the definition of the dimensionless temperature T_D. . 78

6.1 Constraints, buckling lengths, bucking resistances and critical temperatures. 85

6.2 Indicative charge weight, from [24]. 89

6.3 Indicative TNT equivalent mass factors, from [24]. 89

6.4 Parameters for the Johnson-Cook analysis. 91

6.5 Experimental and numerical comparison. The label "y0" means y-axis (strong axis) pin-ended, while the label "z0" means z-axis (weak axis) pin-ended. 91

6.6 Six analysed configurations: coordinates of the charge. 93

6.7 Parameters for the simplified analysis. 96

6.8 Residual load bearing capacities 100

6.9 Lateral displacement (at mid-height and along the x-axis). 101

6.10 Influence of strain rate in Eq. 6.11 ($c = 0.0247$). 105

A.1 Experimental results at room temperature. 135

A.2 Averaged experimental results ($\dot{\varepsilon}^* = 300\,\mathrm{s}^{-1}$ at 20°C) 144

A.3 Averaged experimental results ($\dot{\varepsilon}^* = 500\,\mathrm{s}^{-1}$ at 20°C) 145

A.4 Averaged experimental results ($\dot{\varepsilon}^* = 850\,\mathrm{s}^{-1}$ at 20°C) 146

Chapter 1

Introduction

1.1 The engineering motivation

In the last years many researchers focused their attention on the behaviour of constructions located in urban habitats and subjected to both natural and/or man-made strong accidental actions, such as for example catastrophic earthquakes, severe fire loadings, gas explosions, wind storms, accidental or malicious impacts against critical infrastructures and, last but not least, blasts due to terrorist attacks (e.g. COST C26 Action, *Urban Habitat Constructions under Catastrophic Events*). Among these accidental actions, the acts of terrorism have increased markedly in the recent decades (Figure 1.1) and consequently the use of explosives by terrorist groups is becoming a growing problem all around the world (Figure 1.2).

Furthermore, it is important to note that an accidental action can be also the triggering cause of more severe actions. For example, the Great East Japan earthquake (Tohoku, 2011) triggered powerful tsunami waves which caused the Fukushima nuclear disaster, or the sadly known 9/11 World Trade Center airplane impacts which caused the complete collapse of the Twin Towers. Consequently, it is quite clear that the simultaneous effect of these actions should be also taken into consideration. Moreover, a common aspect among these severe actions is that these phenomena are characterised by a huge amount of energy which is released in a very short period of time [1, 2]. In other words these are dynamic actions.

In this context, the ability of structural systems to resist damages under extreme loadings has become a widely studied topic (e.g. [3–5]). Consequently, many re-

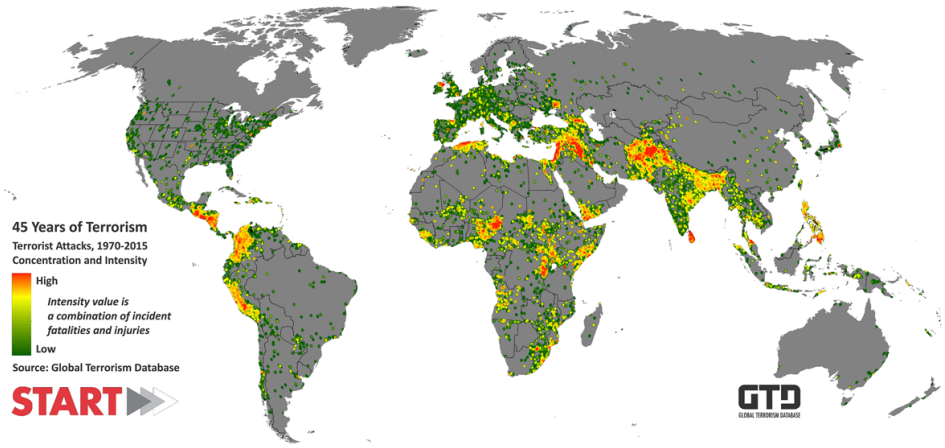

Fig. 1.1 Global Terrorism Database World Map: 45 Years of Terrorism. From [6].

searchers studied how to avoid that the spreading of an initial local failure caused by extreme loadings, results in the collapse of a disproportionately large part of a structure [7]. Starting from the early 1970's this topic, commonly known as *progressive or disproportionate collapse*, has been more and more studied (Figure 1.3). The triggering event, in 1968, was the partial collapse of the Ronan Point building due to a localised internal gas explosion on the 18^{th} floor. However, it is only after the 9/11 World Trade Center tragedy that a remarkable increase of knowledge has been renewed in this field.

This gives evidence that the evaluation of the structural robustness to progressive collapse under extreme loading conditions has become a relevant issue, but some aspects are still open to investigation. In fact, because of the complexity of these phenomena, the structural assessment cannot pass through definite empirical equations. Likewise, full scale tests are almost prohibitively expensive, hardly repeatable and moreover, require too much time. Depending on the level of risk assessment, the structural behaviour under extreme loading conditions is usually studied performing numerical analyses of increasing complexity. But, it is a matter of fact, that, together with the appropriate computational algorithms, a complex numerical simulation strongly depends on how well the material behaviour is implemented.

For these reasons, the present work is aimed at contributing to the improvement of the evaluation of the structural robustness to progressive collapse under the simultaneous effect of two extreme conditions: fire and blast loadings. In particular, focusing the attention on steel structures, the problem is investigated both at the material level and the structural level (Figure 1.4).

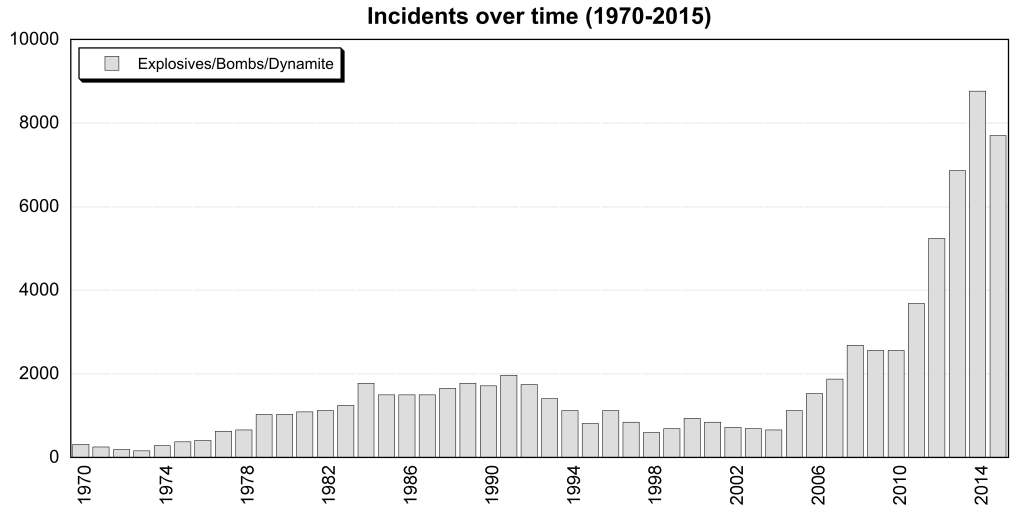

Fig. 1.2 Number of incidents from 1970 to 2015 with explosives, bombs or dynamite. From [6].

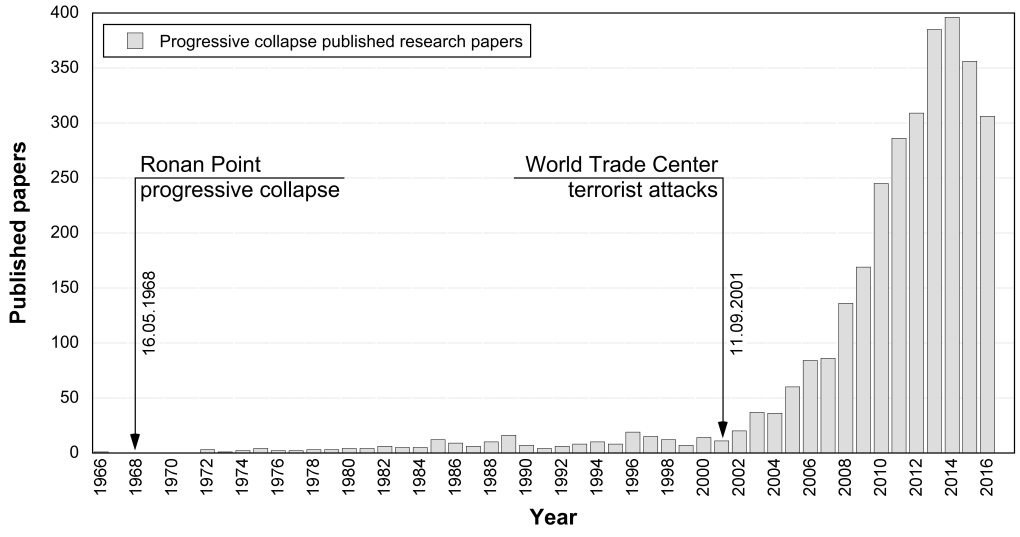

Fig. 1.3 Progressive collapse papers in the last fifty years (from the Scopus database, updated on October 2016).

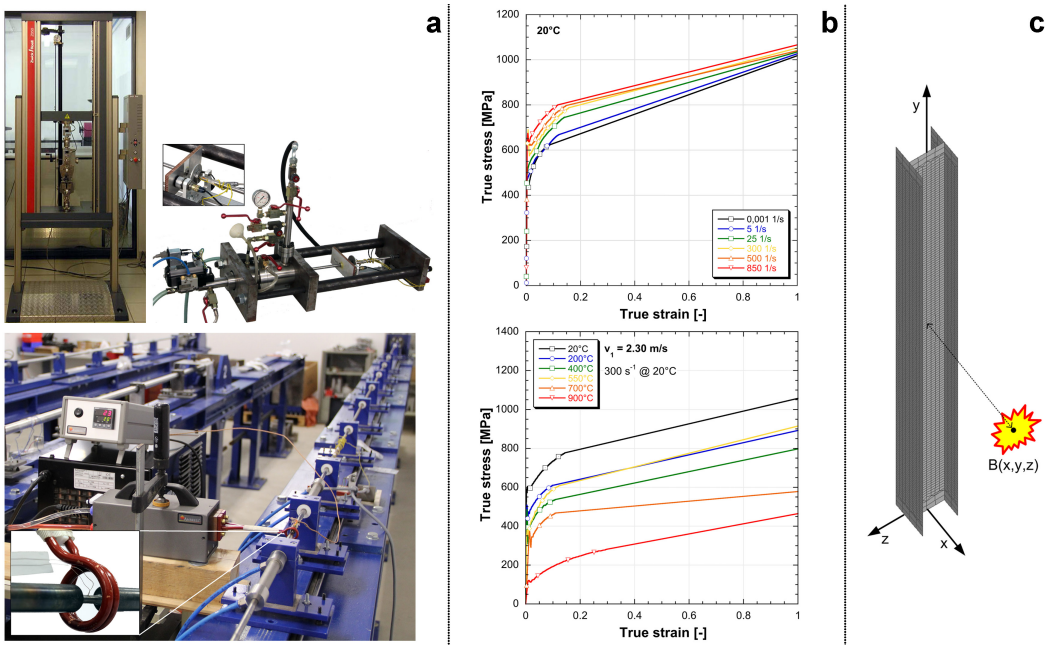

Fig. 1.4 Levels of investigation. Experimental set-ups (a) for the mechanical characterisation in a wide range of strain rates and temperatures, example of material properties (b) and numerical model (c).

The material level is studied performing an experimental investigation in a wide range of strain rates and temperatures of a typical structural steel used in constructions. The dynamic characterisation at high strain rates and in a wide range of temperatures is performed by means of a modified Split Hopkinson (Kolsky) bar equipped with a water-cooled induction heating system. A hydro pneumatic machine and a universal electromechanical testing machine are used for intermediate and quasi-static strain rate tests, respectively.

The structural level is numerically investigated by studying the residual load bearing capacity of steel columns under fire conditions and followed by an explosion. The approach adopts the use of the results obtained at the material level and implemented into a constitutive law able to take into account both the strain rate sensitivity and the thermal softening.

1.2 Objectives of this research

In the framework of this research, the following objectives are to be achieved, which will contribute at the same time to the improvement of the evaluation of the structural robustness to progressive collapse under the simultaneous effect of two extreme conditions.

- By means of a detailed experimental characterisation, evaluate the strain rate sensitivity ($10^{-3}\,\mathrm{s}^{-1} \div 850\,\mathrm{s}^{-1}$) of a typical structural steel.
- Experimental evaluation of the high temperatures influence (up to 900 °C) on the material behaviour at high strain rates.
- Implementation of the experimental results into a reliable and easy to use material constitutive law.
- Perform a detailed numerical simulation in order to evaluate the blast effects on steel columns under fire conditions.
- Evaluate the applicability and the usability of the material model.

1.3 Organisation of the manuscript

The manuscript is arranged in 7 Chapters.

Chapter 1 presents the engineering motivations as well as the objectives of the research.

Chapter 2 introduces the approaches to evaluate the structural robustness to progressive collapse. A special attention is paid to the interaction of two accidental actions: blast and fire loadings. A literature review, the knowledge gaps and the key points in progressive collapse analyses are reported.

Chapter 3 concerns the experimental techniques used to investigate the mechanical behaviour of materials in a wide range of strain rates and temperatures.

Chapter 4 presents the experimental investigation on the S355 low-alloy structural steel in a wide range of strain rates ($10^{-3} \div 850\,\mathrm{s}^{-1}$) and temperatures (20÷900 °C).

Chapter 5 deals with the choice and the description of the constitutive material model able to describe the material properties in numerical simulations of dynamic events at different temperatures.

Chapter 6 presents the study of the residual load bearing capacity of steel columns under fire conditions and followed by an explosion. A single detailed column model is reported. An evaluation of both applicability and reliability of the numerical model is studied by means of a non-linear numerical analysis using the commercial code LS-DYNA.

Chapter 7 summarises the findings, the conclusions as well as the future developments of the research.

In Appendix all the performed test results are reported.

Chapter 2

Structural robustness to progressive collapse

Starting from a brief description on the accidental actions, this chapter introduces the topic of the structural robustness to progressive collapse. Then, the approaches and the analysis methods for the progressive collapse assessment are described. Lastly, focusing the attention on the latest and more significant research works on this topic, the weak points in the progressive collapse assessment are highlighted.

Some parts reported in this chapter are part of two published papers in *Engineering Structures* [8] and in *Materials and Design* [9].

2.1 Accidental actions

During its entire life a structure should be able to withstand any accidental action that may *reasonably* be expected. The term *reasonably* is ambiguous, because it is not thinkable to design structures able to withstand any accidental action (see for example Figure 2.1). However, *the ability of a structure to withstand events like fire, explosions, impact or the consequences of human error, without being damaged to an extent disproportionate to the original cause*, should be ensured. This is the commonly known definition of structural robustness reported on Eurocode 1, Part 1-7 [10]. Other definitions of robustness can be found [11–13], but summarising, the robustness can be described as a desirable property of structural systems which reduces their susceptibility to disproportionate consequences in relation to the initial failure.

How it is possible to take into consideration the accidental actions?

(a)

(b)

(c)

Fig. 2.1 Famous examples of accidental actions. (a) World Trade Center terrorist attacks, New York City, U.S., 11 September 2001. (b) Deepwater Horizon disaster, Gulf of Mexico, U.S., 20 April 2010. (c) Pirelli Tower airplane crash, Milan, Italy, 18 April 2002.

Following an approach proposed by the Eurocode [10], it is possible to recognise strategies based on identified accidental actions and strategies based on limiting the extent of localised failure. If an accidental action was identifiable, its occurrence and its consequence would be easily associated with a certain risk level. Typical identified accidental actions are for example: fire loadings, explosions, earthquakes, impacts, flooding and landslides. On the contrary, strategies based on limiting the extent of localised failure refer to unidentified accidental actions and date back to the seventies as a consequence of the collapse of the southeast corner of the Ronan Point building (London, 1968) [14–16]. After this partial collapse (Figure 2.2), caused by an internal gas explosion on the 18^{th} floor, the building codes were updated by introducing more prescriptive rules. The first rules were reported on the *Building Regulations* (1976). These regulations stated that a building should be constructed so that the structural failure caused by the removal of a member, should be localised to a certain limited area. The requirements, stated in this regulation, were developed in relation to the hazard of an internal gas explosion, prescribing the design of key elements to resist to an overpressure of 34 kN/m^2. Then, the British philosophy has been also extended and used in the current suite of Eurocodes [10].

Another approach for accidental design situations is based on consequence classes [10, 17]. The consequence classes are identified by considering the consequences of failure or malfunction of the structure. Following is the categorisation of consequences classes reported on the EN 1991-1-7, Table A.1 [10]:

Low consequence of failure (CC1) Single occupancy houses not exceeding four storeys. Agricultural buildings. Buildings into which people rarely go, provided no part of the building is closer to another building, or area where people do go, than a distance of 1.5 times the building height.

Medium consequence of failure (CC2a) Five storey single occupancy houses. Hotels not exceeding four storeys. Flats, apartments and other residential buildings not exceeding four storeys. Offices not exceeding four storeys. Industrial buildings not exceeding three storeys. Retailing premises not exceeding three storeys of less than 1000 m^2 floor area in each storey. Single storey educational buildings. All buildings not exceeding two storeys to which the public are admitted and which contain floor areas not exceeding 2000 m^2 at each storey.

Fig. 2.2 Ronan Point progressive collapse, London (1968).

Medium consequence of failure (CC2b) Hotels, flats, apartments and other residential buildings greater than four storeys but not exceeding fifteen storeys. Educational buildings greater than single storey but not exceeding fifteen storeys. Retailing premises greater than three storeys but not exceeding fifteen storeys. Hospitals not exceeding three storeys. Offices greater than four storeys but not exceeding fifteen storeys. All buildings to which the public are admitted and which contain floor areas exceeding 2000 m^2 but not exceeding 5000 m^2 at each storey. Car parking not exceeding six storeys.

High consequence of failure (CC3) All buildings defined above as Class 2a and 2b that exceed the limits on area and number of storeys. All buildings to which members of the public are admitted in significant numbers. Stadia accommodating more than 5000 spectators. Buildings containing hazardous substances and/or processes.

For structures with a low consequence of failure (CC1), no specific consideration is necessary for accidental actions. For structures in CC2a (lower risk group), the

provision of effective horizontal ties or effective anchorage of suspended floors are required. In addition to these provisions, buildings in CC2b (upper risk group) should be checked to ensure that upon the loss of a vertical load bearing element, the building remains stable and any local damage does not exceed a specific limit (e.g. the smaller between the 15% of the floor or 100 m^2). If the notional remove of a vertical load bearing element results in an extent of damage higher than the specific limit, such element is considered a key element. Finally, for structures in CC3 a risk analysis may be required and the use of refined methods such as dynamic nonlinear analysis and interaction between load and the structure should be used.

When the structural robustness needs to be evaluated, the building classification into consequence classes is fundamental to determine the suitable approach as well as the appropriate analysis method. This will be discussed in the next Paragraph 2.2.

2.2 Progressive collapse, approaches and analysis methods

The progressive collapse is a widely discussed topic when the robustness of a structure needs to be evaluated, and even if could be defined *as the spread of local damage from an initiating event, from element to element resulting in the collapse of an entire structure or a disproportionately large part of it*, there is no unique definition of what constitutes a progressive collapse [13, 18, 19, 11].

Historically, the progressive collapse became an important topic in structural engineering design after the partial collapse of the Ronan Point Building (London, 1968), due to an internal accidental gas explosion [15, 14, 16]. During the last decades other buildings were partially destroyed by a progressive collapse, mainly due to terroristic attacks. The most famous are the Hyatt Regency Hotel (Kansas City, 1981), the L'Ambiance Palace (Bridgeport, 1987) and the Murrah Federal Building (Oklahoma City, 1995) [20, 21]. But, it is only after the 9/11 World Trade Center disaster (New York, 2001) that the scientific community dealt with the consequences of a progressive collapse caused by a terroristic attack [22, 23]. As a consequence, an increase of knowledge has been renewed in order to protect existing or new critical infrastructures as well as the civilian population (Figure 1.3).

Nowadays it is a matter of fact that the use of explosives by terrorist groups which target critical infrastructures as well as civilians, is becoming a growing problem all around the world. In addition it is important to note that the explosive devices, the weapons used by terrorists, have become more powerful and smaller in size. This leads to an increased mobility of the explosive materials as well as larger range effects. The consequences of such explosions can be directly related to instantaneous life losses. Furthermore, structural failures might be triggered (e.g. progressive collapse) as well, leading to additional extensive fatalities. As a consequence, the structural response under explosive loads cannot be ignored and a reliable structural design procedure is required [24]. Among the accidental actions, the EN 1991-1-7 [10] is mainly focused on internal gas explosions in structures where gas is burned or regulated or where explosive gases are stored or transported (e.g. chemical facilities, vessels, bunkers, sewage constructions, energy ducts, roads, rails). As stated by Karlos and Solomos [24], among the several informative sources in the open literature [25–28], the most reliable references seem to be some USA military publications [29, 30]. The initial guidance in the complex field of protective design was provided in 1969 with the publication of the technical manual *Structures to Resist the Effects of Accidental Actions* [29]. In this manual, procedures and techniques for determining the blast effects as well as for the design of reinforced concrete structures were given. In addition this manual is periodically updated. Currently, several petrochemical-focused references (e.g. [31]) and several references for blast resistant design (e.g. ASCE 59-11 [32], PDC TR-06-08 [33], UFC 3-340-02 [34]) provide a significant amount of information. However, none of these references require the consideration of thermal loads either before, during or after the blast threat.

Besides the explosions, the common definition of robustness [10] takes undoubtedly into consideration the fire loadings. This because an extended exposure to elevated temperatures may seriously influence the structural performances, leading to possible fire induced progressive collapses [28]. Moreover, it is worth noting that an explosion is defined as a rapid chemical reaction of dust, gas or vapour, which results, in the production of very high temperatures and pressure waves. These high temperatures might be the ignition source of a fire, or vice versa, the high temperatures reached during a fire might be the triggering source of explosions as well. A recent example of a blast induced by a fire took place in BASF headquarters

Fig. 2.3 BASF headquarters disaster (Ludwigshafen, 17 October 2016).

(Ludwigshafen, 17 October 2016). The fire on a supply line led firstly to multiple smaller explosions, and lastly, resulting in the final larger blast (Figure 2.3).

As a result explosions and fire loadings should go hand in hand, or in other words, the interaction of such accidental actions should be considered.

2.2.1 Approaches

It is then a matter of fact that a progressive collapse is a very complex situation, where a complex interplay of large deformations, dynamics and inelastic material behaviour are involved. Then, as also reported by Stylianidis et al. [35], conventional structural analysis needs to be used with care.

Even if the progressive collapse is a widely studied problem, there are numerous sources of uncertainty in the building design process (e.g. model and material approximations, strength and frequency of accidental actions, ...). These sources of uncertainty give rise to risk, and as a consequence, structural systems cannot built to be risk-free.

Among the different approaches to evaluate the structural robustness to progressive collapse, the risk-based methods are mainly used in situations where the traditional design fall outside the normal limits [5]. Moreover, other approaches may be followed. For example Ellingwood et al. [7] in their *best practices* to reduce the likelihood of progressive collapse of buildings, reported and described three methods

ordered by increasing levels of analytical complexity. These methods could be used for buildings with increasing level of risk for consequences of failure to progressive collapse. These techniques are classified as: indirect design methods, specific local resistance (SLR) and alternate load path (ALP) analyses. The last two are commonly known as direct design methods. It is worth noting that the terms *indirect design* and *direct design* were introduced by Ellingwood and Leyendecker [36] in 1978. The main difference between an indirect approach and a direct approach, is that in the first the robustness is assumed, while in the second the robustness is demonstrated [5].

The aforementioned approaches can be grouped as follow:

- risk-based methods,
- indirect design methods, known also as tie-force based design methods[1],
- specific local resistance, known also as key-element design[2],
- alternate load path.

These approaches are common to codes all around the world and are also widely described in the *Review of international research on structural robustness and disproportionate collapse (2011)* [5]. Furthermore, as reported by Formisano et al. [37], when the progressive collapse should be evaluated, the choice among one of the above mentioned methods is suggested by the international codes. A brief description is reported in the following sections.

Risk-based methods

The approaches based on risk-methods are generally adopted for buildings with a high level of risk for consequences of failure (e.g. buildings in consequence class 3). Canisius [38] in the *COST Action TU0601 - Robustness of Structures* described an approach to quantify the structural robustness (e.g. in case of progressive collapse) on the basis of a robustness index. Baker et al. [39] proposed a risk-based robustness

[1]The "indirect design method" is a definition generally adopted in the US, while in Europe is known as "tie-force design method".

[2]The "specific local resistance" is a definition adopted in the US, while in Europe is referred to as "key-element design".

index based on a complete risk analysis, where the consequences are divided into direct and indirect. Frangopol and Curley [40] and Fu and Frangopol [41] proposed a probabilistic robustness index based on probabilities of failure of the structural system for undamaged and damaged structures. Faber et al. [42] proposed a deterministic robustness index based on structural measures. As a consequences a damage strength ratio (DSR), that takes values between zero and one (with larger values indicating larger redundancy), has been defined. Also Knoll and Vogel [43] proposed three different methods for the design of structural robustness, and one of them is based on the probability of occurrence of hazards. Canisius et al. [19] reported that there are two approaches to assess the robustness of a structure. The first is based on practical evaluation methods, while the second is focused on the reliability or risk-based approaches.

Indirect design method

The indirect method is a prescriptive approach because the effects on the structure due to a member loss are not explicitly taken into consideration. This method has been introduced in the early 1970s (*Building Regulations*) after the Ronan Point building collapse (1968). In place of an accurate structural analysis, the designer may adopt prescriptive design rules. These rules should ensure a minimum level of connectivity between the structural components, e.g. providing minimum joint resistance or more commonly using inter-member ties. In Figure 2.4 different types of ties to provide structural integrity are reported. This leads in an enhanced load transfer and an improved degree of continuity among the structural parts of a structure.

Even if it is unquantifiable, in the published literature it is widely recognised that the tie-force methods provide a minimum positive contribution to the structural robustness. This is also confirmed from past events, which demonstrates the good performance of buildings designed following this approach. Some references are reported in [5].

This approach is generally adopted for structures which require a low level of protection (e.g. CC2a Class). This approach is also used for the design of structures in seismic regions.

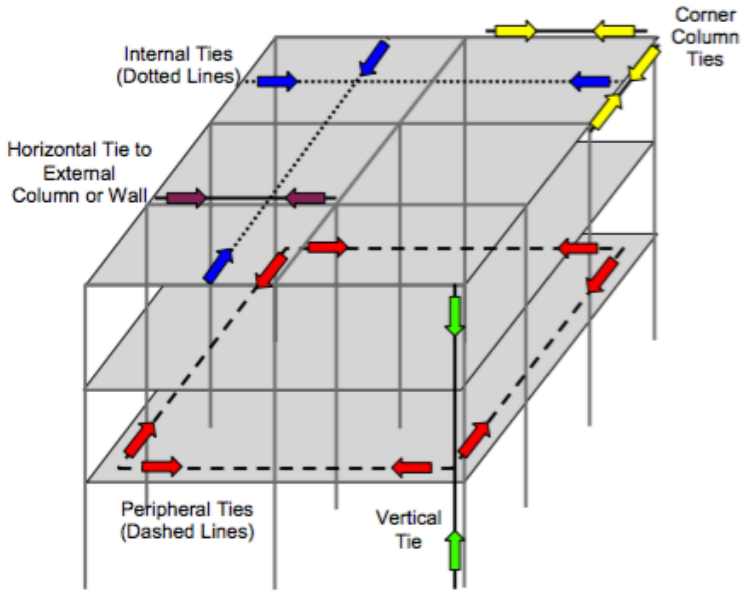

Fig. 2.4 Different ties to provide structural integrity. Image from [7].

Alternate load path

The *alternate load path* (ALP) approach is a direct design method [36]. In case of a member loss (e.g. vertical load bearing element) the designer should check the ability of the whole structural system to find an alternate path, that is to say, if the damaged structure is able to redistribute the loads in order to remain stable. This analysis is generally considered as a threat independent approach because a hypothetical damage state is assumed. In other words, the cause (threat) that leads to the loss of a vertical load bearing element is ignored.

There is a general agreement in the literature (Krauthammer [27], Ellingwood et al. [7]) that this approach is a representative and widely applicable scenario that can be applied to develop an adequate level of robustness.

The *alternate load path* approach has been the subject of considerable study at Imperial College London (Stylianidis et al. [35], Stylianidis and Nethercot [44], Stylianidis et al. [45], Vlassis et al. [46], Izzuddin et al. [47]).

Key-element design

The *key element design* is a direct design method [36] in which the designer needs to perform sophisticated structural analyses to evaluate the effect of abnormal loading events. This approach, known also as *specific local resistance*, is generally used as method of last resort, where the robustness cannot be assessed by other analyses.

This method should be adopted for Class 2B structures when the *alternate load path* design can not assure an adequate redistribution of loads. This is the case where the floor area at risk of collapse exceeds a fixed amount[3]. The *key element design* should be used also for Class 3 structures. In this case, following the approaches based on risk-methods, the critical elements essential for the stability of the structural system should be identified, e.g., ground floor columns. These elements should be designed as *key element*.

Any critical element should be designed to sustain the effect due to an accidental action. As a consequence this method is considered as a *threat specific approach*. In other words, the cause (threat) that triggers a progressive collapse should be taken into consideration. A notional load of 34 kN/m^2 is generally adopted.

2.3 Research works on progressive collapse

The 9/11 events triggered (Figure 1.3) a lot of research works on progressive collapse of steel framed structures, ranging from energy-based to experimental, analytical and computational approaches.

In his book Krauthammer [27] reported an in-depth overview of progressive collapse mitigation approaches as well as a robustness-oriented design. Szyniszewski and Krauthammer [48] presented an energy-based progressive collapse assessment of multi-storey buildings, focusing their attention on the role of the energy flow. Szyniszewski [49, 50] showed also the importance of the deformation energy during progressive collapses. Furthermore, energy considerations are also the main criteria in the field of the controlled demolitions in order to plan the sequence of detonations as well as the weight of explosives. Lew et al. [51], studied the vulnerability of structures to disproportionate collapses. The authors performed an experimental

[3]The smaller value between 100 m^2 or 15% of the floor area [10].

study of two full-scale beam-column assemblies with two types of moment resisting connections to define their response characteristics under a column removal scenario. Sadek et al. [52] performed a computational investigation of the same beam-column assemblies considered by Lew et al. [51], finding a good agreement between experimental and numerical results. Liu et al. [53] performed an analytical study of the forces generated in steel framed structures during a progressive collapse. The authors focused their attention on the overall structural behaviour as a function of the removal rate of a supporting element in the range between 1 s to 1 ms. It has been demonstrated that the rate of the column removal affects the response of the frame when the removal time is between 1 s and 10 ms. When the column removal rate reaches 10 ms, the final results do not differ much from the 1 ms case. This can lead to the conclusion that a static method to predict the structural performance is not a suitable approach. In the last years the researchers of the Imperial College, paid specific attention to progressive collapse. For example Izzuddin et al. [47] proposed a simplified approach for progressive collapse assessment of multi-storey building structures considering a sudden column loss as a design scenario. Then, Vlassis et al. [46] demonstrated the applicability of the approach by means of a case study. More recently, Stylianidis and Nethercot [44], Stylianidis et al. [45, 35, 54] proposed a simplified analytical model for describing the nonlinear static behaviour of beams subsequent to notional column removal. The advantage of this simplified model makes it suitable for rapid parametric studies. Kwasniewski [55] studied the progressive collapse of a multi-storey building by means of a dynamic procedure, neglecting the strain rate effects. Grierson et al. [56] used a nonlinear quasi-static procedure to evaluate a progressive collapse, while Kaewkulchai and Williamson [57] demonstrated that a static analysis may not provide a conservative estimate of collapse.

In the last decades, a significant amount of research has been also carried out to assess the structural robustness in case of fire induced progressive collapse of steel structures. Liew et al. [58] proposed different methodologies of advanced analysis techniques for studying the large-displacement inelastic behaviour of building frames subjected to localised fire. Fang et al. [59] presented the key issues that should be addressed in the robustness assessment of steel-composite structures subjected to localised fire and proposed robustness assessment approaches that offer a practical framework for the consideration of such issues. Fang et al. [60] presented also a simplified energy-based robustness assessment approach, based on a Temperature

Independent Approach (TIA) where the core idea was a sudden column loss (typically employed for blast loading) and in which the maximum temperature is assumed to be unknown. Sun et al. [61] developed a robust static-dynamic procedure to model the dynamic and static behaviour of steel buildings during both local and global progressive collapse under fire conditions. Kucz et al. [62] demonstrated that the boundary conditions play an important role in describing the real behaviour of elements under fire conditions. Porcari et al. [63] in their extensive literature review of the mechanisms involved in fire induced progressive collapse of steel building structures, concluded that the robustness is influenced also by the durability of fireproofing when subjected to blast or other sources of stress. Jiang et al. [64] conducted a parametric analysis to study the possible progressive collapse mechanisms of planar steel frames when one column fails under elevated temperature.

Other authors have tried to study the combined effect of fire and blast. Izzuddin and Fang [65] and Izzuddin et al. [66] made one of the first attempt to perform an integrated fire and blast analysis. Chen and Liew [67] have proposed an approach to analyse steel frame structures subjected to a localised explosion and followed by fire. Liew [68] has introduced a numerical model for analysing steel frame structures subjected to localised damage caused by blast load and subsequently investigating their survivability under fire attack. In this research the strain rate effect due to blast load is taken into consideration by multiplying the static strength by dynamic increase factors [69], while for the temperature effect, the strength and stiffness reduction curves of steel at elevated temperatures [70] have been considered. Song et al. [71] and Izzuddin et al. [66] considering both the strain rate and the temperature effects proposed and verified a method for integrated analysis of steel frames subjected to explosion followed by a fire loading. Ding et al. [72] have presented a numerical model for the prediction of the integrative damage of steel columns subjected to blast loading and followed by fire. Seif et al. [73], with the intention to gain better understanding into the behaviour of moment connections under fire loading, performed FE analysis considering both geometric and material nonlinearities. Seif et al. [73] in their simulations implemented temperature-dependent materials for different types of steels used in connections.

2.4 Knowledge gaps and key points in progressive collapse analysis

The evaluation of the structural robustness to progressive collapse is strongly influenced by different aspects [8]. Some of the most important will be discussed below.

2.4.1 Choice of the analytical procedure

As a matter of fact, the progressive collapse is a dynamic event and a dynamic event require a dynamic analysis. For that reason, the analytical procedure that can be used to model the problem plays a key role. Four different approaches can be adopted by means of linear static (LS), non-linear static (NLS), linear dynamic (LD) or non-linear dynamic analyses (NLD). In the last decades a significant amount of research has been carried out by using different analytical procedures. For example, Marjanishvili and Agnew [74] explained four methods (LS, NLS, LD and NLD) used to perform progressive collapse analyses. Fu [75] analysed a 20-storey 3D structure by means of a nonlinear dynamic analysis. Powel [76] compared different type of analysis (LS, NLS and NLD) finding that a static approach can lead to very conservative results. On the contrary, Kaewkulchai and Williamson [57] demonstrated that a static analysis may not provide a conservative estimate of collapse. Kokot et al. [77] starting from an investigation on a real-scale reinforced concrete flat-slab frame building, performed at first a linear static analysis. Then, in order to account for severe dynamic effects occurring during fast dynamic events, linear and non-linear dynamic analyses were performed.

Even if simplified assumptions are made the most accurate and rigorous approach for evaluating progressive collapses is through the use of an explicit nonlinear dynamic (NLD) procedure. Another approach that can be followed is based on the employment of discrete element method (DEM) models. An extensive research in this field has been performed by Masoero et al. [78–80] that demonstrated the DEMs applicability to progressive collapse by simulating the behaviour of 2D and 3D framed structures after sudden damage.

2.4.2 Influence of choices

A commonly used design scenario for progressive collapse assessment is based on a sudden column loss hypothesis. In other words the progressive collapse analysis it is considered as threat independent, meaning that the cause that triggers the bearing element failure is not considered. Even if this is a weak point of this approach, is generally considered a suitable way to provide an adequate level of robustness. This is the approach adopted in the Alternate Load Path analyses.

On the other hand, following a threat specific approach (e.g. key element design), the critical elements essential for the stability of the structural system should be identified and designed to sustain the effect of an accidental action. As stated on the EN 1991-1-7 [10] each critical element should be capable of sustaining an accidental design action of 34 kN/m^2. But, it is worth noting that this load is not a specific overpressure resulting from a real situation such as a dynamic load due to the blast pressure following an explosion. This is undoubtedly a weak point of this approach. Following a more rigorous approach each critical element should be designed to sustain gravity loads after being subjected to one or more real extreme loading.

2.4.3 Structural response under coupled effects

Only after the 9/11 tragedy the international community raised significant questions on fire safety and on disproportionate collapses as a result of local failures due to accidental actions (e.g. impacts or blasts). In the last fifteen years some authors [65, 71, 66, 81, 67, 68] have studied the influences of blast loading on the fire resistance of steel frames or steel elements. However, as highlighted by some authors [68, 82, 83], in many of these studies only uncorrelated effects of high temperatures and dynamic loadings have been considered. For example Song et al. [71] considered the effect of dynamic loads followed by fire loading, and not acting at the same time. Only recently a numerical method to study the response of steel beams and steel tubular columns has been introduced by Xi et al. [82] and Xi [83]. However, the structural response under the coupled effect of fire and explosion loadings has still more criticisms open to investigation.

One of the reasons is the great difference in the structural and material behaviour under fire and explosion loadings. As stated by Liew et al. [81] the short duration of

the explosion loadings implies that the material should be strain rate sensitive. In fact, blast pressure loads generally produce high strain rates within structural elements. Typical strain rates during blast events are in the range between 10^2 s^{-1} and 10^3 s^{-1} [84]. Moreover, the fire loading is an event of longer duration and is associated with elevated temperatures. This leads to a significant strength deterioration in the mechanical properties. In addition, if the problem is coupled, e.g. a fire loading followed by an explosion, the thermal material properties should be coupled with the strain rate material properties. In other words, the real material properties at high strain rates and in a wide range of temperatures are required. Furthermore, a material constitutive law able to take into account both the strain rate sensitivity and the thermal softening is necessary. The need for material properties and performance during and after the fire is also among the known gaps stated on the *International R&D Roadmap for Fire Resistance of Structures* [85].

2.4.4 Material modelling

The reliability of a structural analysis, apart from the appropriate computational algorithms, strongly depends on how well the material behaviour is captured [7] and, as a consequence, by the choice of the material constitutive model.

The importance of an adequate modelling of the material behaviour under high strain rates and elevated temperatures has emerged clearly during a series of recent collapses. An example is the Kobe earthquake (Japan, 1995) which originated a "domino effect" in oil refineries putting into evidence the crucially different behaviour of different classes of steel used, e.g. for X-cross reinforcement and columns of LNG Horton spheres first subjected to dynamic loading and then to blast and fire. Another and sadly famous example, is the surprisingly rapid vertical collapse of the World Trade Center towers (New York, 2001). This collapse showed the peculiar high-strain rate behaviour of 14-in. steel box columns (mild steel with $f_y = 36$ ksi) subjected to hammer-like loading after heat collapse of the airplane-struck floors.

Also in the controlled demolition field the knowledge of the material behaviour under high loading rates could be of great importance [86]. This because a common way to achieve the desired end of a structure, is to plant explosives at critical points. But not always a planned failure can be a failure itself. An example is the controlled demolition planned for removing the obsolete main spans of the old Cooper River

bridges (Charleston, 2005) [87]. The planned failure with explosives failed to go as planned. As a result, one large portion of the superstructure was left intact and this led to a delay in order to recover all the steel out of the river.

In addition, the detailed knowledge of the high strain rate and high temperature properties of structural steel can be of great interest, e.g., in forensic investigations where the appearance of damage can witness the dynamics of the explosions and fire. As an example, on December 28, 2014, a strong fire occurred in two garage decks of the Italian motorship Norman Atlantic during navigation in the Adriatic Sea. Relatively high temperatures were attained especially in the open deck, and local explosions of inflammable truck content caused high strain rates upon the structural steel grids. The structure was severely damaged, however, an overall robust behaviour was observed. Only the material properties at high strain rates and in a wide range of temperatures can explain the resilient response under the coupled effect of local dynamic events triggered by high temperatures.

Outlook of the structural steel properties at high strain rates and at elevated temperatures

It is obvious that the evaluation of a progressive collapse of steel structures subjected to a combined effect of fire and blast, needs the real mechanical properties at elevated temperatures and in a wide range of strain rates.

The material properties at elevated temperatures can be assessed by two different methods [88], namely steady-state and transient-state. In the steady-state test, that is an isothermal process, the specimen is brought into thermal equilibrium at a predefined temperature and then loaded until it fails keeping the same temperature. On the other hand, in the transient-state test, that is an anisothermal process, the specimen is under constant load while the temperature is increased at a given heating rate.

Low-carbon mild steels (S235, S275, S355) are commonly used as a major structural material in the building construction field [89]. Moreover, in the last years also the use of High Strength Steels - HSS (S460 and S690) and Very High Strength Steels - VHSS (S960) is increasing. But the material properties of these steels at different temperatures have been investigated mainly in quasi static conditions. For example, Outinen et al. [90] tested in quasi-static conditions the structural steel S355

at elevated temperatures by using the transient-tensile test method and reported three equations in function of the temperature for the elastic modulus, the proportional limit and the yield stress. The same authors [91] tested in the same conditions three additional structural steels by using different heating rates. They found that the highest heating rate gives the higher strength properties. In this technical report [88] guidance is given on available, but uncorrelated, elevated temperature and high strain rate material property data, referring to high strength steels used specifically for offshore structures. Yan et al. [92] investigated in quasi static conditions the mechanical properties of a normal mild steel and a high strength steel (S690) between $-80\,^{\circ}\mathrm{C}$ and $30\,^{\circ}\mathrm{C}$. Chen et al. [93] tested at high temperatures and in quasi-static steady and transient state modes two different materials, the BISPLATE80, similar to the S690 structural steel and the XERPLATE Grade 350. They reported the thermal reduction factors for the main mechanical properties and compared them with some current standards [70, 94]. Heidarpour et al. [95] studied in steady-state conditions the quasi-static tensile behaviour of a Very High Strength steel at elevated temperatures. Qiang et al. [96, 97] performed quasi static tests on specimens from three structural steels (S960, S690 and S460) after cooling down from temperatures up to $1000\,^{\circ}\mathrm{C}$, finding that the post-fire performances were correlated with the steel grade. The same authors [98], using both steady and transient state methods at temperatures ranging from $20\,^{\circ}\mathrm{C}$ to $700\,^{\circ}\mathrm{C}$, carried out experimental quasi-static characterisation of the S690 structural steel. They obtained the reduction factors at different temperatures for the elastic modulus as well as for the yield strength at various strain levels and the ultimate tensile strength, finding a good agreement with the data proposed by AISC [99] and Eurocode 3 [70]. Mirmomeni et al. [100] studied the post-impact fire properties of Grade 350 steel. Firstly, different damage levels were introduced (at medium strain rates, $10\,\mathrm{s}^{-1}$). Subsequently, the partly damaged specimens were subjected to steady-state quasi-static tensile loading in a wide range of temperatures ($20\,^{\circ}\mathrm{C}$ to $600\,^{\circ}\mathrm{C}$). The same authors studied also the mechanical properties, the microstructure evolution and the fracture behaviour of structural mild steel subject to the multi-hazard loading scenario of post-impact-fire [101].

Only in few studies the influence of strain rate and temperature were considered as a combined effect. For example Krabiell et al. [102] set the temperatures between $-196\,^{\circ}\mathrm{C}$ and $20\,^{\circ}\mathrm{C}$ while the strain rates between 10^{-4} and $100\,\mathrm{s}^{-1}$. Knobloch et al. [103] tested in steady state conditions the influence of the strain rate ($1.67\cdot$

$10^{-5} \div 1\,s^{-1}$) on the material properties of the S355 structural steel. Børvik et al. [104] studied the combined effect of high strain rates, elevated temperatures (100 °C to 500 °C) and stress triaxiality of a structural steel (Weldox 460E). It was found that the influence of temperature on the stress strain behaviour differs at high strain rates compared with the quasi-static conditions. Moćko et al. [105] studied the mechanical behaviour of selected Polish structural steels (St0S, St3SX, 18GS and 34GS), concluding that the viscoplastic characteristics depend on both temperature and strain rate. Solomos et al. [106] performed an experimental campaign (tensile tests) to investigate the strain rate ($0.001 \div 300\,s^{-1}$), the temperature (20 °C, 400 °C and 600 °C) and size effects in three nuclear steels. Results showed the degrading influence of temperature as well as the strain rate effects on the mechanical properties at elevated temperatures.

One of the most thorough work is reported on the NIST Technical Note 1714 [107], where a model to represent the mechanical behaviour of structural steels is reported. This model is based on combination data from the WTC collapse investigation and other literature sources. The final form of the stress strain model takes into consideration the temperature effect, the strain rate sensitivity, the elastic modulus as well as the strain hardening behaviour. A summary of the literature data on the high-temperature stress strain behaviour is also reported.

Finally, to conclude, there is a scarcity of full stress-strain data sets for structural steels under the coupled effect of elevated temperatures and high strain rates, and this need is attempted to be remedied in this work.

This page intentionally left blank.

Chapter 3

Mechanical characterisation of materials

With the purpose of studying the mechanical properties of a typical structural steel, this Chapter is concerned with the experimental techniques used to investigate the mechanical behaviour in a wide range of strain rates and temperatures.

Firstly, a brief description of the material studied in this research is given. Secondly, an appropriate brief history [108] on the *Kolsky bar* and its modifications is presented [109–113]. Then, a brief exposition of the experimental techniques used to study the dynamic behaviour of the materials is reported. In particular, the mechanical characterisation at high strain rates and in a wide range of temperatures was performed by means of a Split Hopkinson Tensile Bar (SHTB) equipped with a water-cooled induction heating system. Furthermore, with the intention of studying the strain rate sensitivity at room temperature, a Hydro-Pneumatic Machine (HPM) and a universal electro-mechanical testing machine were used for the characterisation at intermediate strain rates and in quasi-static tensile conditions, respectively.

Some parts reported in this chapter are part of two published papers on *Engineering Structures* [8] and on *Materials and Design* [9].

3.1 Material: the S355 structural steel

The material studied in this research is the S355 [114] low-alloy structural carbon steel, widely used in the construction field due to its good strength characteristics as well as good welding properties. This material is also widely used in other applications, such as for example bridge components, offshore structures, power plants, mining applications and tower components.

At room temperature and in quasi-static conditions, the nominal tensile properties of this steel are: elastic modulus 205 GPa, yield strength 355 MPa and ultimate strength 510 MPa. The capital letter S, preceding the nominal yield strength, identify the structural steel.

The specimens for the mechanical characterisation were obtained in the longitudinal direction from a hot-rolled wide-flange section HE. Starting from the initial section geometry and with the purpose of avoiding any influence of the machining operations, wire electrical discharge machining (WEDM) was used in order to obtain small prismatic samples with 7x7 mm cross section (Figure 3.1). These small samples were then turned in order to obtain the usually adopted geometry for dynamic testing, consisting of round samples with 3 mm in diameter and 5 mm of gauge length (Figure 3.2). This peculiar geometry was specially designed for the dynamic tests with the Hopkinson apparatus, and allows the comparison of the full stress strain data obtained using different apparatus [115].

It is worth noting that the S355 structural steel in HE sections can be considered an isotropic material, and for that reason there is no need to check the mechanical

Fig. 3.1 Prismatic sample 7x7 mm cross section and sample after turning.

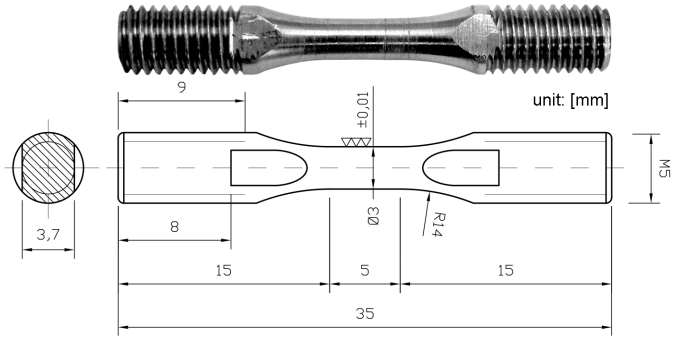

Fig. 3.2 Geometry of the sample. Dimensions in mm.

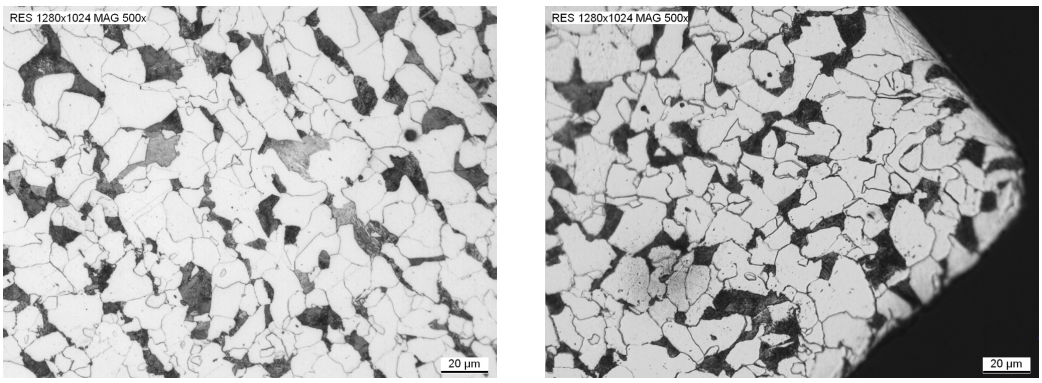

(a) Midsection (b) Border

Fig. 3.3 Metallography.

properties in the transverse direction and also that there is no need to do any compression tests. However, the uniformity of the material properties within the whole section was verified by means of a metallography in different points of the section (see an example in Figure 3.3) and micro-hardness measurements by using a Gnehm Vickers hardness tester. In Figure 3.4 it is possible to observe that the Hardness Vickers HV5 is mainly constant within the measurement points, confirming the uniformity of the material properties within the whole section.

3.2 Dynamic material testing methods

The material properties such as the elastic modulus, the yield strength, the ultimate tensile strength and uniform strain, as well as the fracture strength and strain are generally obtained under quasi-static loading conditions. But, when a structure is

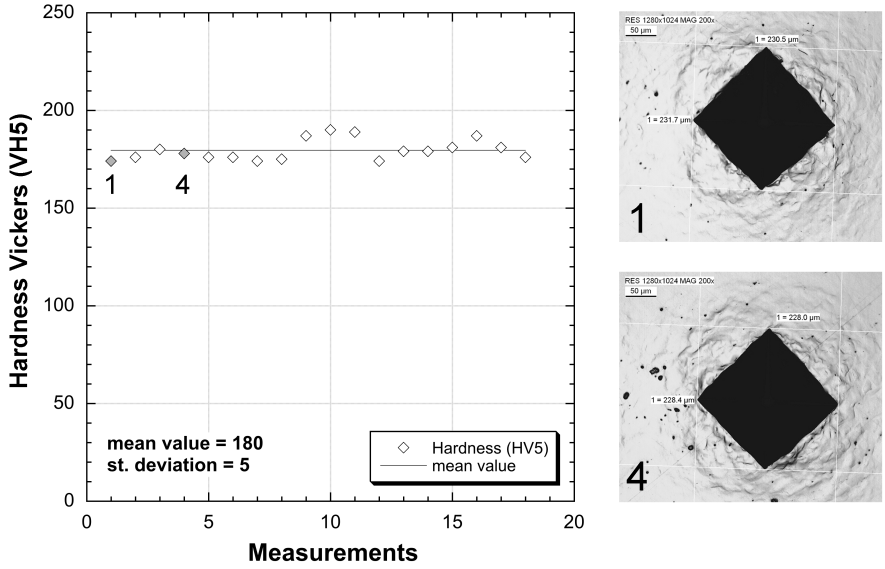

Fig. 3.4 Microhardness measurements and 2 points of measure.

subjected to impulsive loads, such as for example explosions, impacts, earthquakes or progressive collapses, the energy does not act immediately on all parts of the structure. This is because the impulsive loads propagate through the structures, or some part of them, like stress and strain waves. Moreover, the stress waves are propagated at high strain rates through the structure, giving rise to microstructure changes different from those taking place in quasi-static conditions [116].

To perform a safe design of a structure, engineers should take into consideration these phenomena in order to decide an adequate testing method. Therefore, a dynamic material testing method assuring results of high precision must be used in order to ensure product quality and reliability under impact conditions such as those encountered in the vehicle collision, impact, explosion as well as during a progressive collapse.

To obtain a dynamic response of materials under laboratory controlled conditions, Kolsky [117] proposed a very cleaver solution. Instead of direct impact on the specimen (e.g. the effect produced by hammer impact corresponding to a dynamic events commonly encountered in engineering applications), he placed two elastic rods on both sides of the specimen and then struck one of the rods with an explosive blast. In Figure 3.5 is reported the schematic of this concept. The elastic rod between the external impact and the specimen is called the incident bar (or “the input bar”) and the rod on the other side is called the transmission bar (or “the output bar”).

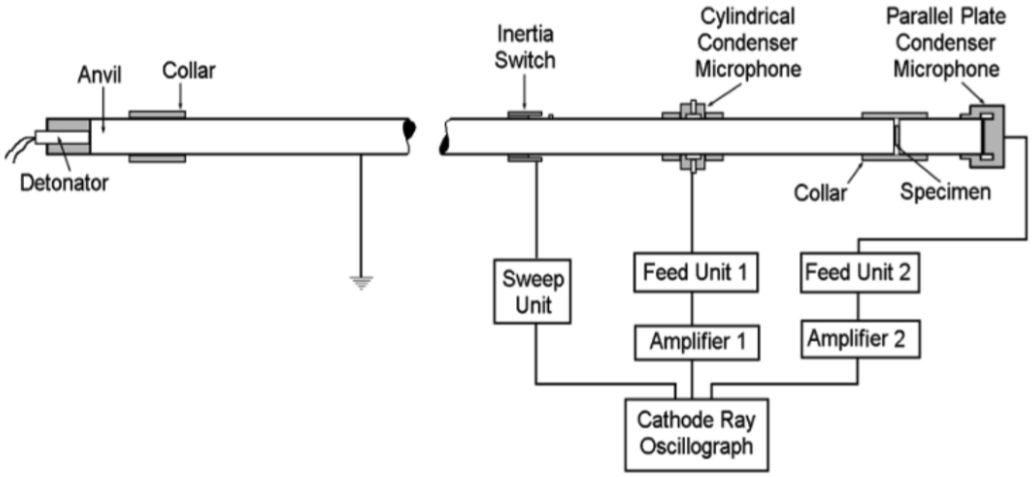

Fig. 3.5 Kolsky bar original design [117], from [113].

Under this arrangement the impact event is controllable and quantitative, and as a consequence, repeatable. The functioning is very simple: when the incident bar is loaded by external impact, a compressive stress wave is generated. When the wave arrives at the interface between the incident bar and the specimen, part of the wave is reflected back into the incident bar and the rest is transmitted through the specimen into the transmission bar. By means of laboratory instrumentations it is possible to record the stress waves in the incident bar propagating towards the specimen and being reflected back from the specimen and the wave in the transmission bar. Further analysis on the waves recorded in the impact event results in information regarding the loading conditions and deformation states in the specimen. Since it was first introduced by Kolsky in 1949, this system has been called the Kolsky bar or, as it will be explained in the following paragraph, a split-Hopkinson pressure bar (SHPB). The original version of the Kolsky bar is for dynamic compression experiments, while versions for other stress states, such as tension, torsion, biaxial, triaxial, and axial/shear combination, have been developed in the past decades.

3.3 A brief history

The original setup of the well known *Kolsky bar* owes its name to Herbert (Harry) Kolsky (1917-1992) who, in 1949, designed the first compression version. But, this apparatus is also widely called *split-Hopkinson pressure bar (SHPB)* in memory of

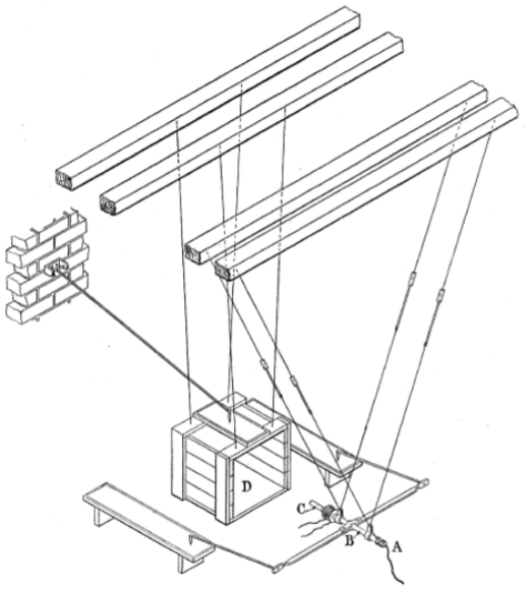

Fig. 3.6 Bertram Hopkinson's original apparatus, from [118].

John Hopkinson (1849-1898) and his son, Bertram (1874-1918). In the following paragraphs the reasons and a brief historical report are explained.

In 1872 John Hopkinson conducted a pioneering work, performing rupture tests of an iron wire by the impact of a drop weight. Even if this experiment reveals the propagation of stress waves in the wire, in the 19^{th} century it was very challenging to measure stress wave propagation. On the other hand, his son Bertram in 1914 [118], introduced a momentum trapping technique whereby the shape of the pressure-time pulse produced by an explosion or by the impact of a bullet could be approximately determined due to the very limited measurement techniques at that time. In Figure 3.6 the Bertram Hopkinson's original apparatus is reported.

In 1946 Taylor [120] was the first to mention the use of Hopkinson pressure bar as a method of measuring the mechanical properties of soft materials (plastics and rubbers) in compression, while the apparatus, consisting of two Hopkinson bars supported by strings, was designed by Enrico Volterra [119], whose schematic is reported in Figure 3.7.

Davis in 1948 [121], with the intention of measuring the pressure-time curves produced by a detonation or a bullet impact, conducted a critical study of the Hopkinson's technique by using parallel plate and cylindrical condenser microphones

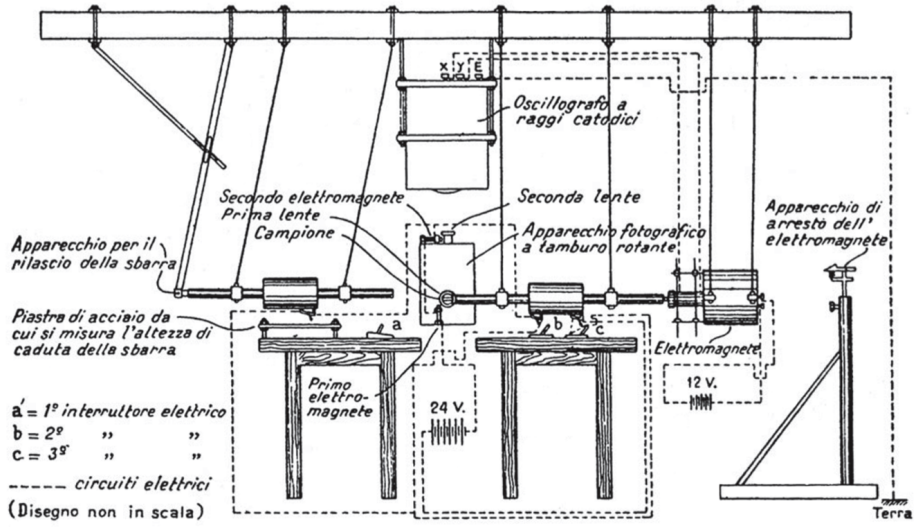

Fig. 3.7 Volterra's split Hopkinson bar apparatus. Figure from [119].

to electrically measure the axial and radial movements of the bar loaded by a detonation.

The pendulum arrangement proposed by Volterra [119] for measuring the dynamic properties of polymers and rubbers was not able to produce stresses large enough to deform metals. For that reason Kolsky in 1949 [117] designed a split-bar system that was dynamically loaded at one end using a detonator (Figure 3.5). Kolsky was the first person to extend the Hopkinson bar technique to measure stress-strain response of materials (polythene, natural and synthetic rubbers, polymethyl-methacrylate, copper and lead) under impact loading conditions.

During the first years after the Kolsky bar was developed, several authors proposed improvements and updated versions. In 1954, Krafft *et al.* [122] applied strain gauge technique to the Kolsky bar to measure the stress waves. The same authors [122], with the intention to generate a repeatable impact stress pulse and because an alternative method to detonators was needed, used a gas gun (typically called *striker bar*) to launch a projectile rod against one end of the incident bar. As a result, repeatable trapezoidal shaped pulses were generated. Finally, in 1964, Lindholm [123] incorporated most of the previous improvements and presented an updated version of the Kolsky bar for valid dynamic characterisation, becoming a popular template of Kolsky bars in laboratories around the world [113].

3.4 The modified Hopkinson bar for testing at high strain rates

The original Hopkinson (Kolsky) bar has been designed and generally used for high strain rate compression tests [118, 121, 117, 123]. An updated version of the original Hopkinson (Kolsky) bar was developed at the Joint Research Centre of Ispra during the seventies by Albertini *et al.* in the frame of nuclear reactor safety studies on severe accidents [124–127] and in automotive crash safety studies [128]. This innovative version can be used to perform tensile, compressive and shear tests of ductile metals and plastic specimens in a wide range of strain rates and temperatures.

The development of this modified Hopkinson bar, in which the projectile is replaced by a pretensioned bar which is a solid continuation of the input bar, was particularly needed in order to make available a unique versatile equipment able to generate repeatable long pulses (2.4 ms) with the intention of imposing large displacement until fracture on ductile specimens. By means of the traditional Hopkinson bar used as a dynamic testing equipment it would have been necessary to launch very long projectile in order to obtain pulses of comparable duration. This would have been a very difficult task, in particular with the intention of obtaining a plane impact of the projectile on the input bar, an absolutely necessary condition for the generation of an elastic stress plane wave pulse, which is needed for a correct analysis by means of the one-dimensional elastic plane stress wave propagation theory, as will be discussed in the next section.

3.4.1 Functioning of the Split Hopkinson Tensile Bar

The Split Hopkinson Tensile Bar (SHTB) consists of two bars made of high strength steel called the input and output bars. The specimen is mounted with threads between the bars. A first part of the input bar is used as a pretensioned bar (substituting the projectile of the classic Kolsky bar). The length of the pretensioned bar should be chosen in order to generate a tensile pulse allowing the specimen deformation until fracture at a constant strain rate, while the output bar length should be chosen such as to allow the specimen deformation under the clean and controlled loading resulting only from the incident tension pulse and avoiding the superposition of the wave reflections.

The SHTB functioning is based on storing a certain amount of elastic mechanical energy in the pretensioned bar length by statically pulling this bar up to a stress value lower than its yield strength. To this aim, the end section of the pretensioned bar, contiguous to the incident bar, is blocked by a brittle intermediate piece and the other end is pulled by means of a hydraulic actuator. When the necessary elastic mechanical energy is stored in the pretensioned bar, the rupture of the blocking brittle intermediate piece give rises to the contemporaneous generation of two elastic plane waves:

1. A plane elastic unloading (compression) wave starting from the bar section left free by the rupture of the brittle intermediate piece, which propagates along the prestressed bar unloading it.

2. A plane elastic tension wave starting from the same bar section, which propagates along the incident bar, loading it in tension, reaches and loads the specimen until fracture, and finally, propagates and loads in tension the output bar.

The amplitude of the loading pulse is half of the static prestress value established in the pretensioned bar by the hydraulic actuator, while the duration corresponds to the travel time of the unloading wave from the unblocked bar section to the hydraulic actuator and back. By using a long pretensioned bar it is possible to generate a tensile pulse allowing the deformation at constant high strain rate until fracture of high ductility specimens. In order to deform the specimen under the clean and controlled loading history given by the incident tension pulse without the superposition of the wave reflections from the bar ends, it is necessary to use an output bar of the same length of the prestressed bar.

The Split Hopkinson Tensile Bar (SHTB) used in this research [8, 9], whose scheme has been reported in Figure 3.8, is a tensile version of the modified Hopkinson Bar developed during the seventies by Albertini *et al.* [124, 125] consisting of two bars made of high strength steel, 9 m (input bar) and 6 m (output bar) long and 10 mm in diameter. The first 6 m of the input bar are used as a pretensioned bar. The length of the pretensioned bar has been chosen in order to generate a tensile pulse of 2.4 ms ($6\,\mathrm{m}\cdot 2/C_0 = 0.0024\,\mathrm{s}$).

Three strain-gauge stations are glued respectively:

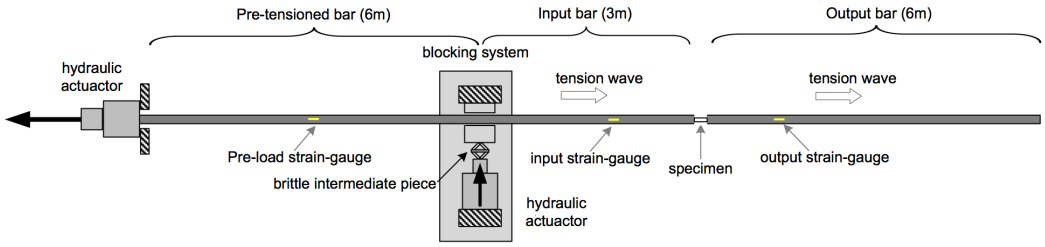

Fig. 3.8 Schematic of the SHTB used for the mechanical characterisation at room temperature, from [8].

1. On the prestressed bar, with the intention of controlling the preload.

2. On the input bar at 800 mm from the specimen, in order to record the deformation of the bar caused by the incident tensile pulse (ε_I) during its propagation toward the specimen and the deformation caused by the part of the incident tension pulse reflected (ε_R) at the interface incident bar-specimen.

3. On the output bar at the same distance from the specimen as the strain-gauge station on the input bar, in order to record the deformation caused on the bar by the part of the incident pulse which has been sustained by the specimen and has been therefore transmitted (ε_T) in the output bar.

On the basis of the signals ε_I, ε_R and ε_T, the one-dimensional elastic plane stress wave propagation theory can be applied, and the stress, the strain and the strain rate versus time within the specimen can be evaluated. Recalling, the constitutive equation (Eq.(3.1)) of the linear elasticity in a bar, the equation (Eq.(3.2)) of the propagation velocity of one-dimensional plane wave in a bar as well as the equation (Eq.(3.3)) of particle velocity in an elastic bar:

$$\sigma = E_0 \cdot \varepsilon \tag{3.1}$$

$$C_0 = \sqrt{\frac{E_0}{\rho}} \tag{3.2}$$

$$V = C_0 \cdot \varepsilon = C_0 \cdot \frac{\sigma}{E_0} \tag{3.3}$$

where σ is the stress in the bar, E_0 is the elastic modulus of the bars and ρ is the bar material density.

The forces acting at the input and output bar-specimen interfaces are given by:

$$F_{in}(t) = A_0 \cdot E_0 \cdot \Big(\varepsilon_I(t) + \varepsilon_R(t)\Big) \tag{3.4}$$

$$F_{out}(t) = A_0 \cdot E_0 \cdot \Big(\varepsilon_T(t)\Big) \tag{3.5}$$

where A_0 is the cross section of the input and output bars and t is the time.

The displacement d of the input and output bar-specimen interface are given by:

$$d_{in}(t) = \int_0^t [V_I(t) - V_R(t)]\, dt = C_0 \int_0^t \Big(\varepsilon_I(t) - \varepsilon_R(t)\Big)\, dt \tag{3.6}$$

$$d_{out}(t) = \int_0^t [V_T(t)]\, dt = C_0 \int_0^t \Big(\varepsilon_T(t)\Big)\, dt \tag{3.7}$$

Therefore the averaged values of the stress, the strain and the strain rate within the specimen are evaluated as follow:

$$\sigma_{avg}(t) = \frac{F_{in}(t) + F_{out}(t)}{2A} = \frac{A_0 E_0}{2A} \cdot \Big(\varepsilon_I(t) + \varepsilon_R(t) + \varepsilon_T(t)\Big) \tag{3.8}$$

$$\varepsilon_{avg}(t) = \frac{d_{in}(t) - d_{out}(t)}{L} = \frac{C_0}{L} \cdot \int_0^t \Big(\varepsilon_I(t) - \varepsilon_R(t) - \varepsilon_T(t)\Big)\, dt \tag{3.9}$$

$$\dot{\varepsilon}_{avg}(t) = \frac{C_0}{L} \cdot \Big(\varepsilon_I(t) - \varepsilon_R(t) - \varepsilon_T(t)\Big) \tag{3.10}$$

where A is the cross section of the specimen within the gauge length L.

In order to obtain an accurate measurement of the mechanical properties of a material subjected to a dynamic loading, two basic contitions should be fulfilled :

1. The specimen should be short enough so that the time taken by the wave to propagate through the specimen is short compared to the total time of the test, allowing many reflections inside the specimen necessary for reaching a homogeneous stress and strain distribution along the specimen gauge length and leading to an equilibrium of the forces acting on both ends of the specimen.

2. The bar diameter should be small in comparison with the pulse length, thus ensuring that the stress wave travels down the bars with negligible dispersion.

In Figure 3.9 the signals acquired during a test from the input and output strain gauges, namely incident plus reflected ($\varepsilon_I + \varepsilon_R$) and transmitted ($\varepsilon_T$) pulses are

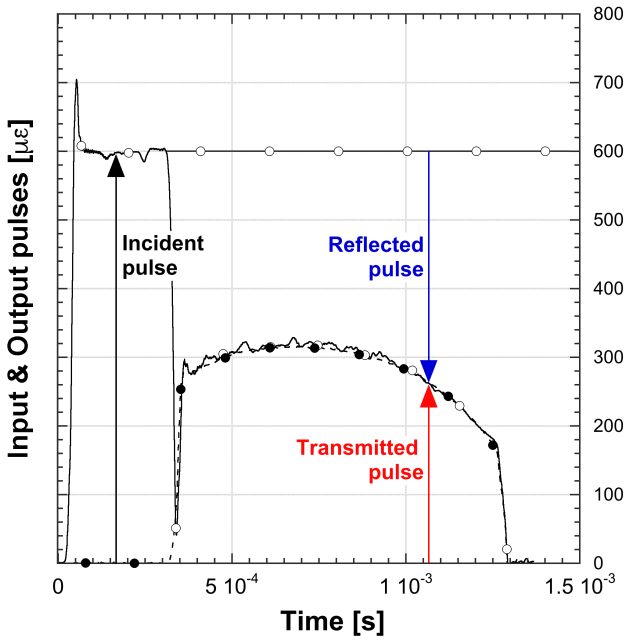

Fig. 3.9 Incident, reflected and transmitted pulses.

reported, respectively. It is possible to observe the superposition of these signals, or in other words:

$$\varepsilon_I + \varepsilon_R = \varepsilon_T \tag{3.11}$$

This is the confirmation of the achievement of force equilibrium within the sample ($F_{in} = F_{out}$) and as a consequence, the reflected pulse is obtained by subtracting the incident pulse (rectangular wave) from the input signal. Applying the previous Eq.(3.11) leads to the following simplified relations for the stress (3.12), the strain (3.13) and the strain rate (3.14) versus time within the specimen:

$$\sigma(t) = E_0 \cdot \frac{A_0}{A} \cdot \varepsilon_T(t) \tag{3.12}$$

$$\varepsilon(t) = -\frac{2C_0}{L} \int_0^t \varepsilon_R(t) \tag{3.13}$$

$$\dot{\varepsilon}(t) = -\frac{2C_0}{L} \cdot \varepsilon_R(t) \tag{3.14}$$

where E_0 is the elastic modulus of the bars, A_0 is the cross section of the input and output bars, A is the cross section of the specimen within the gauge length L, C_0

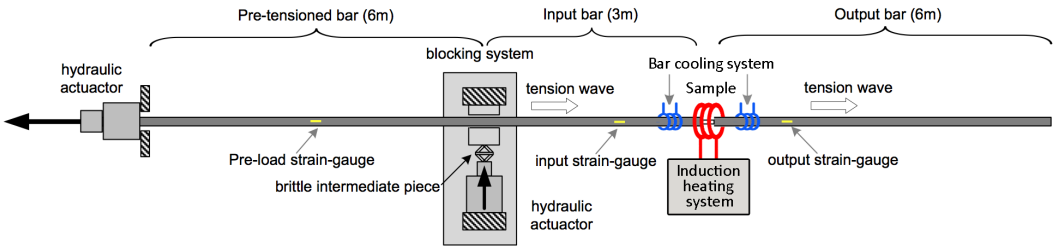

Fig. 3.10 Schematic of the SHTB used for the combined high strain rate and temperature testing, from [9].

is the bar elastic wave speed, ε_T and ε_R are the transmitted and reflected pulses, respectively.

3.4.2 Dynamic tests at high temperatures

Thanks to the versatility of the SHTB it is easily possible to perform high strain rate tests in a wide range of temperatures [9]. To do this, an Ambrell compact EASY-HEAT induction water-cooled heating systems with maximum power of 2.4 kW was integrated into the SHTB. The positioning of the thermal system is depicted in Figure 3.10.

This non-contact induction heating is ideal for heating parts of many geometries and compositions with precise power control within 25 W resolution and is able to supply energy only to the part and the zone to be heated. In Figure 3.11, the setup for the high strain rate tests at elevated temperature is shown. It is possible to observe the input ① and the output bars ② of the SHTB, the heating system ③, the water-cooled induction coil ④, the sample to be tested ⑥ connected by means of a thermocouple to a thermal controller ⑤ and, approximately at 15 cm from the specimen, the cooling system ⑦ for the input and output bars, respectively.

The tests at high temperature were performed as follow: firstly (i) the sample was mounted between the input and output bars, (ii) and then the thermocouple was welded in the middle part of the gauge length of the sample. Secondly, using the heating systems, (iii) the sample was heated at a constant heating rate (2.78 °C/s) to the desired temperature that (iv) was kept constant for 10 minutes in order to reach a homogeneous distribution along the whole specimen and in particular in the gauge length part (see Figure 3.2 and Figure 3.12). Lastly, (v) the test was performed in

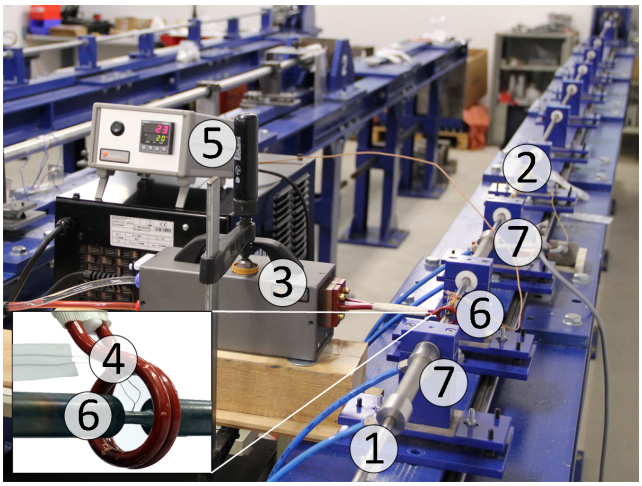

Fig. 3.11 Setup for the high strain rate tests at elevated temperatures, from [9].

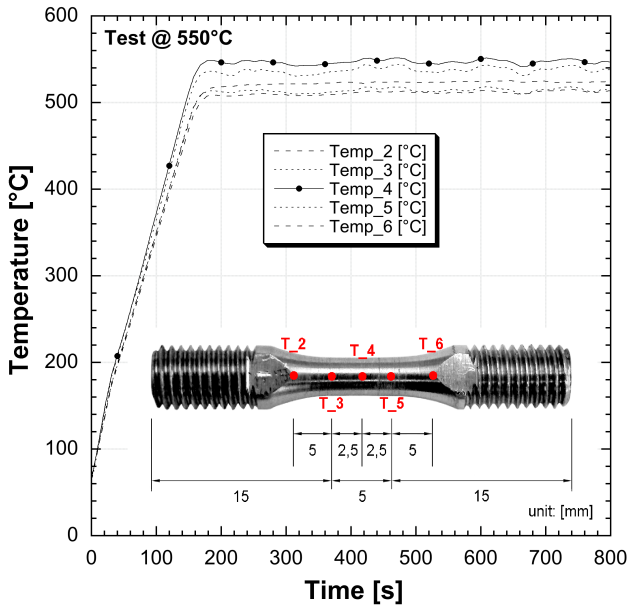

Fig. 3.12 Distribution of the temperature along the whole specimen at 550 °*C*, from [9].

steady-state conditions. It is worth noting that at high strain rates no heat is dissipated from the specimen to the surrounding and the test conditions are adiabatic. As a consequence, mainly during the necking process, the temperature of the specimen rises further. This temperature increase, limited to few dozens of degrees [129, 130], has been considered negligible for the purposes of the testing.

Then, using the previous Equations (3.12), (3.13) and (3.14), stress, strain and strain rate as function of time have been evaluated.

In order to check the temperature distribution within the sample, five thermocouples were welded in five different positions within the sample length. In Figure 3.12 the positioning of the thermocouples are reported for a temperature check at 550 °C. After approximately 200 s it is possible to observe the constancy of the temperature and the homogeneous distribution along the whole specimen, in particular in the gauge length part. This verification was performed at the five temperatures with the scope of checking the homogeneous distribution.

3.5 The Hydro-Pneumatic Machine for testing at medium strain rates

In order to study the strain rate sensitivity at room temperature and at intermediate strain rates ($5 \div 25\ s^{-1}$) a Hydro-Pneumatic Machine (HPM) was used. An image of the HPM is reported in Figure 3.13 from which it is possible to see that the machine is composed of:

1. A cylindrical tank divided in two chambers by a sealed piston. One chamber to be filled with water ①, while the other chamber to be filled with gas ② at high pressure.
2. A piston shaft which extends out of the gas chamber ③ through a sealed opening, and its end is connected to the specimen ④ to be tested.
3. A strain-gauge instrumented elastic bar ⑤, one end of which is connected to the specimen to be tested and the other end is rigidly fixed to the machine supporting structure.

In order to perform a test, a fast electro-magnetic valve ⑥ closing the water chamber is quickly opened. As a consequence, the force exerted by the gas pressure on one

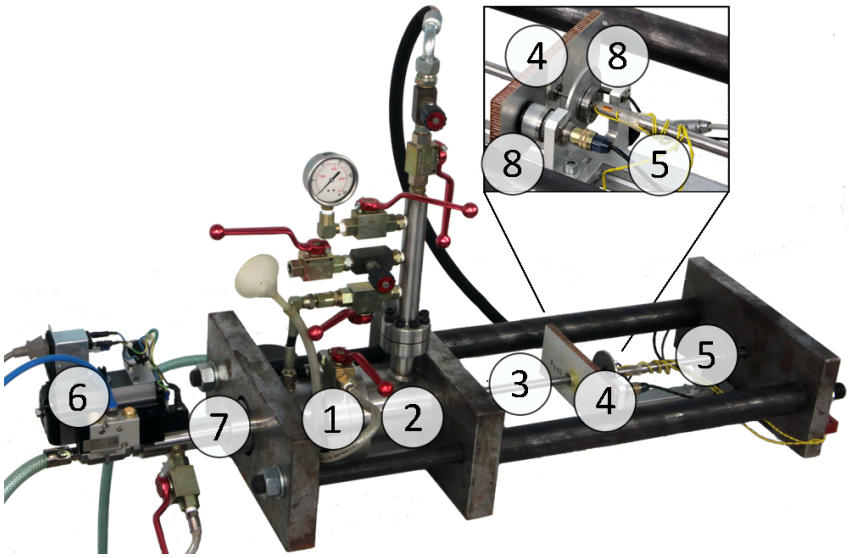

Fig. 3.13 Hydro-Pneumatic Machine used for the characterisation at intermediate strain rates.

face of the piston prevails, accelerating the piston (pushing water to flow out through a calibrated orifice ⑦ at a constant speed) and simultaneously loading the specimen, with the result of imposing a strain to the specimen with a constant strain-rate. Through the elastic properties of the bar it is possible to measure the load on the specimen, while by means of two targets attached at both ends of the specimens it is possible to obtain the specimen elongation by using two non-contact displacement transducers ⑧.

3.6 Static tests

Quasi-static tests ($10^{-3}\,s^{-1}$) were performed at room temperature by means of a universal electro-mechanical testing machine type Zwick/Roell-Z50.

This page intentionally left blank.

Chapter 4

Experimental results

In order to study the robustness of steel structures subjected to a progressive collapse triggered by a coupled effect of fire and dynamic loading, this Chapter deals with the mechanical characterisation of the S355 structural steel in a wide range of strain rates and temperatures.

Firstly, a brief description on the testing conditions is reported. Then, the strain rate influence at room temperature is studied. Lastly, the mechanical behaviour at high strain rates and in a wide range of temperatures is presented as well.

Data presented in this chapter are part of two published papers in *Engineering Structures* [8] and in *Materials and Design* [9].

4.1 Introduction

With the intention of studying the strain rate sensitivity at room temperature of the S355 structural steel, quasi-static, medium and high strain rate tests were performed at room temperature (20 °C).

Then, in order to understand the effect of the temperature on the dynamic mechanical properties, high strain rate tests at elevated temperatures were performed using the same testing conditions adopted at room temperature. At room temperature the target strain rates were set at $300\,s^{-1}$, $500\,s^{-1}$ and $850\,s^{-1}$. The corresponding particle velocity in the input bar, evaluated using the previous Eq. (3.3), as well as the target strain rate $\dot{\varepsilon}^*$, can been used as a reference for the testing condition (Figure 4.1 and Table 4.1).

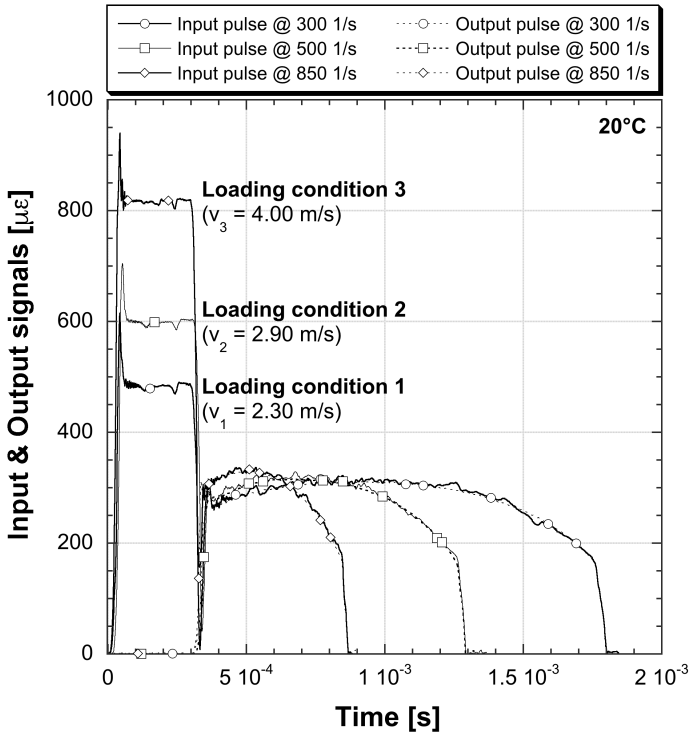

Fig. 4.1 Preloading conditions.

The strain rate obtained during the experimental tests has been evaluated as the average value after the yield and up to the ultimate tensile strength. From Figure 4.2, where the stress and the strain rate as a function of time have been evaluated using the previous Eqs. (3.8) and (3.10), it is possible to note that the strain rate remains nearly

Testing condition (-)	Particle velocity in the input bar (m/s)	Target strain rate at 20°C, $\dot{\varepsilon}^*$ (s^{-1})
1	$v_1 = 2.30$	300
2	$v_2 = 2.90$	500
3	$v_3 = 4.00$	850

Table 4.1 Testing conditions at high strain rates.

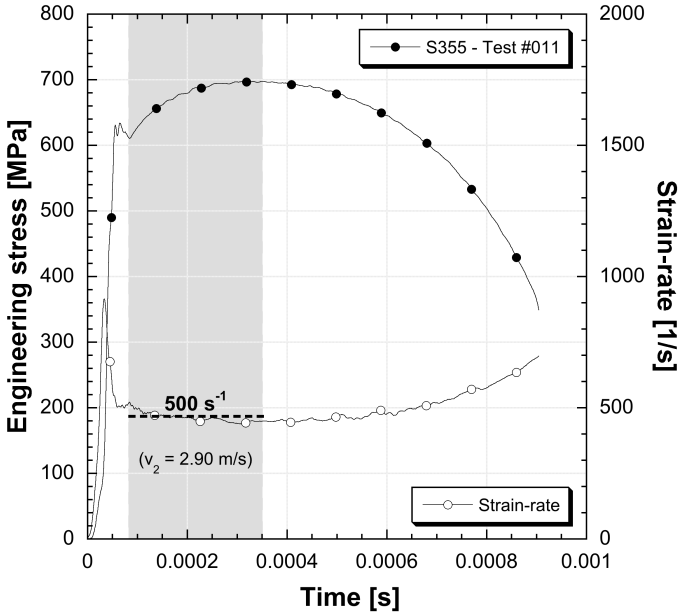

Fig. 4.2 Stress and strain rate versus time at 20 °C.

	Quasi static tests	Medium strain rate tests		High strain rate tests		
Target strain-rate at 20 °C, $\dot{\varepsilon}^*$	0.001 (s^{-1})	5 (s^{-1})	25 (s^{-1})	300 (s^{-1})	500 (s^{-1})	850 (s^{-1})
Tests at 20 °C	3	3	3	3	3	3
Tests at 200 °C	-	-	-	3	3	3
Tests at 400 °C	[103]	-	-	3	3	3
Tests at 550 °C	[103]	-	-	3	3	3
Tests at 700 °C	[103]	-	-	3	3	3
Tests at 900 °C	-	-	-	3	3	3

Table 4.2 Scheduled tensile test campaign of this research.

constant in this zone. For the sake of completeness, the scheduled experimental tensile tests are reported in Table 4.2.

4.1.1 Mechanical tensile properties

In order to make a full comparison between data at different strain rates as well as different temperatures, the following mechanical tensile properties were evaluated.

- The reduction of area at fracture (Z), evaluated as follows:

$$Z = \frac{A - A_{fract}}{A} \tag{4.1}$$

  where A is the cross section of the specimen within the gauge length, while A_{fract} is the area at fracture measured by means of a post-mortem examination of the specimens by measuring the diameter (see Figure 4.3 as an example).

- The upper yield strength ($f_{y,up}$).

- The lower yield strength ($f_{y,low}$).

- The proof strength ($f_{p,0.2\%}$), as the stress corresponding to the intersection point of the stress-strain curve and the initial slope line offset by 0.2%.

- The effective yield strength ($f_{y,x\%}$), as the stress at level of total strain of 0.5%, 1.0%, 2.0%, 5.0%, 10% and 15% corresponding to the intersection point of stress-strain curve and a vertical line at these strain levels.

- The ultimate tensile strength (f_u), as well as the corresponding uniform strain (ε_u).
- The engineering fracture strength (f_f), as well as the corresponding engineering fracture strain (ε_f).
- The true fracture strength ($f_{f,true}$), as well as the corresponding true fracture strain ($\varepsilon_{f,true}$). See Eqs 4.3 and 4.4.
- The strain energies under the true stress versus strain curve up to determined value of strains (ε^*), evaluated as follow:

$$U = \int_0^{\varepsilon^*} \sigma(\varepsilon, T) d\varepsilon \tag{4.2}$$

  where the value of ε^* has been chosen in order to evaluate:

  - the modulus of resilience ($\varepsilon^* = \varepsilon_y$),
  - the strain energy in correspondence of the true uniform strain ($\varepsilon^* = \varepsilon_{u,true}$),
  - the modulus of toughness, evaluated up to the true fracture strain ($\varepsilon^* = \varepsilon_{f,true}$).

The results have been reported in terms of engineering and true stress-strain curves[1]. In particular, the true stress-strain curves are regarded as significant up to the ultimate tensile strength. After this point the stress localisation as well as the fracture propagation governs the flow stress. Then, beyond this point the one-dimensional true stress-strain curve has been reconstructed by calculating the true stress and the true strain using the Bridgman formulae [131], which introduces the correction for the triaxial stress state. The true fracture strength ($f_{f,true}$), as well as the corresponding true fracture strain ($\varepsilon_{f,true}$) is evaluated as follows:

$$f_{f,true} = \frac{f_f}{(1 + \frac{2R}{a}) \cdot \ln(1 + \frac{a}{2R})} \tag{4.3}$$

$$\varepsilon_{f,true} = 2 \cdot \ln \frac{D}{D_{fract.}} \tag{4.4}$$

[1] $\sigma_{true} = \sigma_{eng.}(1 + \varepsilon_{eng.})$, while $\varepsilon_{true} = \ln(1 + \varepsilon_{eng.})$

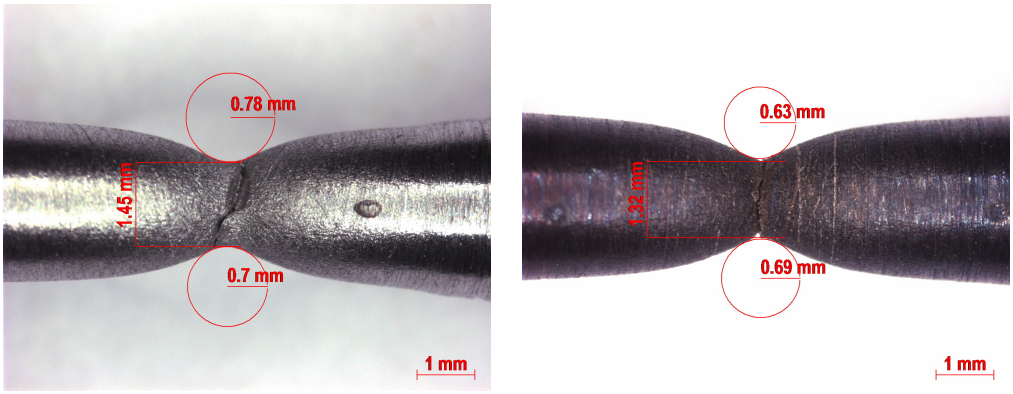

(a) 20 °C (b) 200 °C

Fig. 4.3 Post-mortem examination of two samples tested at 500 s^{-1}.

where a is the minimum radius at the reduced section of the specimen, R is the meridional profile radius of curvature at the reduced section of the specimen, D and $D_{fract.}$ are the initial diameter and the diameter of the reduced section of the specimen, respectively. These geometrical properties were obtained by means of a post-mortem examination of each specimen (see Figure 4.3 as an example) using a Zeiss stereo microscope Stemi 2000.

4.2 The strain rate influence at room temperature

The mechanical tensile property data evaluated from tests at room temperature are collected as average and standard deviation values in Table A.1. The high reproducibility of tests performed at different strain rates is confirmed by the quite low standard deviation.

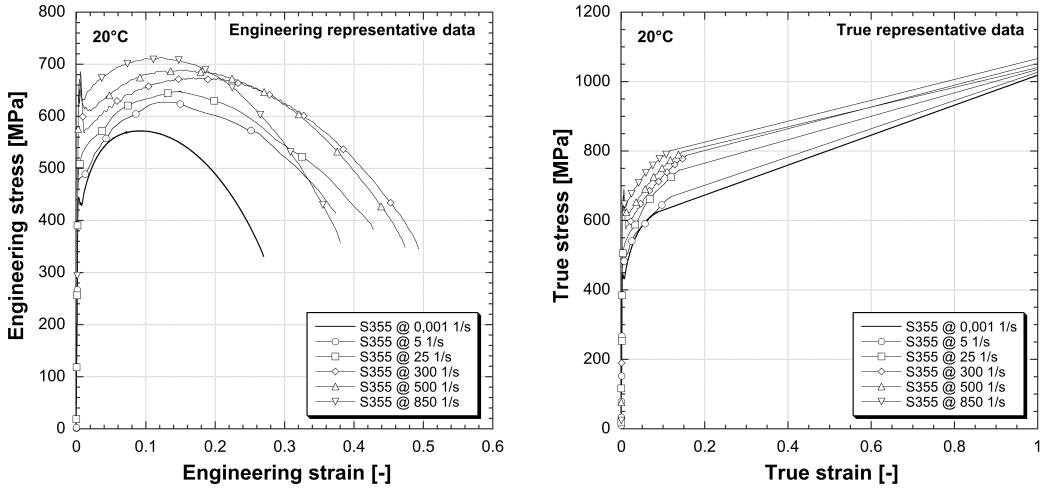

(a) Engineering (b) True

Fig. 4.4 Representative stress-strain diagrams at 20 °C.

For the sake of clarity the representative engineering and true stress-strain curves are reported in Figure 4.4. The comparison among three tests performed at the same testing condition is shown in Appendix A.1 (Figure A.1-A.6).

From Figure 4.4 it is possible to observe the strain rate sensitivity of the structural steel S355 on both the strength and the fracture strain. Moreover, the strain hardening capacity with increasing strain-rates can be observed. At high strain strain rates an instability, such as upper and lower yield strengths, is present.

After the ultimate tensile strength, the true stress-strain curves were reconstructed using the Bridgman formulae (Eqs 4.3 and 4.4). By means of the high speed camera *Y4-S3 Motion Pro* the necking process was monitored, and the relevant parameters quantified. This camera is able to record up to 7'000 fps at the maximum resolution (1024x1024), while 100'000 fps can be recorded at 1024x8. In Figure 4.5(a) the setup used to record the images is reported. In Figure 4.5(b) eight frames during the failure process of a sample tested at $850\,s^{-1}$ are reported. In this testing condition,

the time between each frames is about 7,9 μs, while the global frame rate was set at 63000 fps.

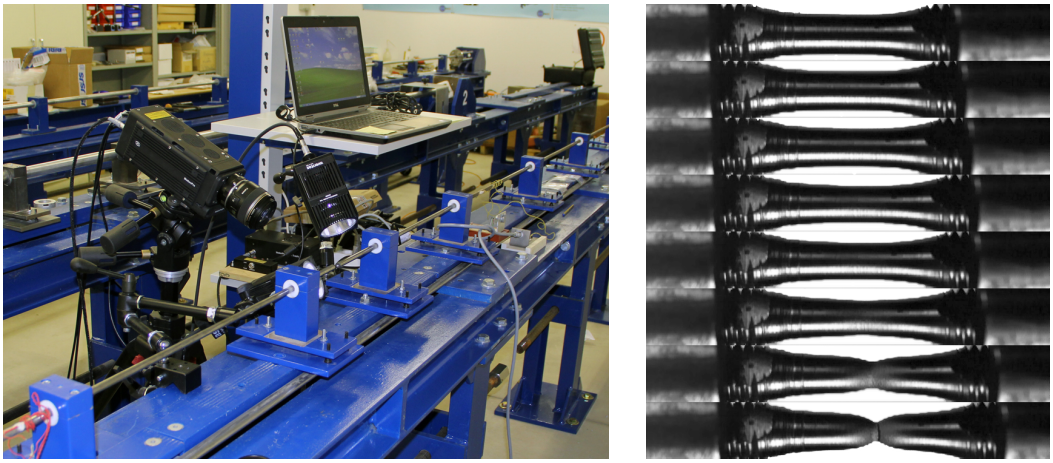

(a) (b)

Fig. 4.5 (a) Y4-S3 Motion Pro Camera and (b) eight frames during the failure process of a sample tested at 850 s^{-1} [8].

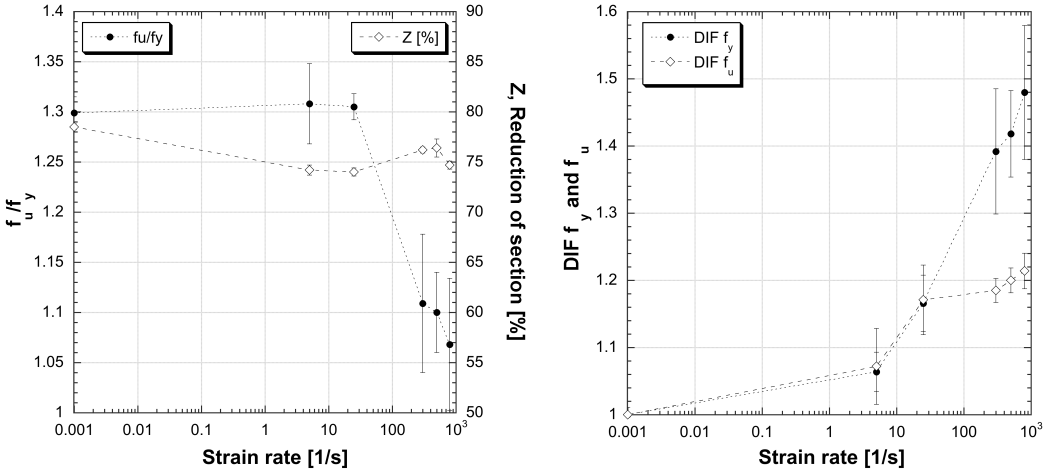

(a) (b)

Fig. 4.6 Ductility indexes: (a) $f_u/f_{p,0.2\%}$ ratio and reduction of area at failure and (b) DIFs for ultimate tensile strength and yield strength.

A widely used strain-rate index is the ductility. Different ductility indexes could be considered. Firstly, the ratio between the ultimate tensile strength (f_u) and the proof strength ($f_{p,0.2\%}$), secondly, the reduction of area at failure (Z), and lastly, the ratio between the dynamic and quasi-static values, namely dynamic increase factor

(DIF). The first two indexes are depicted in function of the strain rate in Figure 4.6(a). It is possible to observe that, the $f_u/f_{p,0.2\%}$ ratio highlights a marked decrease in ductility at high strain rates, while the reduction of area at failure (Z) does not seem to be significantly influenced by the strain rate. In Figure 4.6(b) both DIFs for ultimate tensile strength and yield strength are reported as a function of the strain rate. Up to the medium strain-rates, both DIFs have the same trend. At high strain rates the DIF for the ultimate tensile strength is perceptibly lower than the DIF for the yield strength.

In Figure 4.7 the strain energies in function of the strain rate are depicted. It is possible to observe a similar upward trend for both the modulus of resilience (U_y, Figure 4.7a) and the strain energy evaluated at the uniform strain (U_u, Figure 4.7b). On the other hand, the modulus of toughness presents higher values but does not seem to be strongly influenced by the increasing strain rates (U_f, Figure 4.7c).

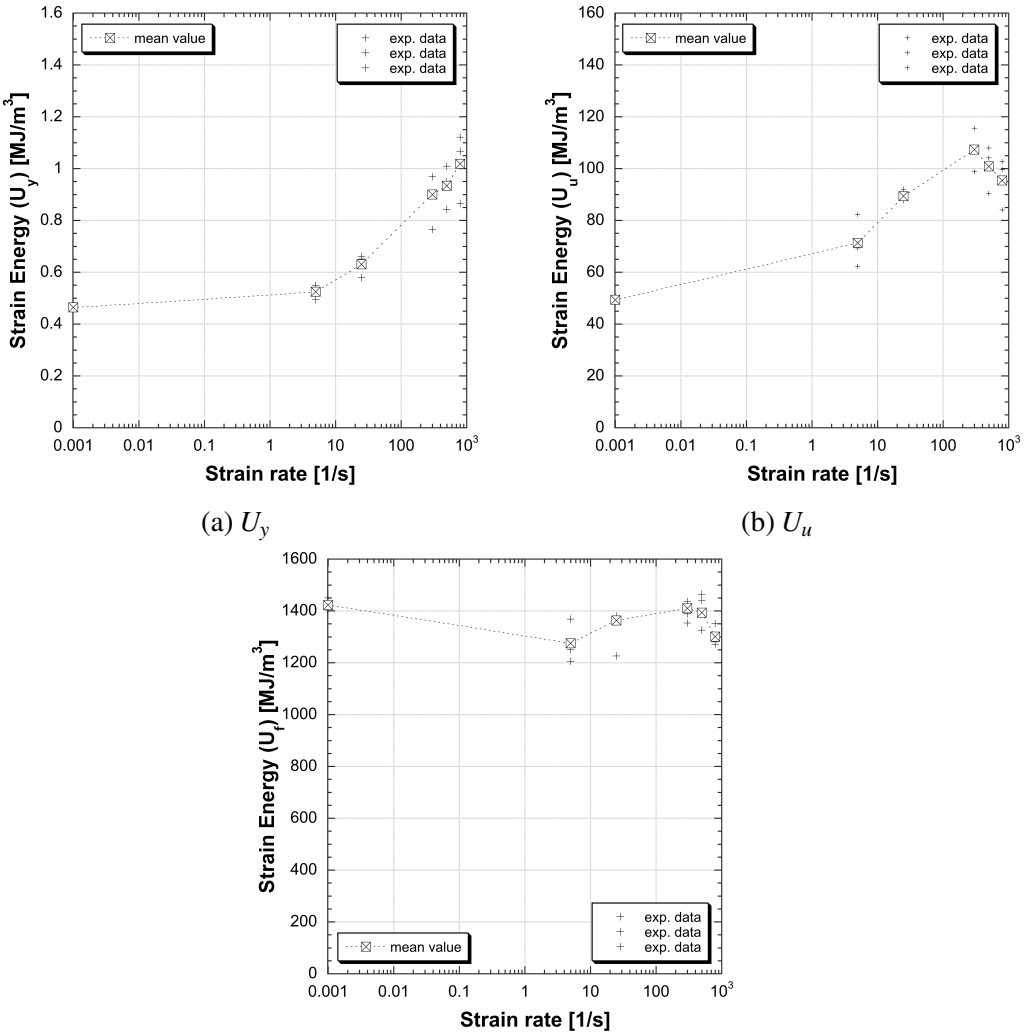

(a) U_y (b) U_u

(c) U_f

Fig. 4.7 Strain energies in function of the strain rate.

4.3 Mechanical behaviour at high strain rates in a wide range of temperature

The representative engineering and true stress-strain curves are reported in function of the testing conditions in Figures 4.8-4.10. The comparison among tests performed at the same testing condition is shown in Appendix A.2 (Figure A.7-A.21).

The mechanical tensile property data evaluated from tests at high temperatures are collected as average and standard deviation values and are reported in Appendix A.2 (Tables A.2-A.4).

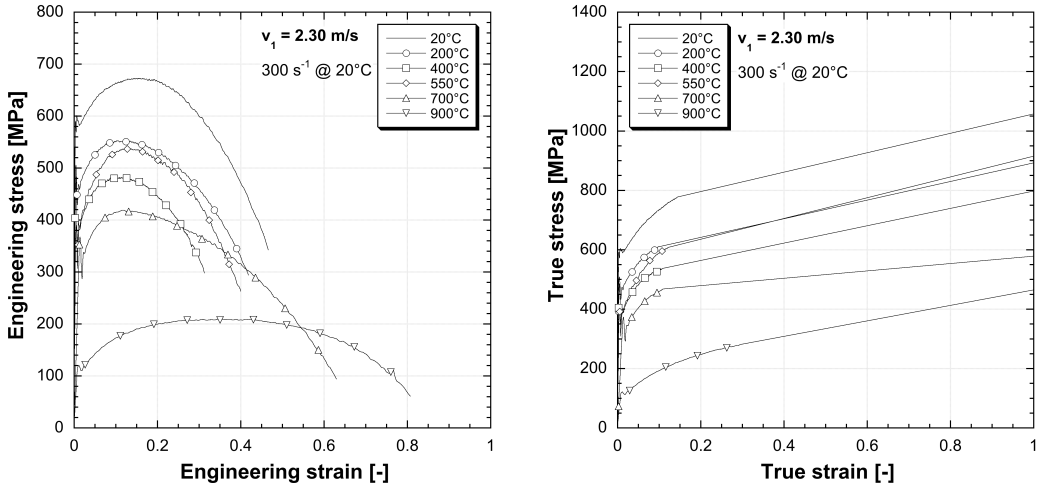

(a) Engineering (b) True

Fig. 4.8 Representative stress-strain diagrams ($\dot{\varepsilon}^* = 300\,\mathrm{s}^{-1}$ at 20°C).

The effect of the elevated temperatures is clearly visible on the strain rate. A noticeable increase in the average strain rate (Eq. 3.10 and Figure 4.2) is observed at different temperatures (Figure 4.11). This is due to the different mechanical properties of steel at elevated temperatures, which lead to an increase of the reflected pulses. This is highlighted in Figure 4.12, where different incident and reflected pulses are depicted at different temperatures.

As a consequence, the comparison between the tensile properties at different temperatures is reported as a function of the testing conditions (Table 4.1). In literature [91, 98, 90, 103], the most used way of comparing the mechanical properties at different temperatures is by means of a reduction factor determined as the ratio of

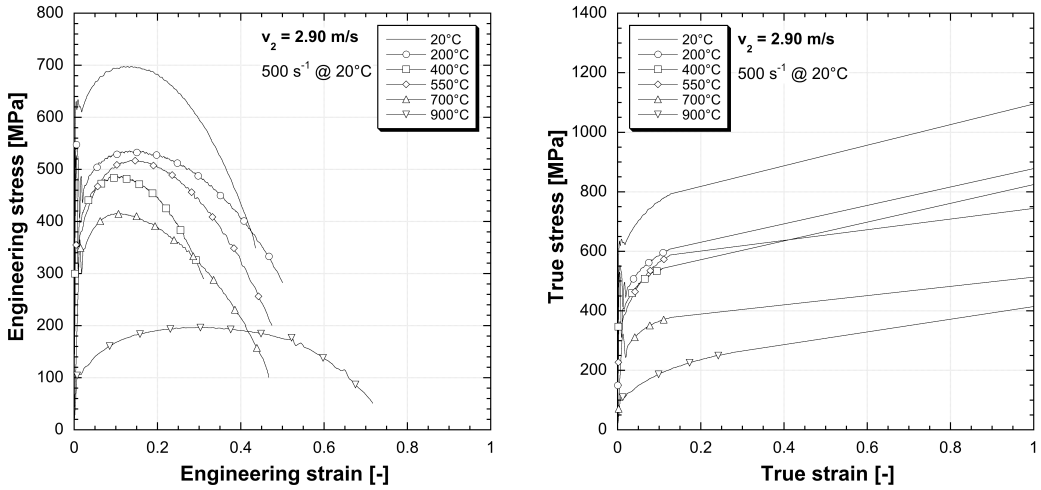

(a) Engineering (b) True

Fig. 4.9 Representative stress-strain diagrams ($\dot{\varepsilon}^* = 500\,\mathrm{s}^{-1}$ at 20°C).

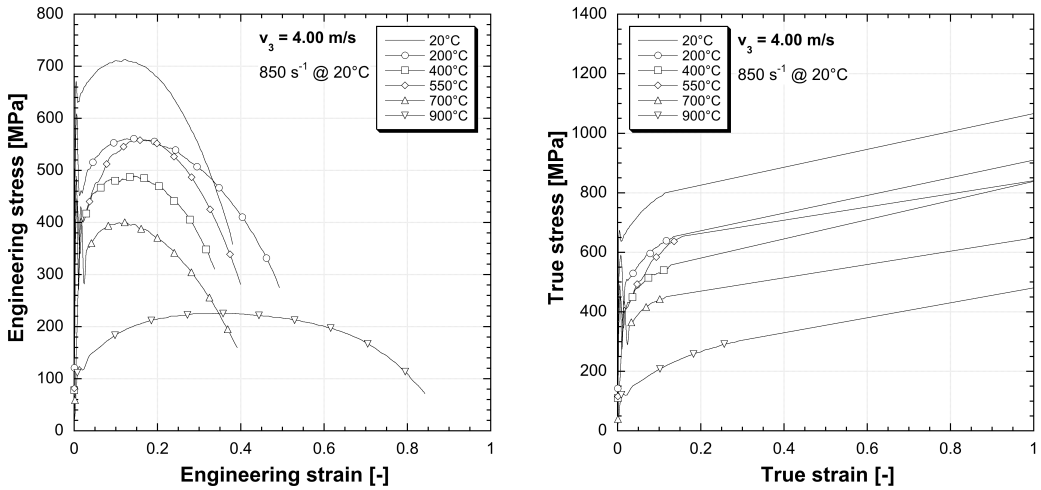

(a) Engineering (b) True

Fig. 4.10 Representative stress-strain diagrams ($\dot{\varepsilon}^* = 850\,\mathrm{s}^{-1}$ at 20°C).

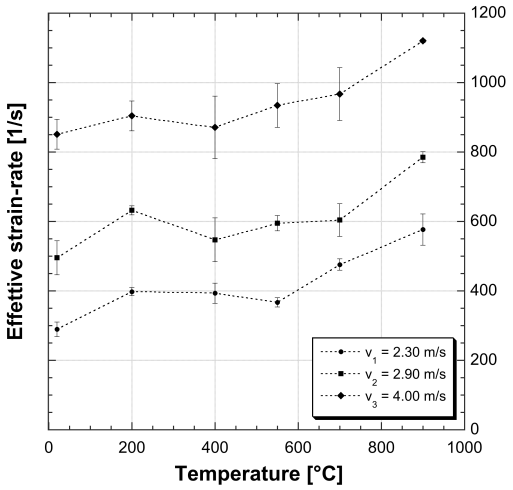

Fig. 4.11 Effective strain rate at increasing temperatures.

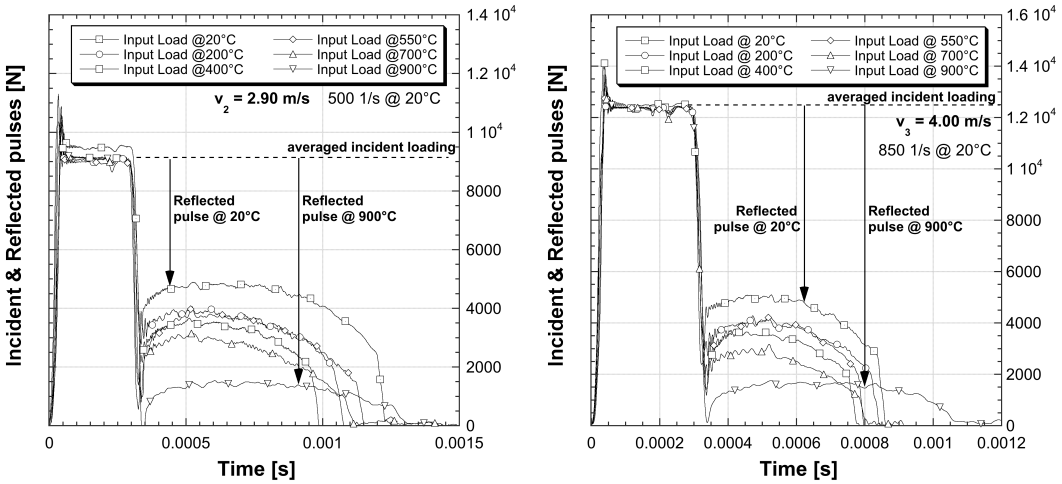

(a) ($\dot{\varepsilon}^* = 500\,\mathrm{s}^{-1}$ at 20°C). (b) ($\dot{\varepsilon}^* = 850\,\mathrm{s}^{-1}$ at 20°C)

Fig. 4.12 Comparison of reflected pulses at increasing temperatures.

the value at elevated temperatures to the corresponding value at room temperature:

$$f(T) = \frac{f_{x,\theta}}{f_{x,20}} \tag{4.5}$$

where $f_{x,20}$ and $f_{x,\theta}$ are the mechanical properties under consideration at room and high temperature, respectively.

The reduction factors for the main mechanical properties are reported in Figures 4.13-4.14. Even if the average strain rates are quite dissimilar, the reduction factors are not strongly different for the three testing conditions. As reported by Fransen and Vila Real [132], the reduction factor for the proof strength depends on the steel grade. The values for the S355 structural steel in quasi static conditions reported in [132], are in good agreement with data obtained at high strain rates only up to 400 °C (see Figure 4.13a). At higher temperatures the reduction factor overestimates those obtained at high strain rates. On the other hand, the reduction factor proposed by the Eurocode 3 [70] for the proportional limit in quasi-static conditions differs significantly from the reduction factors obtained at high strain rates. In fact, the reduction factor proposed by the Eurocode 3 [70] overestimates those obtained at high strain rates starting from 200 °C (see Figure 4.13a). Finally, it is worth noting that on the Eurocode 3 [70] the proof strength is not reported as a function of the steel grade, as also mentioned by Fransen and Vila Real [132].

An important consideration for the S355 mechanical properties is highlighted in Figures 4.8-4.10 and Figures 4.13-4.14. In fact, it is possible observe a significant decrease of strengths up to 400 °C, while in the range of 400 - 550 °C a slight increase is noted before a new marked decrease noticed up to 900 °C. This atypical behaviour is a common occurrence for carbon steels, known as blue brittleness, where in specific ranges of strain rates and temperatures an increase of strength and a reduction of ductility are ascribed to the dynamic strain ageing (DSA). This phenomenon is caused mainly by the interaction of nitrogen atoms with dislocations or, in other words based on the dislocation motion and its dependence on the interstitial atoms [133, 134]. This phenomenon has been highlighted also by Nemat-Nasser and Guo [135], Guo [136] and Albertini et al. [137]. In particular it is pointed out that the DSA shifts to higher temperatures with increasing strain rate. A strength increase at 550 °C is found in this research.

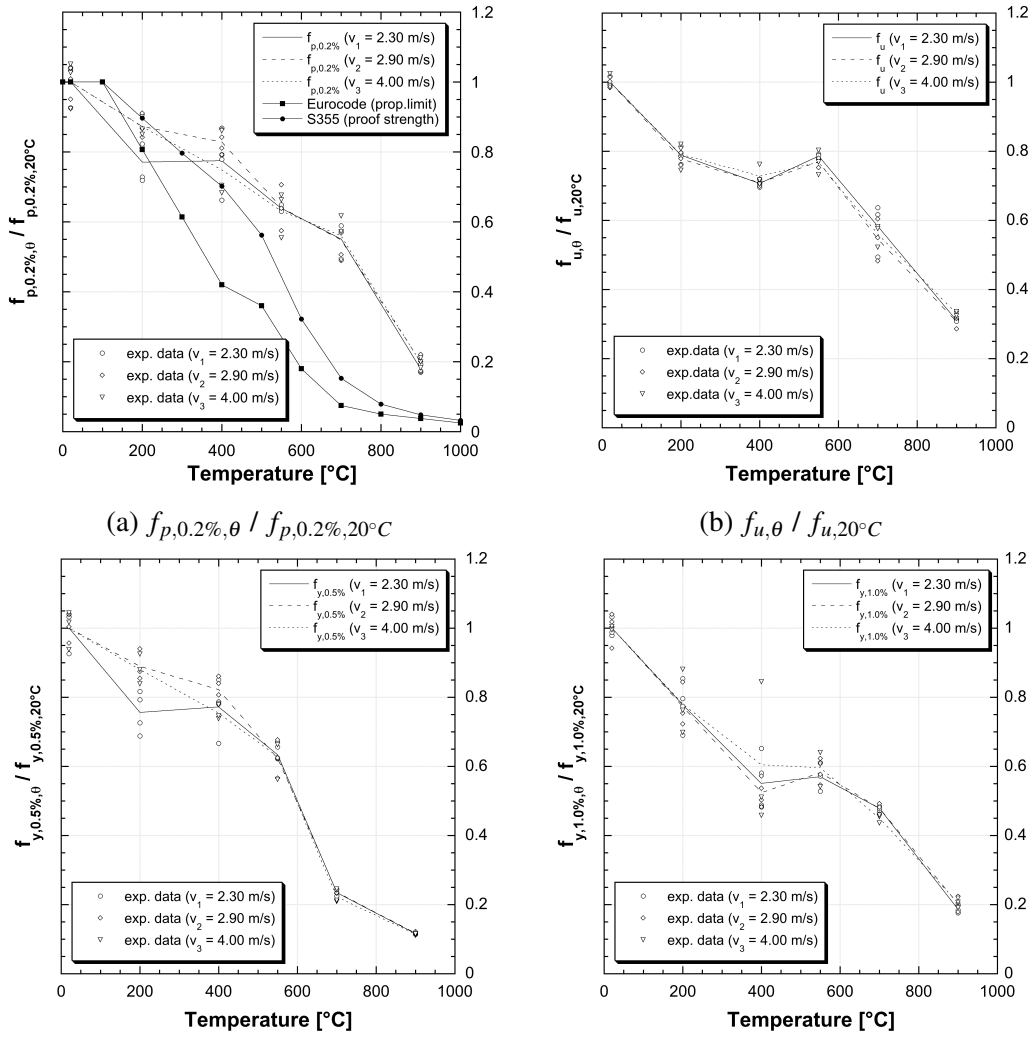

(a) $f_{p,0.2\%,\theta}$ / $f_{p,0.2\%,20°C}$

(b) $f_{u,\theta}$ / $f_{u,20°C}$

(c) $f_{y,0.5\%,\theta}$ / $f_{y,0.5\%,20°C}$

(d) $f_{y,1.0\%,\theta}$ / $f_{y,1.0\%,20°C}$

Fig. 4.13 Reduction factors for: proof strength (a), ultimate tensile strength (b), effective yield strength at 0.5% (c), 1.0% (d).

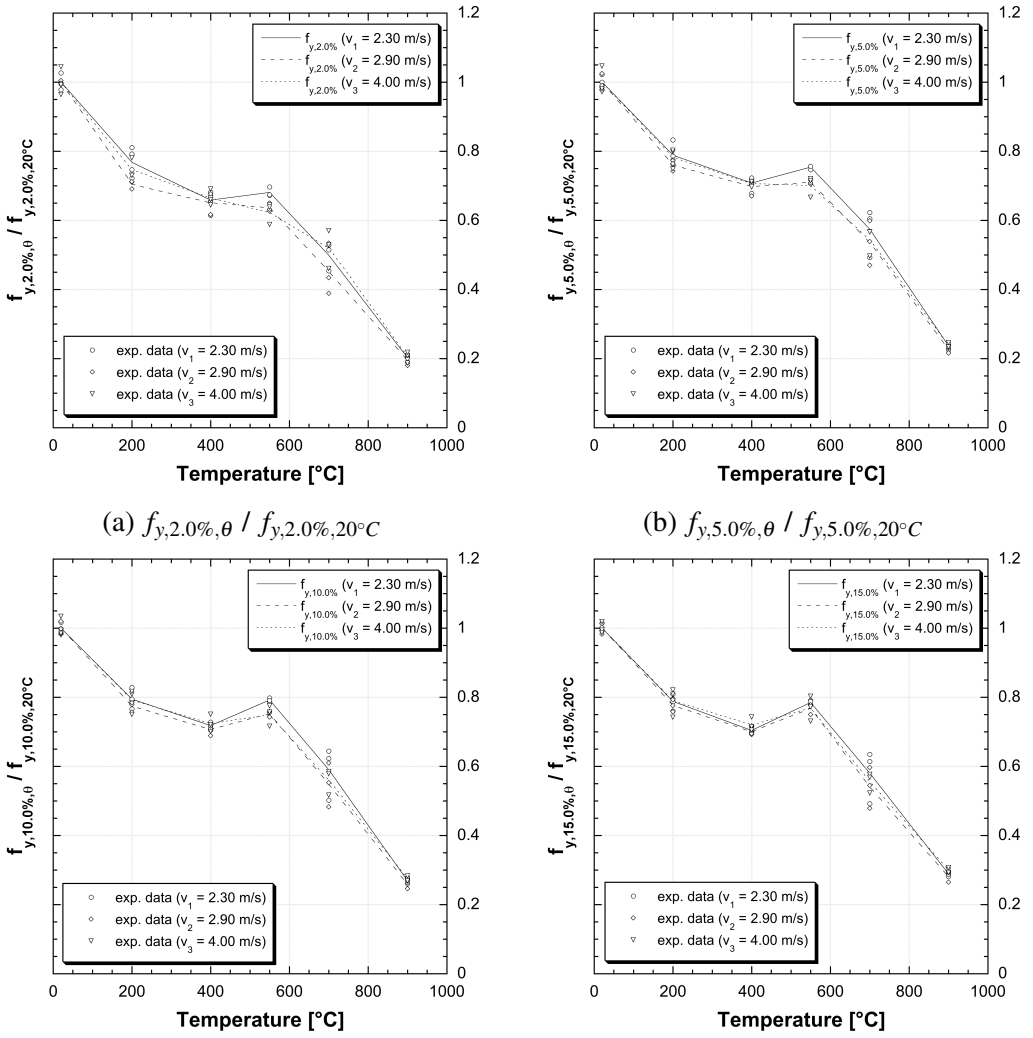

(a) $f_{y,2.0\%,\theta}$ / $f_{y,2.0\%,20°C}$ (b) $f_{y,5.0\%,\theta}$ / $f_{y,5.0\%,20°C}$

(c) $f_{y,2.0\%,\theta}$ / $f_{y,2.0\%,20°C}$ (d) $f_{y,5.0\%,\theta}$ / $f_{y,5.0\%,20°C}$

Fig. 4.14 Reduction factors for effective yield strength at 2.0% (a), 5.0% (b), 10.0% (c) and 15.0% (d).

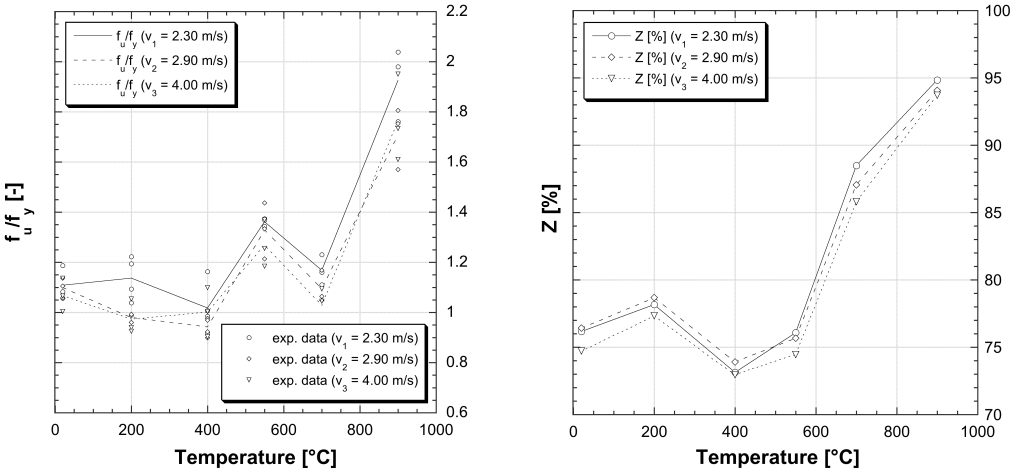

(a) $f_u/f_{p,0.2\%}$ ratio. (b) Reduction of area at failure.

Fig. 4.15 Trend of ductility indexes at high temperatures.

The ductility is an important aspect that should be considered also at high temperatures. In particular the ratio between the ultimate tensile strength (f_u) and the proof strength ($f_{p,0.2\%}$) is depicted in Figure 4.15(a). A marked increase of this ratio is visible at a very high temperature (900 °C). On the other hand at 550 °C the effect of the DSA is visible, but an increase of ductility is observed. This is probably due to the fact that the proof strength ($f_{p,0.2\%}$) at 550 °C do not seem to be influenced by the DSA (see Figure 4.13(a)). As a consequence the $f_u/f_{p,0.2\%}$ ratio grows at 550 °C (Figure 4.15(a)). On the other hand, the reduction of area at failure highlights an almost constant ductility up to 550 °C, with lower values obtained in the range between 400 °C and 550 °C. Then, a marked increase is noted at 700 °C and 900 °C (Figure 4.15(b)). Finally, it is worth noting that DIFs have not been evaluated as ductility indexes at high temperatures because of the lack of quasi-static data on the same sample size.

The strain energy up to the ultimate tensile strength is reported in Figure 4.16a as a function of the testing conditions. A marked decrease in the strain energy up to 400 °C is visible. On the other hand, an almost constant behaviour with approximately 50% of the strain energy capacity evaluated at room temperature is noted at the higher temperatures. The modulus of toughness is reported in Figure 4.16b. It is possible to observe a significant decrease up to 550 °C, while a marked increase is noted up to 900 °C.

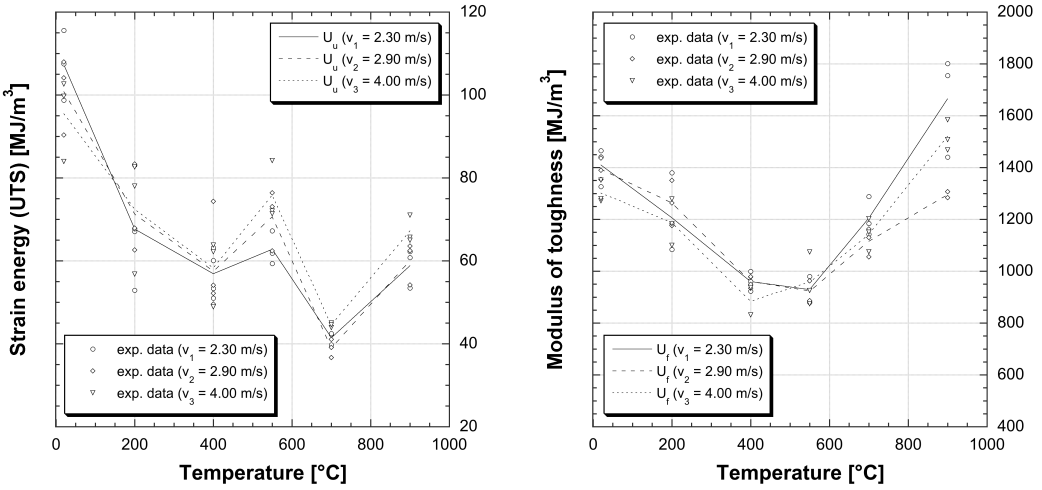

(a) U_u (b) U_f

Fig. 4.16 Strain energies for different temperatures.

Chapter 5

Constitutive model

In this chapter a brief introduction on the available temperature and strain-rate dependent models is initially presented. Then, the parameters of the selected material model are evaluated on the basis of the experimental data focusing the attention on the thermal effect at high strain rates. Lastly, a modification of the dimensionless temperature is proposed.

Some data presented in this chapter are part of two published papers in *Engineering Structures* [8] and in *Materials and Design* [9].

5.1 Introduction

The structural performance evaluation in response of a coupled effect of fire and blast loading may be performed by a variety of approaches ranging from elastic static to inelastic dynamic. The choice of the approach to perform a numerical simulation strongly influences the analysis, and as a consequence a critical evaluation of the results is fundamental. This because the greater the simplification of the analysis in representing the response of the structure, the more difficult it will be to evaluate the real performance of the structure from the calculated results. For that reason the real mechanical properties of the materials subjected to a combined effect of dynamic and fire loadings should be used to improve the numerical simulations.

In general, three different categories of temperature and strain-rate dependent models can be identified [138], as:

1. physical models,
2. semi-empirical models and
3. empirical constitutive models.

The physical constitutive models are generally based on ideas from dislocation dynamics. The Zerilli-Armstrong [139] is a simple and widely used physics-based model. More complex physical constitutive models are for example the Mechanical Threshold Stress (MTS) model [140] and the Preston-Tonks-Wallace (PTW) model [141]. On the other hand, the Steinberg-Cochran-Guinan-Lund (SCGL) [142, 143] is a semi-empirical model extensively used by the shock physics community. The empirical models are the simplest and for that reason widely used in numerical simulations. Thanks to its simplicity, one of the easy-to-use empirical constitutive relationship has been proposed by Johnson and Cook in the eighties [144]. This constitutive relationship is a phenomenological model, and even if it is not based on traditional plasticity theory, is widely used to describe the material strength [145] in numerical simulations of dynamic events. Elsanadedy et al. [146] performed a non-linear dynamic analysis in order to establish the vulnerability of a typical multi-storey steel framed building employing a simplified Johnson-Cook material model. Ding et al. [72], by using the Johnson-Cook strength constitutive equation, introduced a numerical approach to evaluate the damage of unprotected steel columns

subjected to blast load and a following fire action. Moreover, Gambirasio and Rizzi [147] presented various procedures adoptable for calibrating the parameters of the Johnson-Cook model, with the intention of provididing a useful guideline in the process of determining the best parameters in each specific situation. Other authors [148] compared different constitutive models for studying the flow behaviour of the Ti-6Al-4V alloy at low strain rates and elevated temperatures.

In the end, it is worth mentioning that among the empirical models, also rate dependent plasticity models can be adopted. In this case the dynamic effects of strain rates are taken into consideration by scaling the static yield stress. Such a model is the widely used constitutive equation proposed by Cowper and Symonds in the fifties [149]. Even if it is a very simple and used approach, it suffers from the lack of a complete flow-stress definition. Moreover, other criticisms can emerge to couple the strain rate effects with the thermal softening effects.

5.2 Johnson-Cook constitutive model

In this research the Johnson-Cook model is considered. This choice depends mainly on the availability of the experimental flow stress data in a wide range of strain rates and temperatures necessary for a satisfactory calibration of this constitutive model.

The Johnson-Cook flow stress model is based on three phenomena, which are isotropic hardening, strain-rate hardening as well as thermal softening. The flow stress can be expressed as:

$$\sigma_{JC} = (A + B \cdot \varepsilon_p^n) \cdot (1 + c \cdot ln\frac{\dot{\varepsilon}}{\dot{\varepsilon}_0}) \cdot (1 - T^{*m}) \tag{5.1}$$

where ε_p is the true plastic strain, $\dot{\varepsilon}$ is the considered strain rate, $\dot{\varepsilon}_0$ is the reference strain rate (taken as 1 s^{-1}) and T^* is the homologous temperature defined as:

$$T^* = \begin{cases} 0 & T \leq T_r \\ \dfrac{T - T_r}{T_m - T_r} & T_r < T \leq T_m \\ 1 & T > T_m \end{cases} \tag{5.2}$$

where T is the current temperature, T_m is the melting temperature and T_r is the reference temperature. Data obtained at high strain rates and at different temperatures have been used to calibrate this constitutive model. The parameters to find by means of the experimental data are A, B and n, representing the strain hardening effects of the material in quasi-static conditions, c and m representing the strain rate hardening and the thermal softening sensitivity, respectively.

5.2.1 Isotropic hardening

The isotropic hardening parameters have been evaluated by means of the three quasi-static tensile tests performed at room temperature (Figure A.1). A Matlab routine has been implemented in order to find the three parameters. In particular, A is the true yield stress determined at room temperature. Then, the experimental quasi-static data have been plotted as true plastic stress versus true plastic strain, as reported in Figure 5.1. By means of the nonlinear least squares function in Matlab using the *Curve Fitting Toolbox*™ these curves have been fitted to:

$$\sigma_{JC} = (A + B \cdot \varepsilon_p^n) \tag{5.3}$$

The parameters have been evaluated for each quasi-static test (Table 5.1). The averaged values have been used to fit the data, as reported in Figure 5.1, from which it is possible to observe the goodness of the fit.

	A [MPa]	B [MPa]	n [-]
QS test 001	450	756	0.555
QS test 002	453	856	0.609
QS test 003	441	724	0.523
avg. values	448 ± 6	782 ± 67	0.562 ± 0.044

Table 5.1 Isotropic hardening parameters.

In the previous Eq. 5.3 the strain-rate hardening and the thermal softening have not been considered, because $c = 0$ in quasi-static conditions and and $T^* = 0$ for tests at room temperature.

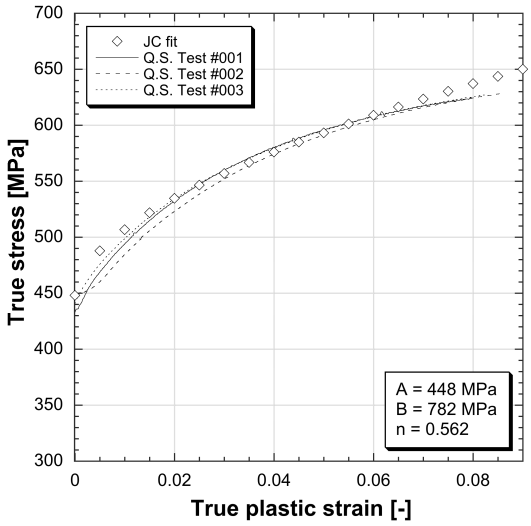

Fig. 5.1 Isotropic hardening fitting model.

5.2.2 Strain rate hardening

The strain rate sensitivity parameter has been determined for each test at room temperature by means of a Matlab routine. The starting point is the following equation:

$$\sigma_{JC} = (A + B \cdot \varepsilon_p^n) \cdot (1 + c \cdot ln\frac{\dot{\varepsilon}}{\dot{\varepsilon}_0}) \tag{5.4}$$

where A, B and n were already determined. For each test at medium and high strain rates, the experimental data have been plotted as true plastic stress versus true plastic strain. Then, by means of the nonlinear least squares function in Matlab using the *Curve Fitting Toolbox*™ these data have been fitted in order to find the only unknown of Eq. 5.4, c.

As a consequence, for each strain rate, three pairs of $c \cdot ln(\dot{\varepsilon}/\dot{\varepsilon}_0)$ could be evaluated and plotted as a function of the strain rate, as reported in Figure 5.2[1]. The final value of $c = 0.0247$ has been obtained finding the best fit of these data.

From Figure 5.3 it is possible to observe the goodness of the model to fit the selected data. On the other hand, a single value of the strain rate sensitivity parameter (c) can not be representative in case of high scatter data. In fact, a limited variation of this dimensionless parameter could strongly influence the constitutive model.

[1] In Figure 5.2 is plotted $c \cdot ln(\dot{\varepsilon})$ because $\dot{\varepsilon}_0 = 1\,s^{-1}$.

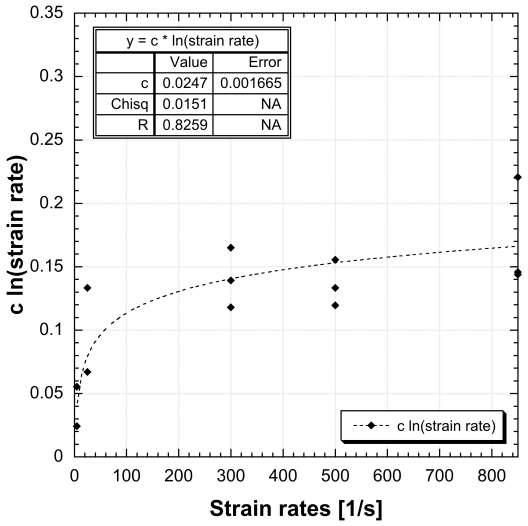

Fig. 5.2 Fitting data for the strain rate sensitivity parameter, from [8].

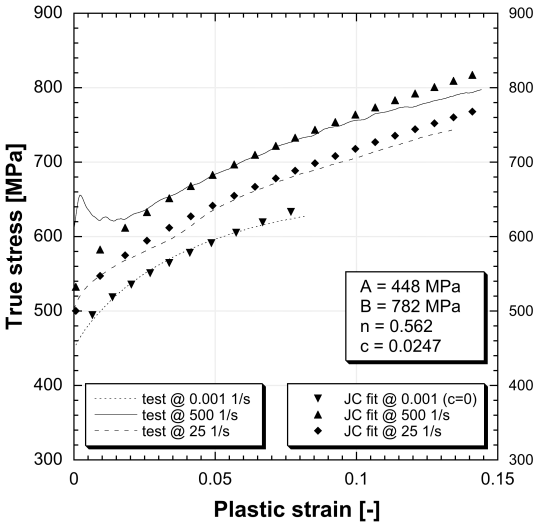

Fig. 5.3 Example of the Johnson-Cook fit at three different strain rates, from [8].

It is worth observing that the high strain rate experiments show an instability before the plastic region, usually described with upper and lower yield strengths (see Figures 4.4, 4.8-4.10 and Tables A.1-A.4). The simulation techniques usually do not allow for a decrease of stress, with the exception of the softening portion. For that reason the adopted monotonic fit could be considered as conservative, in particular for small strains. The instability can be described by using a more complex physical-based constitutive model, whose example can be found in [150].

5.2.3 Thermal softening

The thermal softening in the Johnson-Cook constitutive relationship is governed by the term $(1-T^{*m})$ in which the only unknown is a single value of m. This parameter is commonly evaluated comparing two quasi-static tests [151], one of which is performed at room temperature, and the other is performed at elevated temperature. In this case ($c = 0$) it is possible to evaluate a ratio (R_{STA}) between the true stresses at specific plastic strain. Then the thermal softening parameter is evaluated as follows:

$$m = \frac{log(1-R_{STA})}{log(T^*)} \tag{5.5}$$

The novelty in this research is the addition of the strain rate dependency to the m parameter, so $c \neq 0$. In this case an important consideration should be given: tests at different temperature but with comparable effective strain rate are required. Due to the fact that the effect of the temperature on the effective strain rate has been highlighted (Figure 4.11), additional tests were performed compensating the preload. As a consequence, two comparable set of data in terms of effective strain rates and at different temperatures, were obtained at 450 s^{-1} and 550 s^{-1}.

The thermal softening parameter could be evaluated, for a fixed strain rate by solving the following equation:

$$R^* = R \cdot (1 + c \cdot ln\frac{\dot{\varepsilon}}{\dot{\varepsilon}_0})^{-1} = (1-T^{*m}) \tag{5.6}$$

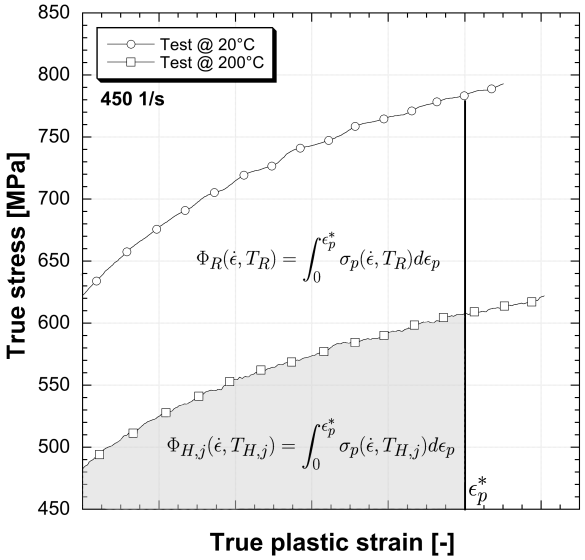

Fig. 5.4 Integration interval in Eqs. 5.8-5.9.

where c is the strain rate softening parameter equal to 0.0247, while R could be defined as the thermal softening reduction factor, evaluated as the ratio:

$$R(\dot{\varepsilon},T)=\frac{\Phi_{H,j}(\dot{\varepsilon},T_{H,j})}{\Phi_R(\dot{\varepsilon},T_R)} \qquad T_{H,j}>T_R=T_{room} \tag{5.7}$$

For each strain rate (450 and 550 s^{-1}), five pairs of $\Phi_R(\dot{\varepsilon},T_R)$ and $\Phi_{H,j}(\dot{\varepsilon},T_{H,j})$ could be evaluated for fixed room temperature (T_R) and five elevated temperatures ($T_{H,j}$, $j=1,...,5$), respectively.

These terms are defined as the area under the true stress versus true plastic strain curve and are evaluated as follows:

$$\Phi_R(\dot{\varepsilon},T_R)=\int_0^{\varepsilon_p^*}\sigma_p(\dot{\varepsilon},T_R)d\varepsilon_p \tag{5.8}$$

$$\Phi_{H,j}(\dot{\varepsilon},T_{H,j})=\int_0^{\varepsilon_p^*}\sigma_p(\dot{\varepsilon},T_{H,j})d\varepsilon_p \tag{5.9}$$

where the upper integration limit, ε_p^*, was set in order to have the same integration interval in Eq. 5.8 and Eq. 5.9. For the sake of clarity Figure 5.4 is reported. In order to compare data in the same plastic strain range, the maximum common value of ε_p^* among tests at the same temperature has been selected. These values are reported in Table 5.2.

Temperature [°C]	ε_p^* [-]	m (450 s^{-1}) [-]	m (550 s^{-1}) [-]
200	0.081	0.551 ± 0.013	0.608 ± 0.035
400	0.087	0.675 ± 0.016	0.684 ± 0.023
550	0.109	0.988 ± 0.025	0.965 ± 0.040
700	0.074	0.953 ± 0.030	0.885 ± 0.060
900	0.109	0.454 ± 0.032	0.451 ± 0.009

Table 5.2 Johnson-Cook thermal softening sensitivity parameters at different temperatures and strain rates.

The values of $\Phi_R(\dot{\varepsilon}, T_R)$ were evaluated by means of the results at different strain rates obtained at room temperature. On the other hand, the values of $\Phi_{H,j}(\dot{\varepsilon}, T_{H,j})$ were evaluated with the results at elevated temperatures.

Lastly, applying the logarithm, the thermal softening parameter can be evaluated from Eq. 5.6 as:

$$m(\dot{\varepsilon}, T) = \frac{\log(1 - R^*)}{\log(T^*)} \tag{5.10}$$

Solving the previous Eq. 5.10, it is possible to evaluate the thermal softening parameter as a function of temperature and strain rate. In Table 5.2 the obtained values are reported. It is possible to observe a noticeable variation at different temperatures. On the other hand, the thermal softening parameter trend do not seem to be significantly different for both the considered strain rates. The variation of m is shown in Figure 5.5.

An important consideration regarding the choice of the upper integration limit of Eqs 5.8 and 5.9 should be given. Although ε_p^* at different temperatures is quite small, the Johnson-Cook constitutive law is able to fit the experimental data up to higher values of ε_p^*. This is confirmed in Figure 5.6, where the Johnson-Cook constitutive law is compared to some experimental data at different temperatures and strain rates. This comparison is performed by choosing the thermal softening sensitivity parameter corresponding to the temperature test and closer to the strain rate. In Figures 5.6a and 5.6b it is possible to observe the goodness of the fit at 200 °C. At higher temperatures the fit is not as good as at 200 °C, but it is conservative.

However, this way of choosing m as a function of the temperature is only valid in simulations where the temperature is kept constant. This because in a finite element code (e.g. LS-DYNA) only a single averaged value of m is required. But, the choice

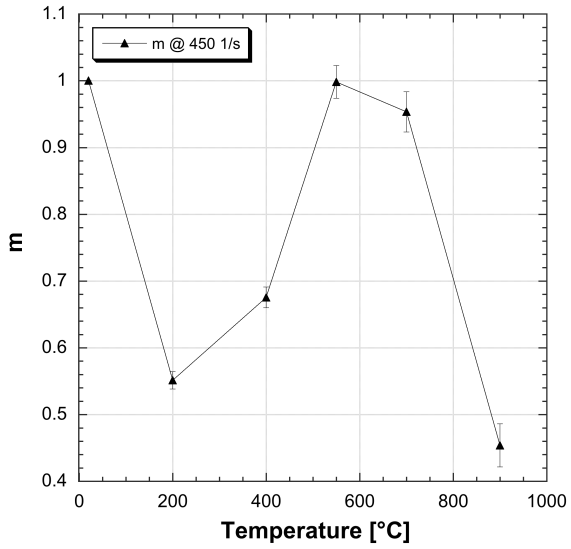

(a) Variation of m at 450 s^{-1}

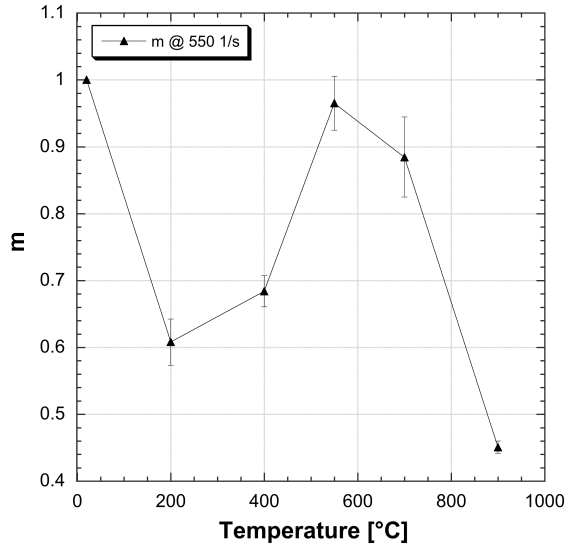

(b) Variation of m at 550 s^{-1}

Fig. 5.5 Thermal softening parameter evaluated at two different high strain rates.

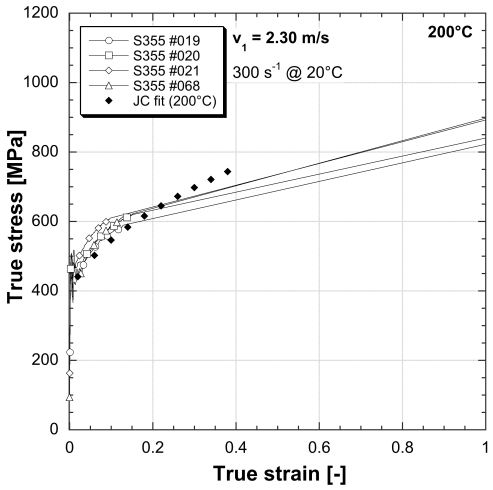

(a) Tests at 200 °C ($v_1 = 2.30 m/s$).

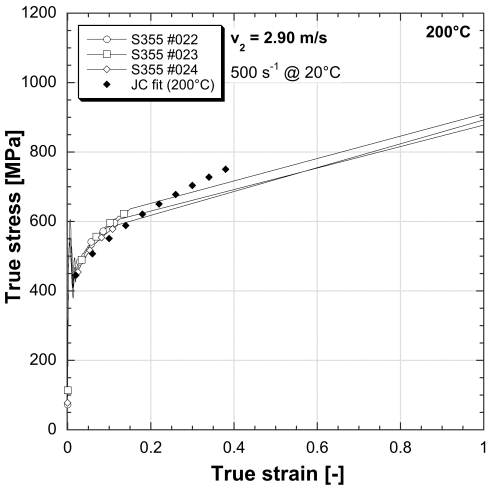

(b) Tests at 200 °C ($v_1 = 2.90 m/s$).

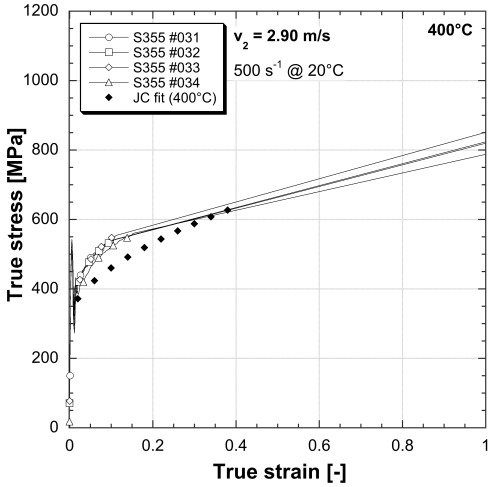

(c) Tests at 400 °C ($v_1 = 2.90 m/s$).

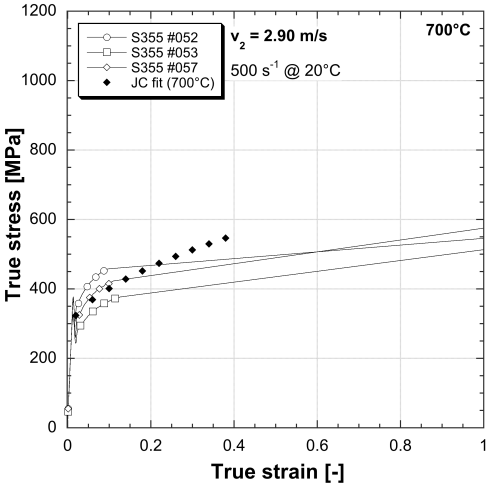

(d) Tests at 700 °C ($v_1 = 2.90 m/s$).

Fig. 5.6 Johnson-Cook fit at different temperatures and testing conditions.

of a single averaged value of m could lead to considerable errors. This is confirmed by comparing the experimental values of R^* and $(1 - T^{*m})$. From Figure 5.7 it is possible to observe how the experimental values (R^* @ 550 or R^* @ 450) can be overestimated (Figure 5.7b) or underestimated (Figure 5.7a) by the thermal effect term of Eq. 5.1 by choosing single averaged values of m.

These results are the confirmation that, if the coupled effect of high temperature and dynamic loadings would be evaluated, the effect of the extreme variation of the thermal softening would not be neglected. But, even with these limitations, the proposed variation of the thermal softening parameter (Figure 5.5) can be interpreted as an aid to obtain a more robust analysis of the coupled effect of dynamic and fire loadings. For example this could be performed by considering a step-by-step numerical simulation in which the thermal softening sensitivity term is modified in function of the temperature.

The modification of the thermal softening term could be another approach to follow. But this will be explained in the next section.

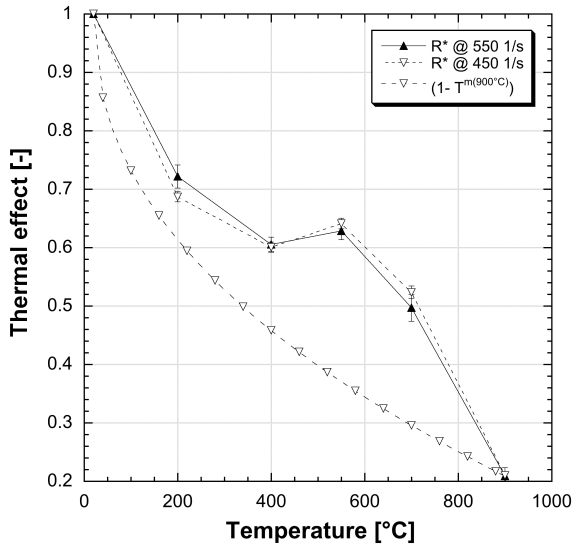

(a) $m \approx 0.45$

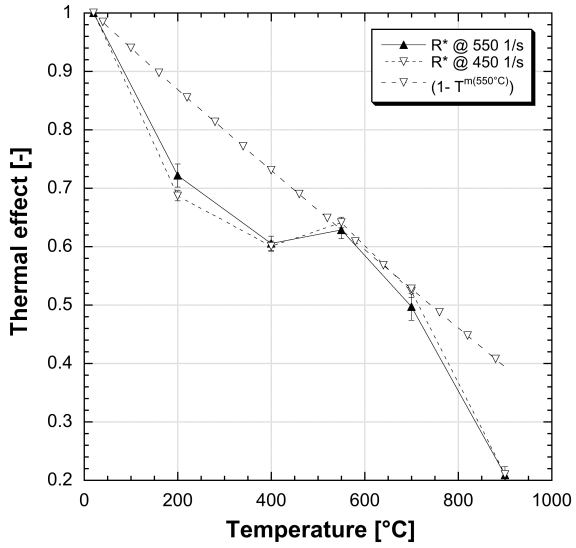

(b) $m \approx 0.98$

Fig. 5.7 Comparison of the thermal softening factors obtained experimentally, with a fixed single values of m and by applying the proposed modification of the Johnson-Cook constitutive law.

5.2.4 Modification of the thermal softening term

In the original Johnson-Cook constitutive model, the thermal softening term is simply a decreasing exponential function for increasing temperatures. This term is mainly influenced by the dimensionless temperature (Eq. 5.2).

Because of the similarity between the thermal softening parameters (Table 5.2 and Figure 5.5), the experimental thermal softening factors (R^*) present a similar trend as well (Figure 5.7). These results, obtained by using two comparable set of data in terms of effective strain rates ($450 \div 550$) s^{-1}, can be interpreted as the real behaviour of the term $(1 - T^{*m})$ at these high strain rates and at different temperatures.

For that reason, following a fitting approach of these two set of experimental data, a more suitable expression for the thermal softening sensitivity term can be proposed as follow:

$$(1 - {T_D}^f) \tag{5.11}$$

where f is a coefficient to be determined and T_D is a dimensionless temperature step-by-step defined for different temperature ranges:

$$T_D = T_{D,i} + \alpha_i \cdot \frac{T - T_i}{T_m - T_R} \tag{5.12}$$

where T_m is the melting temperature, T_R is the room temperature and the other parameters are reported in Table 5.3. In the temperature range ($20 \div 199$) °C, the original and the modified dimensionless temperature are identical ($T_D = T^*$). As a consequence, the value of f could be adopted equal to 0.58, corresponding to the averaged value of m in correspondence of 200 °C. For the sake of completeness, a comparison between the original dimensionless temperature (Eq. 5.2) and the modified version (Eq. 5.12) is shown in Figure 5.8.

Finally, by applying Eq. 5.11 it is possible to observe how the experimental data at different temperatures are well fitted. This modification, due to its step-by-step definition for increasing temperatures (Fig. 5.9), is also able to take into consideration the increase of the tensile strength at 550 °C.

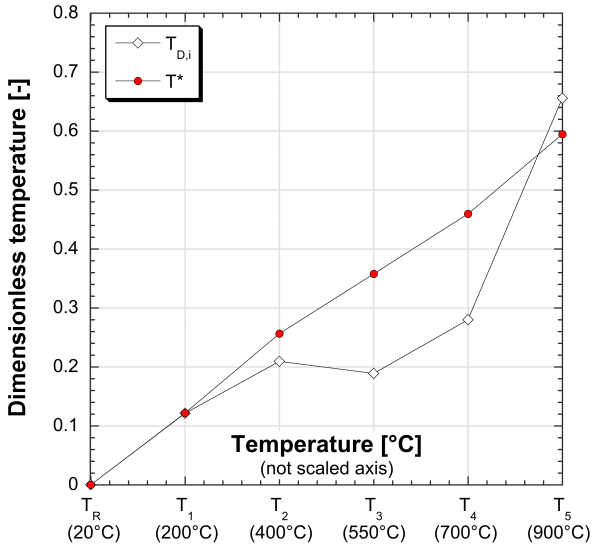

Fig. 5.8 Comparison between the traditional and the modified homologous temperature.

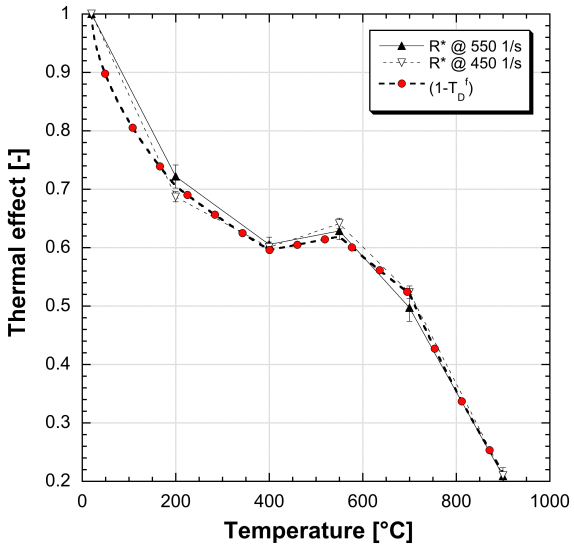

Fig. 5.9 Comparison of the thermal softening factors obtained experimentally (R^*) and the proposed modification of the Johnson-Cook constitutive law (Eq.5.11).

Table 5.3 Parameters for the definition of the dimensionless temperature T_D.

i [-]	$T_{D,i}$ [-]	α_i [-]	T_i [°C]	T range [°C]
0	0	1	20	20÷199
1	0.1216	0.65	200	200÷399
2	0.2095	-0.20	400	400÷549
3	0.1892	0.90	550	550÷699
4	0.2804	2.80	700	700÷900

Chapter 6

Blast effects on steel columns under fire loading

In this Chapter an approach to study the blast effects on steel column under fire conditions is presented. The obtained results will be also helpful in order to validate the implemented material model.

Firstly, a detailed model of a steel column (S355, unprotected HEB260 section) is reported. The effects of the geometry, the boundary conditions, the axial loading and the modelling of blast loads are extensively described. Then, the material properties of the structural steel S355 obtained experimentally at high temperatures and at high loading rates (Chapter 4) are implemented by means of the material constitutive model of Johnson-Cook described in the previous Chapter 5. Lastly, a numerical example study is performed by means of an explicit nonlinear dynamic analysis.

Parts of the results of this Chapter have been included in a paper accepted for publication in the *Journal of Constructional Steel Research* [152].

6.1 Introduction

Analysing the effect of blast loading on civil infrastructures is a difficult task because it involves different and complex aspects, such as structural dynamics, large deformations, dynamics and inelastic material behaviour, complex airblast-structure interactions, the material failure and so on.

Even though advanced numerical simulations have become economical and affordable, the computational effort remains a critical aspect [153]. For that reason a computationally efficient, affordable and not time-consuming numerical simulation, should pass through the choice of the right simplifications.

With these intentions and in order to improve the robustness assessment of structures subjected to a coupled effect of high temperatures and dynamic loads, the behaviour of steel columns under fire conditions followed by an explosion has been studied. Last but not least, this approach is also necessary to validate the proposed method, which starts from a detailed experimental investigation, passes through the definition of a calibrated material model, and ends with a numerical simulation in which both the blast load and the effect of the temperature are considered (Figure 1.4).

6.2 Engineering approach

The approach adopted in this research can be helpful in order to investigate the influence of the implemented dynamic material properties and also to give guidance about the behaviour of steel structures under fire conditions followed by a dynamic event such as a blast load. This not so unlikely event can be the triggering cause of a progressive collapse. For these reasons and with the purpose of considering the triggering threat that could lead to a progressive collapse, a threat specific approach should be considered.

But, it is worth observing that, although the EN 1991-1-7 does not specifically deal with accidental actions caused by external explosions, terrorist attacks and warfare, it is stated that [10][1]:

[1] NOTE 3, clause 3.1(2)

> *Strategies based on unidentified accidental actions cover a wide range of possible events and are related to strategies based on limiting the extent of localised failure. The adoption of strategies for limiting the extent of localised failure may provide adequate robustness against those accidental actions identified in 1.1(6) [e.g. external explosions, terrorist attacks and warfare], or any other action resulting from an unspecified cause.*

In order to limit the extent of localised failures, the EN 1991-1-7 suggests that each critical element (key-element), should be capable of sustaining a notional uniformly distributed load of 34 kN/m^2. But, it is worth noting that this notional load is not a specific overpressure resulting from real situations. On the other hand, the strategies for accidental design situations referring to consequence classes, suggest (in particular for building in CC3) to consider the load-structure interactions by means of sophisticated methods such as dynamic analyses and non-linear material models.

Here, the approach adopts the use of the Johnson-Cook material model [144] described in the previous Chapter 5. Thanks to the experimental investigation in a wide range of strain rates and temperatures, this constitutive material model is able to take into account both the strain rate sensitivity and the thermal softening at high strain rates. A detailed local column investigation is performed through the use of an explicit nonlinear dynamic analysis. The explicit commercial code LS-DYNA [154] version R7.1.1 is used.

These analyses can be helpful for finding out the critical temperatures as well as the critical distances within which a steel column under fire conditions gets seriously damaged by a subsequent blast load. Finally, a comparison with the results obtained adopting a notional distributed load of 34 kN/m^2 is also reported.

6.3 Numerical simulation: a detailed model

6.3.1 Model geometry and boundary conditions

A typical S355 steel column (unprotected HEB260 section, $L = 3.50$m) was considered in this example. This steel column was modelled using fully integrated shell elements with six integration points. A total of 3724 shell elements and 3827 nodes were used to discretise the column. The FE mesh is depicted in Figure 6.1a, while the cross section of the column is reported in Figure 6.1b.

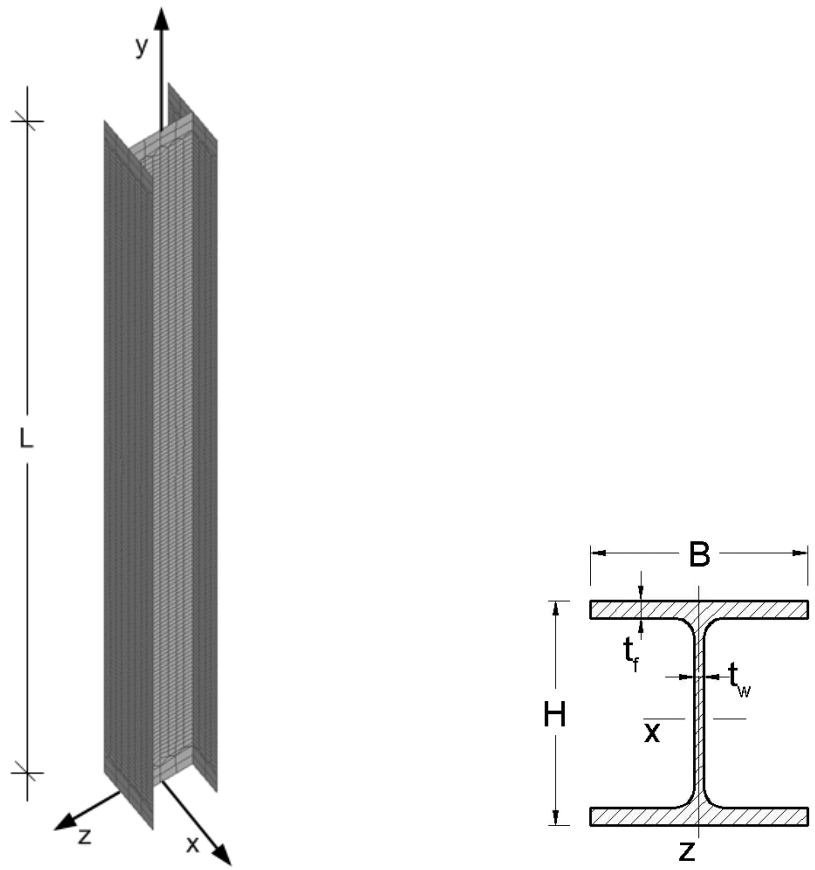

(a) (b)

Fig. 6.1 Coordinate system of the (a) FE column model and for the (b) HEB260 cross section (H = 260 mm, B = 260 mm, t_f = 17.5 mm and t_w = 10 mm).

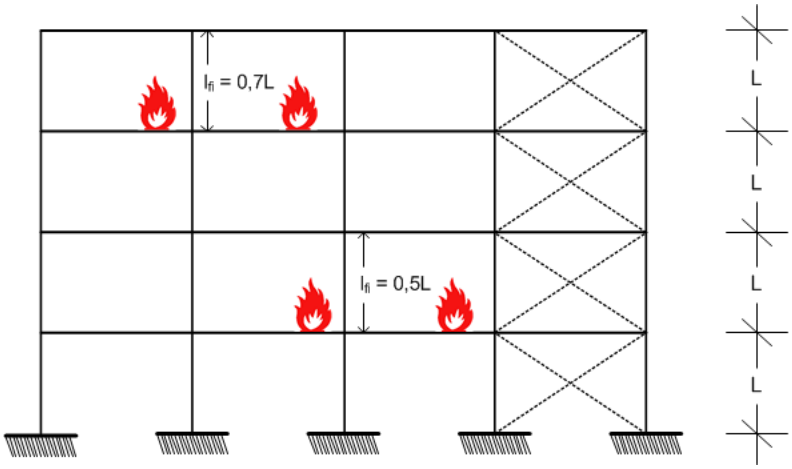

Fig. 6.2 Bucking lengths l_{fi} of columns in a braced frame [70].

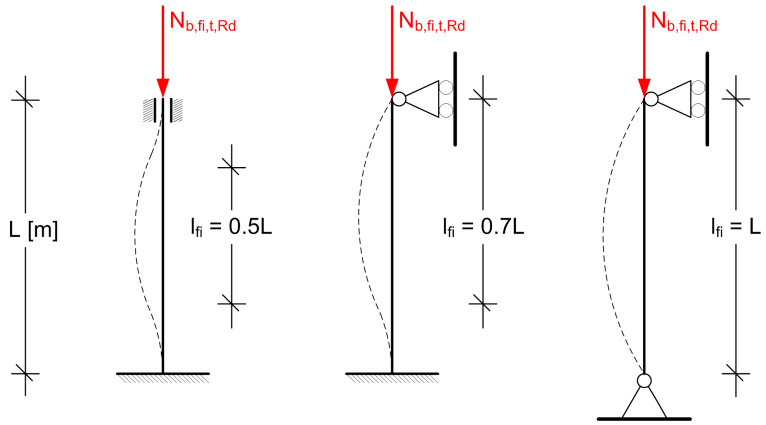

Fig. 6.3 Buckling length for the three column configurations: Fixed-Fixed (left), Fixed-Hinged (center) and Hinged-Hinged (right).

Following the prescription reported on the EN 1993-1-2 [70, 132], different buckling lengths were considered. In case of a braced frame in which each storey comprises a separate fire compartment with sufficient fire resistance, the buckling length may be taken as $l_{fi} = 0.7L$ in the top storey and as $l_{fi} = 0.5L$ in the intermediate storey. L is the column length. See Figure 6.2. In this example three buckling lengths were considered as $l_{fi} = 0.5L$, $l_{fi} = 0.7L$ and also a more conservative hypothesis as $l_{fi} = L$. See Figure 6.3[2]. The knowledge of the behaviour of these three column configurations, is fully representative of events which can occur at any floor of a typical steel braced frame.

[2] The fixed-fixed configuration of the column is not really fixed at the top as it allows for vertical displacement.

6.3.2 Axial loading

On the basis of the prescription reported on the EN 1993-1-2, Part 1-2 [70], the design value of the buckling resistance ($N_{b,fi,t,Rd}$) after 30 minutes (R30) of fire exposure should be determined. To do this, the critical temperature ($\theta_{a,cr}$) after 30 minutes of fire exposure needs to be evaluated.

The critical temperature ($\theta_{a,cr}$) can be determined on the basis of the modified section factor ($k_{sh}[A_m/V]$) for an unprotected (4 sides) HEB260 steel section. This value can be obtained from Vila Real et al. [155] (Annex E) as 79.1 m^{-1}. Then, interpolating from the table for the evaluation of the temperature in unprotected steel members subjected to the standard fire ISO curve [156], the value of $\theta_{a,cr} = 743°C$ is obtained. This is the critical temperature reached after 30 minutes in a unprotected (4 sides) HEB260 steel section subjected to a standard fire ISO.

Then, on the basis of the critical temperature ($\theta_{a,cr}$), the reduction factors for the yield strength ($k_{y,\theta} = 0.1784$) and the Young's modulus ($k_{E,\theta} = 0.1128$) were evaluated by interpolating the values reported on the EN 1993-1-2 [70].

The design value of the bucking resistance can be expressed as:

$$N_{b,fi,t,Rd} = \chi_{fi} \cdot A \cdot k_{y,\theta} \cdot f_y / \gamma_{M,fi} \tag{6.1}$$

where A is the cross sectional area, $k_{y,\theta}$ is the reduction factor for the yield strength, f_y is the yield strength, $\gamma_{M,fi} = 1$ is the partial safety factor for the relevant material property for fire situation and finally, χ_{fi} is the reduction factor for the flexural bucking evaluated as follow:

$$\chi_{fi} = \frac{1}{\phi_\theta + \sqrt{\phi_\theta^2 - \overline{\lambda_\theta^2}}} \tag{6.2}$$

using

$$\phi_\theta = \frac{1}{2} \cdot \left(1 + \alpha\, \overline{\lambda_\theta} + \overline{\lambda_\theta}^2\right) \tag{6.3}$$

with

$$\alpha = 0.65 \cdot \sqrt{235/f_y} \tag{6.4}$$

Finally, $\overline{\lambda_\theta}$ is the non-dimensional slenderness evaluated according to the critical temperature ($\theta_{a,cr}$) as:

$$\overline{\lambda_\theta} = \overline{\lambda} \cdot \sqrt{\frac{k_{y,\theta}}{k_{E,\theta}}} \tag{6.5}$$

where $\overline{\lambda}$ is the non-dimensional slenderness at room temperature evaluated as:

$$\overline{\lambda} = \sqrt{\frac{A \cdot f_y}{N_{CR}}} \tag{6.6}$$

with

$$N_{CR} = \frac{\pi^2 \cdot E \cdot I}{l_{fi}^2} \tag{6.7}$$

The summary results for the three considered buckling lengths are reported in the Table 6.1.

Therefore, in order to cover a worst case scenario, at the beginning of the analysis ($t = 0$ minutes and thus $T = T_{room}$) each column was subjected to its corresponding buckling resistance load ($N_{b,fi,t,Rd}$). See Figure 6.3.

Constraints		Bucking length	$N_{b,fi.t.Rd}$	$\theta_{a,cr}$
Fixed-Fixed	FF	$l_{fi} = 0.5L$	588 kN	743°C
Fixed-Hinged	FH	$l_{fi} = 0.7L$	521 kN	743°C
Hinged-Hinged	HH	$l_{fi} = L$	416 kN	743°C

Table 6.1 Constraints, buckling lengths, bucking resistances and critical temperatures.

6.3.3 Blast under fire loading

During a fire event an explosion could be deliberately or accidentally triggered. If this happens, the blast load can occur between the room temperature ($t = 0$ minutes) and the critical temperature (e.g. $t = 30$ minutes). This is schematically reported in Figure 6.4.

Moreover, on the basis of the standard fire curve ISO 834 [156], it is possible to evaluate the time versus temperature curve in specific unprotected steel members. Using the previously determined modified section factor ($K_{sh}[A_m/V] = 79.1\text{m}^{-1}$)

[132, 155] it is possible to identify the time at which a specific temperature is reached. The time versus temperature curve is reported in Figure 6.5.

An explosion is a very fast phenomenon which lasts only few milliseconds and it results in the production of elevated temperatures and very high pressures.

During the detonation process the produced gases expand in the available space, leading to a propagating pressure front into a surrounding atmosphere. This results in what is called blast wave, which leads to an instantaneous increase from ambient pressure (P_0) to a peak overpressure (P_{S0}). After its peak, the pressure decreases exponentially reaching firstly the ambient pressure and then undergoing into a longer negative pressure phase. In Figure 6.6 a free ideal airblast wave pressure profile is reported. The pressures produced from the negative phase are considerably smaller than those of the positive phase. For that reason the negative phase can be neglected for the design of structures subjected to blast loadings.

The Friedlander equation is commonly used to describe the overpressure-time exponential decay history:

$$p(t) = p_s \cdot (1 - \frac{t}{t_0}) e^{-b\frac{t}{t_0}} \tag{6.8}$$

where p_s is the peak overpressure, t is the time measured after the blast arrival, t_0 is the positive phase duration, while b is a decay coefficient.

Another important parameter, mainly for design purposes, is the impulse of the blast wave. It describes the total force (per unit area) that is applied on a structure due to the blast load. It is defined as the area under the pressure-time curve (see

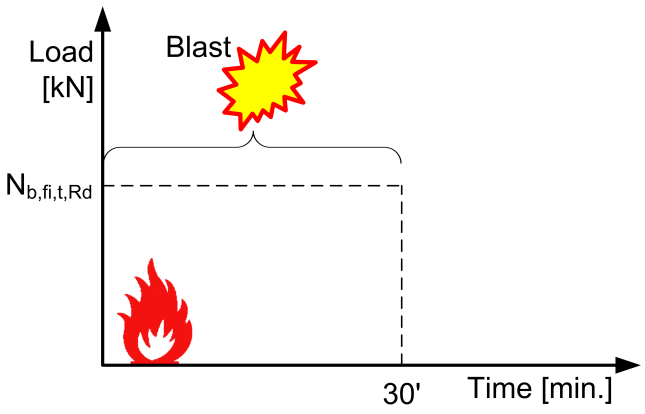

Fig. 6.4 Blast and fire loading timeline.

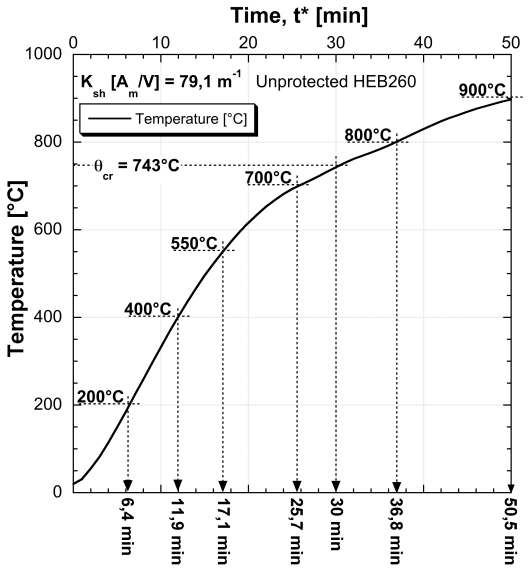

Fig. 6.5 Time versus temperature curve for an unprotected (4 sides) HEB260 steel section.

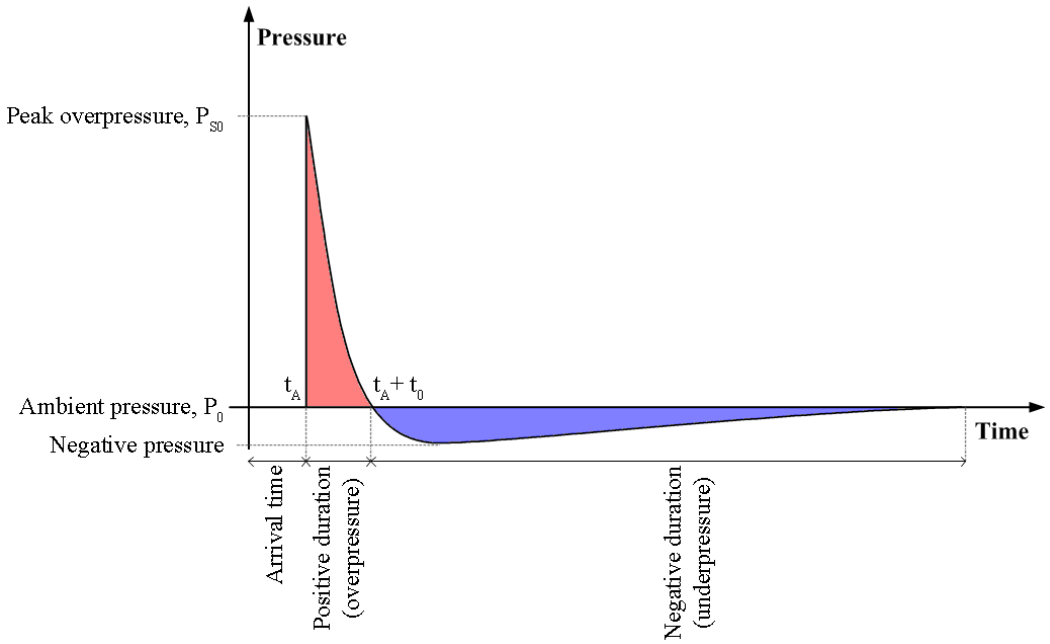

Fig. 6.6 Free ideal airblast wave pressure profile.

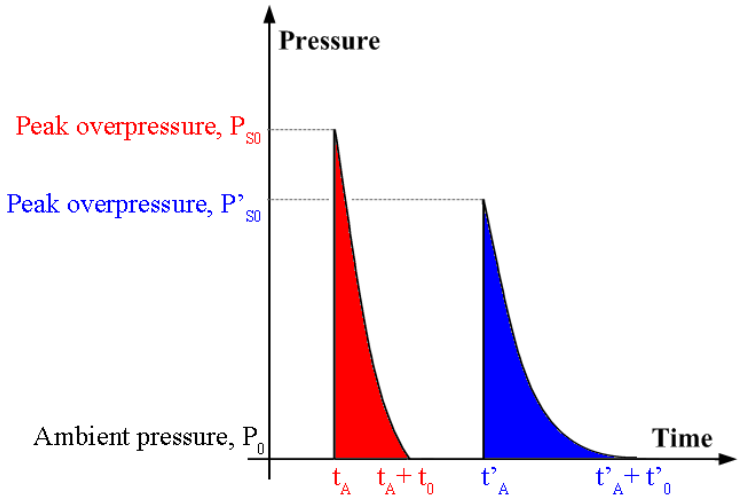

Fig. 6.7 Distance influence on blast wave.

Figure 6.6, where the red area is the positive impulse, while the blue area is the negative impulse). The positive impulse, which is predominantly responsible for damage to structures, is evaluated as:

$$i_s^{(+)} = \int_{t_A}^{t_A+t_0} p(t)dt \tag{6.9}$$

From Figure 6.6 it is also possible to define the arrival time (t_A) as the time taken by the blast wave to reach a target object from the detonation point. It is worth observing that the peak overpressure decreases with the increasing of the distance between the target object and the detonation point (Figure 6.7). As a consequence, the detonation distance, also known as stand-off distance, is a critical parameter for blast loading computations. The effect of the distance is generally taken into consideration by using a scaling law. One of the most widely used is the Hopkinson-Cranz blast wave scaling law [157, 24]. This scaling law establishes that similar explosive waves are produced at identical scaled distances (Z) when two different charges of the same explosive are detonated in the same atmosphere, and is given by:

$$Z = \frac{d}{W^{1/3}} \tag{6.10}$$

where d is the distance from the explosive (in meters), while W is the charge mass in kilograms (usually expressed in equivalent of TNT).

Carrier	Explosive weight
Suitcase	10 kg
Medium-sized car	200 kg
Large-sized car	300 kg
Pick-up truck	1400 kg
Van	3000 kg
Truck	5000 kg
Truck with trailer	10000 kg

Table 6.2 Indicative charge weight, from [24].

Type of explosive	TNT equivalent mass factor	
	Peak pressure	Impulse
TNT	1.00	1.00
C3	1.08	1.01
C4	1.37	1.19
CYCLOTOL	1.14	1.09
OCTOL 75/25	1.06	1.06
TETRYL	1.07	1.05
HMX	1.02	1.03
AMATOL	0.99	0.98
RDX	1.14	1.09
PETN	1.27	1.11

Table 6.3 Indicative TNT equivalent mass factors, from [24].

The explosive charge is positioned at the mid column height (Figure 6.8a) and along the strong axis (x-axis) of the section. The expected response is mainly bending about the weak axis (z-axis) with the least moment of inertia (Figure 6.8b). The influence of the distance (d) between the target surface (column) and the blast source can be evaluated by moving the charge load along the x-axis.

Another important aspect is the weight of the explosive. This is generally estimated by taking into account a relevant attack scenario [24]. In Table 6.2 an estimate of the explosive weights that could be transported by various vehicle types are reported. Furthermore, it is useful to express the charge weight W as an equivalent mass of TNT, then the corresponding masses for other explosives can be obtained through the concept of TNT equivalence [27]. In Table 6.3 some indicative TNT equivalent mass factors are reported.

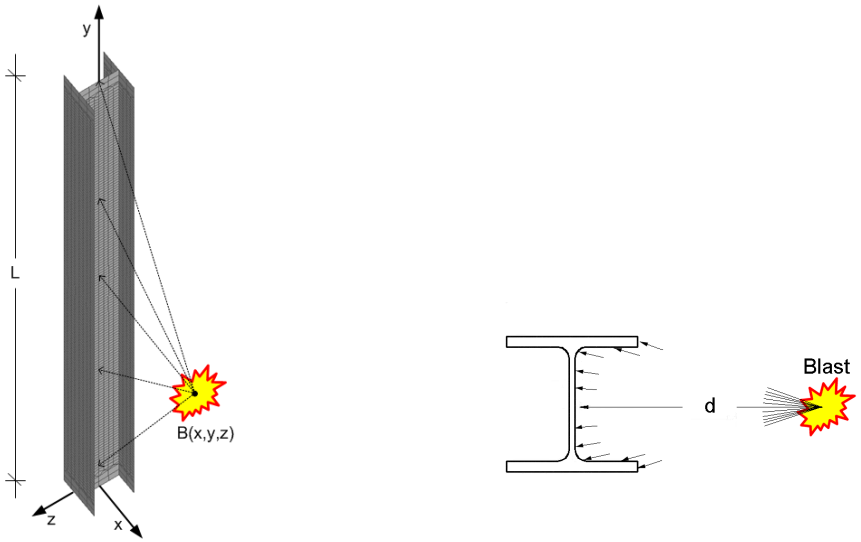

(a) (b)

Fig. 6.8 Blast charge positioning: (a) 3D view of the FE column model and (b) cross section view.

In order to consider all these aspects such as the peak overpressure, the effect of the detonation distance and the blast charge, numerous models are available in literature. The approach adopted in this numerical model is based on the empirical model CONWEP, described in the TM 5-855-1 US ARMY [158]. This model is available in LS-DYNA using the `*LOAD_BLAST` airblast function. An air burst spherical charge was adopted. The range of applicability for the spherical air burst is $0.147\ \text{m/kg}^{1/3} < Z < 40\ \text{m/kg}^{1/3}$ [154], where Z is the scaled distance (Eq. 6.10). Adopting the `*LOAD_BLAST` function the blast pressure is applied to each shell element directly exposed to the blast wave (Figure 6.8). The blast pressure is evaluated as a function of the distance (from the specific shell element to the blast source) and the angle of incidence.

6.3.4 Material modeling

The material properties of the structural steel S355 obtained experimentally at high temperatures and high loading rates were adopted in the numerical simulation by using the `*MAT_JOHNSON_COOK` material model. This is the LS-DYNA material model type `*MAT_015`, which refers to Eq. 5.1.

Material model	Johnson-Cook [144]
LS-DYNA material model	*MAT_015
Elastic modulus	$E_{a,\theta} = k_{E,\theta} \cdot E_a$
Density	7890 kg/m^3
Poisson ratio	0.315
Failure strain	0.4

Table 6.4 Parameters for the Johnson-Cook analysis.

Other adopted parameters are reported in Table 6.4. It is worth noting that the elastic modulus was chosen as a function of the temperature considering the reduction factor reported on the EN 1993-1-2 [70].

6.3.5 Validation of the numerical model

The material adopted in the numerical model is the same material used for steady state column tests described in the technical report *Experiments on steel columns under fire conditions* [159]. For that reason some numerical simulations comparing the results with those reported by Pauli et al. [159] have been performed. The numerical model geometry has been adapted to be comparable to the experimental conditions (*steady state slender HEA100 column centrically loaded; L = 1.84 m; pin-ended conditions*). A satisfactory agreement between the ultimate load[3] evaluated numerically at room temperature and the real test data has been found. For the sake of completeness the results are reported in the following Table 6.5.

Labelling from [159]	Temperature	Experimental ultimate load [159]	Numerical ultimate load
HEA100_SL_20C_z0	20°C	671 kN	610 kN (−10%)
HEA100_SL_20C_y0	20°C	859 kN	760 kN (−11%)
HEA100_SL_400C_z0	400°C	466 kN	454 kN (−3%)

Table 6.5 Experimental and numerical comparison. The label "y0" means y-axis (strong axis) pin-ended, while the label "z0" means z-axis (weak axis) pin-ended.

The numerical model has been also validated comparing the results with data of test steel columns under blast loads. A satisfactory agreement with the experimental

[3] Maximum load evaluated before the column buckling.

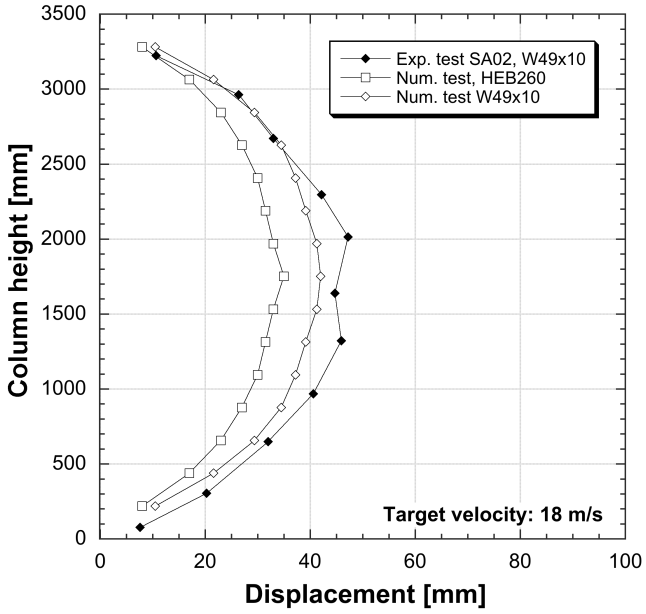

Fig. 6.9 Numerical and experimental horizontal displacement.

results reported in the PhD thesis *Testing and analysis of structural steel columns subjected to blast loads* [160] has been found. In that PhD thesis the experimental tests were performed on steel columns with dimensions, section size and material similar to the considered numerical model. The following Figure 6.9 reports the lateral displacement comparison between an experimental configuration (*Test SA02*, [160]) and a numerical model in which similar loading and boundary[4] conditions were imposed. The horizontal displacement obtained numerically is slightly lower than the experimental results (-30%). This is probably due to the different moment of inertia of the steel column tested experimentally (W49x10, $J = 1.13 \cdot 10^8$ mm^4) and the moment of inertia of the steel column adopted in the numerical model (HEB260, $J = 1.49 \cdot 10^8$ mm^4). When performing a numerical simulation with the same section used in the experimental tests the difference is lower. The horizontal displacement evaluated numerically is underestimated (at mid-height) by about 7%.

[4] Fixed at the base, while the top of the column is free to move only vertically.

6.4 Example study

The blast effect on the three column configurations (Figure 6.3) under fire loading was evaluated from the room temperature up to 900°C. The approach followed is described below and is based on the following assumptions:

1. The charge weight is chosen assuming that the explosive is carried in a medium-sized suitcase. In order to consider a worst-case scenario the charge weight of the explosive is set to 20 kg of equivalent TNT, twice the value suggested by Karlos and Solomos [24]. The corresponding masses for other explosive types can be obtained through the concept of TNT equivalence.

2. The influence of the distance (d) between the target surface (column) and the blast source is studied considering six configurations, as reported in the following Table 6.6. Notwithstanding that $d_1 = 0.75$ m is a close-in detonation, the corresponding scaled distance ($Z = 0.276$ m/kg$^{1/3}$) is within the range of validity (0.147 m/kg$^{1/3} < Z <$ 40 m/kg$^{1/3}$ [154]) for a spherical air blast and using the *LOAD_BLAST airblast function. For that reason this case is treated for simplicity as the other cases.

	$d(x)$	y	z	Charge	Z
Case d_1	0.75 m	1.75 m	0.00 m	20 kg	0.276 m/kg$^{1/3}$
Case d_2	1.00 m	1.75 m	0.00 m	20 kg	0.368 m/kg$^{1/3}$
Case d_3	2.00 m	1.75 m	0.00 m	20 kg	0.737 m/kg$^{1/3}$
Case d_4	3.00 m	1.75 m	0.00 m	20 kg	1.105 m/kg$^{1/3}$
Case d_5	5.00 m	1.75 m	0.00 m	20 kg	1.842 m/kg$^{1/3}$
Case d_6	10.0 m	1.75 m	0.00 m	20 kg	3.684 m/kg$^{1/3}$

Table 6.6 Six analysed configurations: coordinates of the charge.

3. A direct exposure of the column to the blast pressure is assumed. This means that a worst case scenario is considered because the effects of protective elements are neglected.

4. The blast waves transmitted through the floors and reflected from the walls are ignored.

5. The temperature rise due to the blast waves is ignored. The simplification due to this assumption leads to a negligible error.

6. A homogeneous temperature distribution within the whole column is assumed. Keeping a constant temperature is a computational time-saving simplification. Moreover, this choice leads to an easier implementation of the Johnson-Cook material model in LS-DYNA. This because the thermal softening sensitivity parameter (m) can be directly imposed as a function of the temperature (see Figure 5.5 and Table 5.2). Thus, if the temperature is kept constant, this approach leads to thermal softening terms $(1 - T^m)$ in accordance with the experimental data (Figure 5.7).

7. At the beginning of the simulation ($t_{s,0}$) and in order to reach the initial equilibrium, the column is initialised with a static routine using the command `*CONTROL_DYNAMIC_RELAXATION`. An explicit phase follows to evaluate the blast effects.

The beginning of a simulation ($t_{s,0}$) starts imposing a specific temperature to the numerical model. This temperature could be obtained from Figure 6.5, in which the time-temperature behaviour of the HEB260 section is reported during a fire situation. At this time ($t_{s,0}$) the column is also supposed to be under the axial loading $N_{b,fi,t,Rd}$ (Table 6.1 and Figure 6.3). At the same time a blast charge of 20 kg of TNT was applied. In order to understand the effect of the blast distance, different analyses were performed by changing the position of the charge (Table 6.6). Then, at the time $t_{s,1}$ a vertical displacement at the top of the column was imposed to evaluate the residual load bearing capacity. The time $t_{s,1}$ was chosen as the instant within the first milliseconds, at which the blast produces the first maximum lateral displacement of the column. For the sake of clarity, the timeline of the numerical simulations is reported in Figure 6.10.

A total of 108 numerical simulations were performed: three buckling length configuration (Table 6.1), six temperatures (20°C, 200°C, 400°C, 550°C, 700°C and 900°C) and six blast charge positions (Table 6.6).

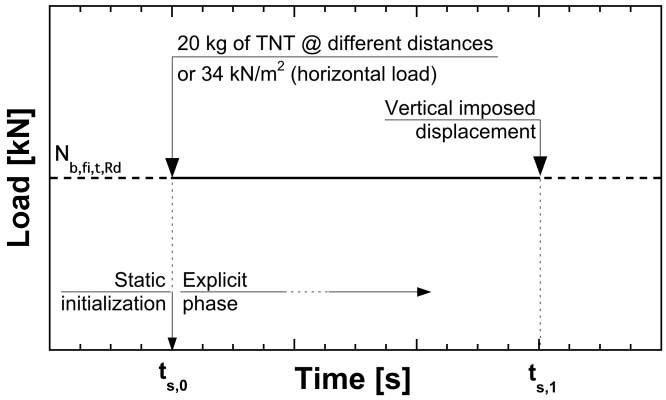

Fig. 6.10 Timeline of the numerical simulations. The $N_{b,fi,t,Rd}$ value is selected accordingly to the column configuration (Table 6.1).

6.4.1 Eurocode approach

The approach stated on the EN 1991-1-7 considers a lateral load equal to 34 kN/m^2 instead of a blast load. In order to compare the results obtained considering both approaches the lateral load was imposed in the same direction of the blast load, thus along the x-axis. The numerical model of the column, the boundary conditions and the axial loadings were the same described in the previous Paragraph 6.3.

The material constitutive law for carbon steel at elevated temperatures reported on the EN 1993-1-2 [70] (Figure 6.11) was adopted. The material model adopted in the numerical simulations is the `*MAT_PIECEWISE_LINEAR_ PLASTICITY`. In LS-DYNA this is the material model type `*MAT_024`. This material model is appropriate to implement elasto-plastic materials with an arbitrary stress versus strain curve. The elastic modulus was chosen as a function of the temperature considering the reduction factor reported on the EN 1993-1-2 [70]. The parameters adopted are reported in Table 6.7.

It is worth noting that following this approach it is not possible to evaluate a critical distance.

A total of 24 numerical simulations were performed. Three buckling length configurations (Table 6.1) and eight temperatures (20°C, 200°C, 400°C, 500°C, 600°C, 700°C, 800°C and 900°C). The results are included in Figures 6.16a-6.18a

Material model	EN 1993-1-2 [70]
LS-DYNA material model	*MAT_024
Elastic modulus	$E_{a,\theta} = k_{E,\theta} \cdot E_a$
Density	7890 kg/m^3
Poisson ratio	0.315
Effective plastic stress versus strain values	See Figure 6.11

Table 6.7 Parameters for the simplified analysis.

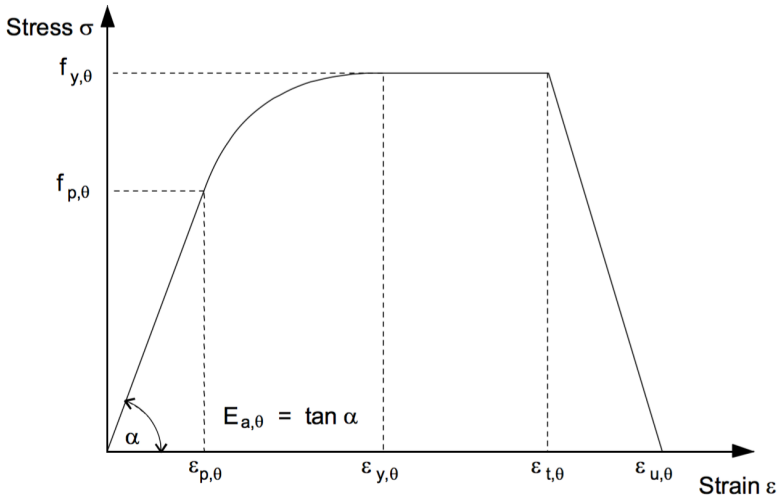

Fig. 6.11 Stress versus strain curve for carbon steel at elevated temperatures [70].

6.5 Results and discussion

In order to study the blast effects on steel columns under fire loadings as well as to evaluate the applicability and the usability of the implemented material model of Johnson-Cook, the residual load bearing capacity and the instantaneous lateral displacement at mid-height were considered.

The residual vertical load bearing capacity was evaluated as the maximum load reached when the top of the column is subjected to a vertical imposed displacement. Beyond this load, failure of the column due to lateral instability occurs. The displacement is applied to a rigid body located at the top of the column. The vertical reaction force of the rigid body gives the compressive force to which the column is subjected. It is worth noting that this force includes also the $N_{b,fi,t,Rd}$ load (Figure 6.1), which is already applied at the top of the column. The time at which the vertical displacement is imposed corresponds to t_{s1}, while for $t < t_{s1}$ only the blast load and the $N_{b,fi,t,Rd}$ are applied (Figure 6.10). For the sake of clarity, this is reported in Figure 6.12, where the residual load bearing capacity is depicted as a function of time and temperature. Clearly, in the event that the blast load destroys the column, this technique cannot be applied as this constitute a failure by itself.

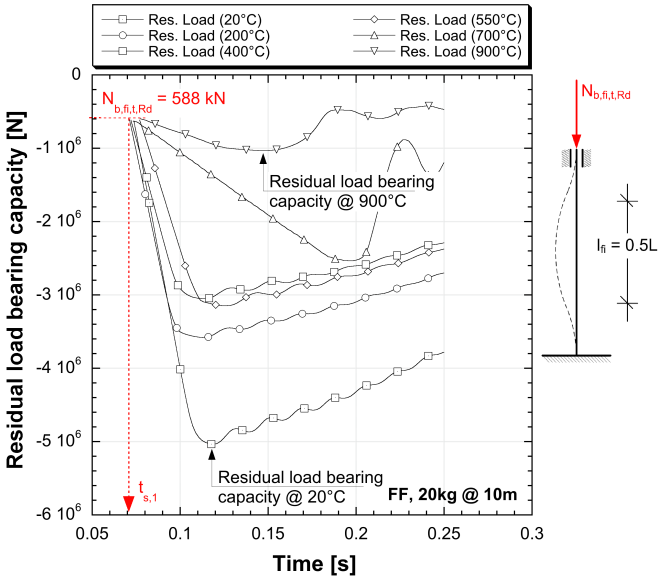

Fig. 6.12 Residual load bearing capacity versus time. Fixed-Fixed column configuration and stand-off distance of 10 meters.

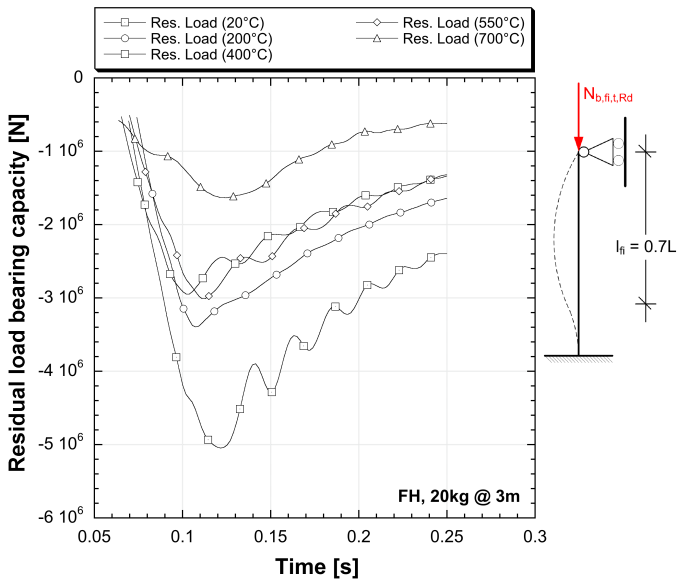

Fig. 6.13 Residual load bearing capacity versus time. Fixed-Hinged column configuration and stand-off distance of 3 meters.

In Figure 6.12 the Fixed-Fixed (FF) column configuration with the blast load located at a stand-off distance of 10 meters is reported. Other two column configuration are reported in Figure 6.13 and Figure 6.14. In Figure 6.13 the residual load bearing capacity is depicted for the Fixed-Hinged (FH) configuration with a stand-off distance of 3 meters, while in Figure 6.14 the Hinged-Hinged (HH) configuration with a stand-off distance of 5 meters is reported. Curves depicted from Figure 6.12 to Figure 6.14 were fitted using the locally weighed least square error method [161] using the data analysis software KaleidaGraph version 4.5.2. The local weight was set to 3%. Five frames recorded during a numerical simulation are reported in Figure 6.15.

Changing the blast detonation distance and the temperature, the residual vertical load bearing capacity was evaluated for the three buckling length configurations. A total of 108 numerical simulations were performed. The results are reported in Table 6.8, and for the sake of completeness, the results are also graphically depicted from Figure 6.16 to Figure 6.18. In these Figures the lateral displacements at mid-height of the column are reported as well. These values were evaluated as the horizontal displacement immediately after the blast load. Thus, this horizontal diplacement can be a useful parameter in order to understand the column response to the peak overpressure. Data in these graphs are depicted as a function of the

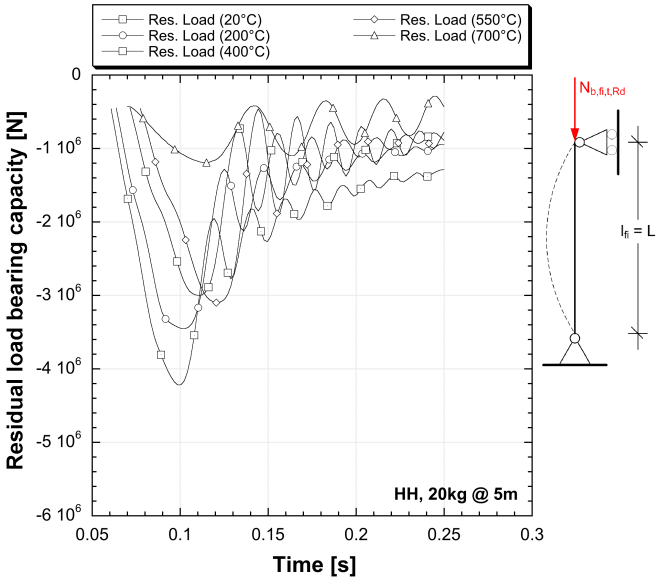

Fig. 6.14 Residual load bearing capacity versus time. Hinged-Hinged column configuration and stand-off distance of 5 meters.

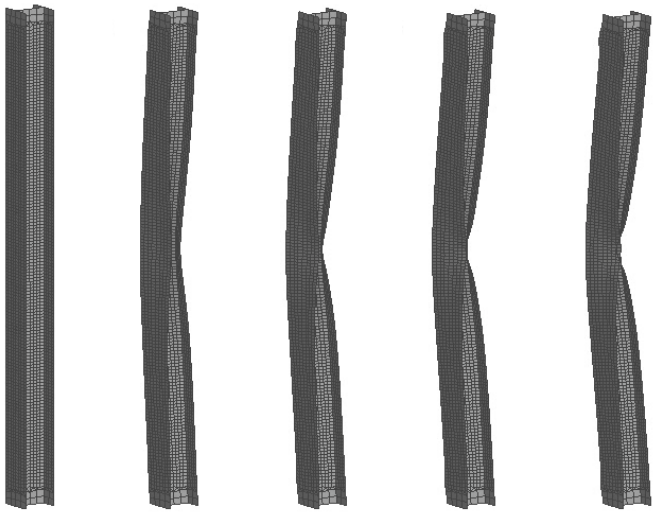

Fig. 6.15 Frames acquired during a numerical simulation (FF, 20kg of eq. TNT at 1 m and 550°C).

Fixed-Fixed configuration ($l_{fi} = 0.5$, $N_{b,fi,t,Rd} = 588$ kN)						
	10 m	5 m	3 m	2 m	1 m	0.75 m
20°C	5038 kN	5089 kN	5140 kN	4927 kN	4133 kN	3460 kN
200°C	3580 kN	3605 kN	3552 kN	3396 kN	2601 kN	1978 kN
400°C	3054 kN	3103 kN	3015 kN	2866 kN	2152 kN	1241 kN
550°C	3148 kN	3183 kN	3099 kN	2968 kN	2332 kN	1312 kN
700°C	2536 kN	2550 kN	2301 kN	1775 kN	Failure	Failure
900°C	1032 kN	934 kN	812 kN	Failure	Failure	Failure

Fixed-Hinged configuration ($l_{fi} = 0.7$, $N_{b,fi,t,Rd} = 521$ kN)						
	10 m	5 m	3 m	2 m	1 m	0.75 m
20°C	4918 kN	5177 kN	5047 kN	4633 kN	3440 kN	2301 kN
200°C	3460 kN	3561 kN	3395 kN	3195 kN	2056 kN	431 kN
400°C	2963 kN	3032 kN	2948 kN	2674 kN	1421 kN	Failure
550°C	3047 kN	3157 kN	3013 kN	2731 kN	1368 kN	Failure
700°C	2485 kN	1683 kN	1636 kN	1538 kN	Failure	Failure
900°C	880 kN	679 kN	Failure	Failure	Failure	Failure

Hinged-Hinged configuration ($l_{fi} = 1.0$, $N_{b,fi,t,Rd} = 416$ kN)						
	10 m	5 m	3 m	2 m	1 m	0.75 m
20°C	4849 kN	4219 kN	4397 kN	3708 kN	2325 kN	1312 kN
200°C	3396 kN	3453 kN	3082 kN	2799 kN	1135 kN	Failure
400°C	2949 kN	3000 kN	2777 kN	2363 kN	Failure	Failure
550°C	3010 kN	3098 kN	2832 kN	2422 kN	Failure	Failure
700°C	1905 kN	1192 kN	1189 kN	1157 kN	Failure	Failure
900°C	616 kN	Failure	Failure	Failure	Failure	Failure

Table 6.8 Residual load bearing capacities

detonation distance and the time (or temperature). It is worth noting that the time-temperature relation was evaluated on the basis of the standard fire curve ISO 834 (Figure 6.5).

From Figure 6.16b to Figure 6.18b it is possible to observe that, when the initial lateral displacement is lower than 50 mm (approximately 1.5% of out-of-plane with respect to the total column height), a robust behaviour is observed, even at very high temperatures.

The comparison between the lateral displacements data at 400°C and 550°C leads to the following consideration. In the range from 400°C to 550°C a slight increase of strength is noted experimentally (see Figures 4.8, 4.9 and 4.10). As a consequence

Fixed-Fixed configuration ($l_{fi} = 0.5$, $N_{b,fi,t,Rd} = 588$ kN)						
	10 m	5 m	3 m	2 m	1 m	0.75 m
20°C	2.1 mm	5.9 mm	11.7 mm	20.8 mm	61.9 mm	98.9 mm
200°C	2.3 mm	6.3 mm	12.8 mm	25.8 mm	81.5 mm	138.9 mm
400°C	2.8 mm	7.3 mm	14.7 mm	30.0 mm	96.1 mm	182.2 mm
550°C	3.2 mm	8.3 mm	15.8 mm	30.8 mm	96.2 mm	180.5 mm
700°C	8.3 mm	19.2 mm	36.1 mm	58.8 mm	Failure	Failure
900°C	13.3 mm	33.6 mm	87.8 mm	Failure	Failure	Failure

Fixed-Hinged configuration ($l_{fi} = 0.7$, $N_{b,fi,t,Rd} = 521$ kN)						
	10 m	5 m	3 m	2 m	1 m	0.75 m
20°C	3.3 mm	9.0 mm	16.9 mm	30.0 mm	84.9 mm	136.7 mm
200°C	3.6 mm	9.3 mm	19.1 mm	36.0 mm	112.2 mm	473.3 mm
400°C	4.4 mm	11.0 mm	21.8 mm	42.4 mm	140.8 mm	Failure
550°C	4.7 mm	11.9 mm	23.4 mm	43.6 mm	139.7 mm	Failure
700°C	12.7 mm	29.4 mm	55.1 mm	93.2 mm	Failure	Failure
900°C	20.9 mm	57.4 mm	Failure	Failure	Failure	Failure

Hinged-Hinged configuration ($l_{fi} = 1.0$, $N_{b,fi,t,Rd} = 416$ kN)						
	10 m	5 m	3 m	2 m	1 m	0.75 m
20°C	5.9 mm	14.0 mm	27.2 mm	47.0 mm	137.5 mm	232.5 mm
200°C	6.3 mm	15.0 mm	29.7 mm	57.0 mm	198.0 mm	Failure
400°C	7.4 mm	16.7 mm	34.7 mm	67.7 mm	Failure	Failure
550°C	8.0 mm	18.7 mm	36.4 mm	69.3 mm	Failure	Failure
700°C	21.7 mm	51.3 mm	96.3 mm	175.0 mm	Failure	Failure
900°C	54.0 mm	Failure	Failure	Failure	Failure	Failure

Table 6.9 Lateral displacement (at mid-height and along the x-axis).

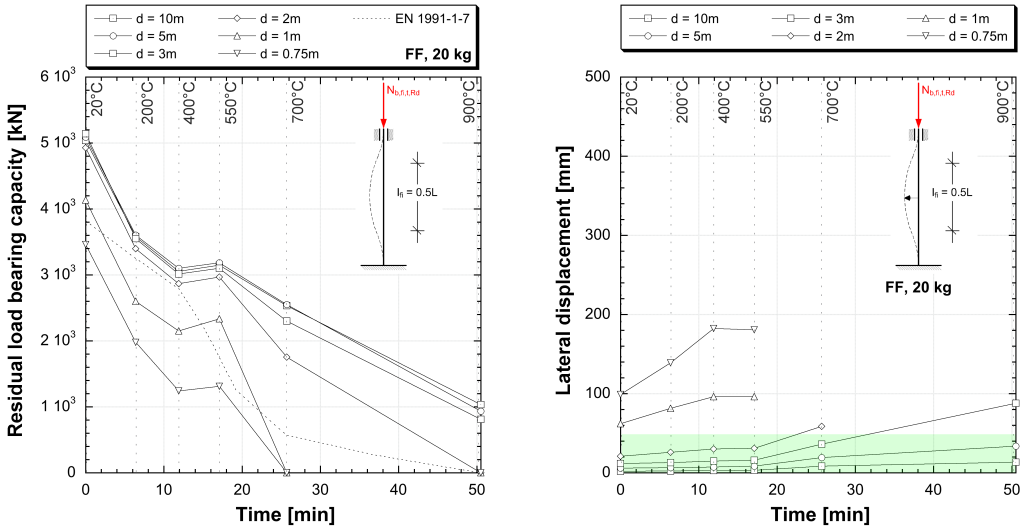

(a) Residual load bearing capacity (b) Lateral displacement (at mid-height)

Fig. 6.16 Fixed-Fixed ends

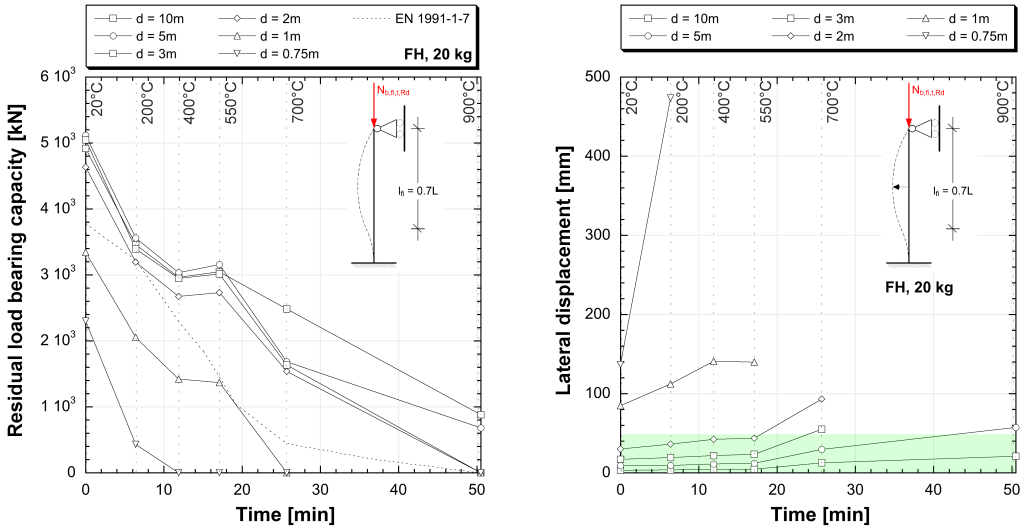

(a) Residual load bearing capacity (b) Lateral displacement (at mid-height)

Fig. 6.17 Fixed-Hinged ends

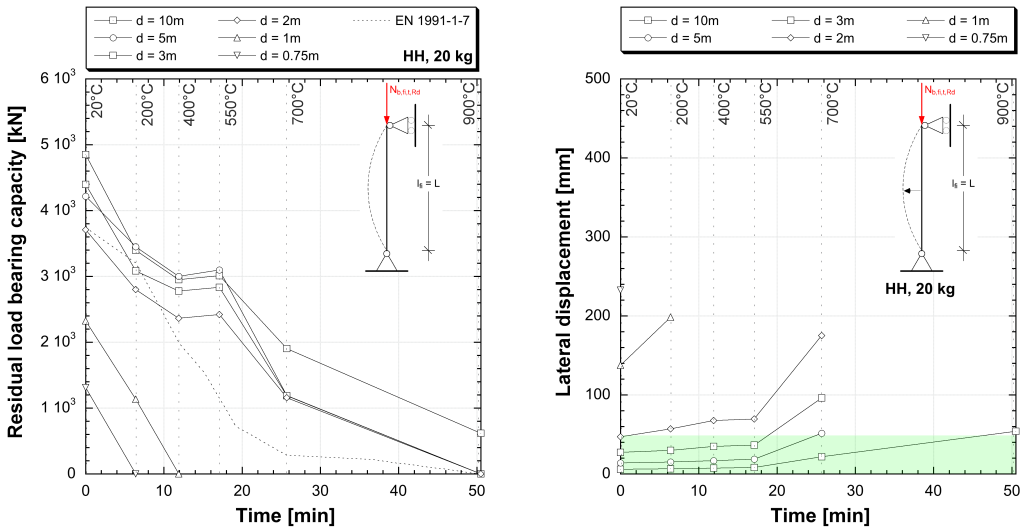

(a) Residual load bearing capacity (b) Lateral displacement (at mid-height)

Fig. 6.18 Hinged-Hinged ends

the lateral displacement at 550°C should be lower than at 400°C. But this is observed only due to explosions at the close proximity. This means that in some configurations the first deformation (at mid-height) due to the blast overpressure is in the elastic regime. On the other hand, in other configurations (mainly due to explosions in the close proximity or at very high temperatures) the peak overpressure leads to deformations (at mid-height) in the plastic regime. This is the reason why in the range between 400°C and 550°C only explosions in close proximity lead to lower lateral displacements at 550°C than 400°C. This confirms that the Johnson-Cook plastic flow material model plays a key role in the numerical simulations.

From Figure 6.16a to Figure 6.18a it is possible to note a general dramatic reduction ($\sim 40\%$) of the residual load bearing capacity due to explosions in the first 10 minutes of fire loading. Moreover, both the FF and FH configurations show a similar trend for blast loads in the range from 10 m to 2 m. In this range of distance these two configurations do not seem to be strongly influenced by blast loads, with the exception of explosions at very high temperature (900°C).

On the other hand, explosions in the close proximity ($d < 2$ m) lead to a higher level of damage. In particular in the FF configuration a complete failure occurs due to explosions triggered after about 20 minutes of fire loading. The HH configuration is the most critical: blast loads within the first 12 minutes lead to a complete failure

of a HEB260 steel column. Finally, it is worth noting that blast events at $d < 0.75\,\text{m}$ lead to complete failures.

From Figure 6.16a to Figure 6.18a it is also possible to recognise a slight increase of the residual load bearing capacity between 400°C and 550°C, while a new marked decrease is noticed up to 900°C. A strength increase in this range of temperatures has been noted also experimentally (see Figures 4.8, 4.9 and 4.10) and is ascribed to the dynamic strain ageing. This is another confirmation of the reliability of the adopted material model which is able to represent the mechanical properties of the S355 structural steel obtained experimentally at high temperatures and in a wide range of strain rates.

The use of the notional lateral load of 34 kN/m^2, suggested by the EN 1991-1-7 [10], leads to different limitations. The main issue is the impossibility to evaluate the critical detonation distance as well as the critical charge of the explosive. This is highlighted comparing the results obtained following a more detailed numerical model. From Figure 6.16a to Figure 6.18a it is indeed possible to observe that the residual load bearing capacity for the HEB260 steel column is generally underestimated for detonation distances higher than 2 meters. On the contrary, the residual load bearing capacity is overestimated for explosions in the close proximity ($1 \div 0.75\,\text{m}$).

Finally, it is worth observing that the obtained results, mainly for the explosion in the close proximity, are based on the simplified assumption that also the close-in detonations produce standard overpressure-time curves (eq. 6.8). However, recent studies [162–164] have shown that at very small distances from the explosive more complex phenomena take place due to after-burning and the violent outflow of the detonation gases, leading to higher values of the overpressure and impulse.

6.5.1 Comments concerning the strain rate

The adopted material model (`*MAT_JOHNSON_COOK`) has been experimentally calibrated in a wide range of temperatures ($20 \div 900$°C) and strain rates ($0.001 \div 850\,\text{s}^{-1}$).

It is worth pointing out that the parameters of the thermal softening term (Eq. 5.11) were evaluated from experimental tests performed in the typically expected range of strain rates which take place during blast events ($10^2 \div 10^3\,\text{s}^{-1}$). In particular, two set of experimental data with comparable effective strain rates

Strain rate	Eq. 6.11 gives	Difference
$450\,s^{-1}$	1.151	n.d.
$550\,s^{-1}$	1.156	+0.43%
$100\,s^{-1}$	1.114	−3.23%
$10\,s^{-1}$	1.057	−8.17%

Table 6.10 Influence of strain rate in Eq. 6.11 ($c = 0.0247$).

($450\,s^{-1}$ and $550\,s^{-1}$) were used. In spite of that, the obtained thermal effect trends from both these set of data were very similar (see Figure 5.7). The thermal effect term is strongly influenced by the temperature.

In the numerical model the strain rates in this range were obtained only locally (at mid-height of the column) due to the blast overpressure and as a consequence of explosions in the close proximity ($d < 2\,m$). On the other hand explosive charges located at greater stand-off distances ($d \geq 2\,m$) lead to local strain rates lower than $10^2\,s^{-1}$.

Supposing that the thermal softening term trend (see Figure 5.7) is similar also at lower strain rates (e.g. $10^1 \div 10^2\,s^{-1}$), but this could be confirmed only performing more experimental tests, the strain rate influence in the Johnson-Cook material model is totally governed by the strain rate hardening term:

$$(1 + c \cdot ln\frac{\dot{\varepsilon}}{\dot{\varepsilon}_0}) \tag{6.11}$$

The influence of the strain rate in the previous Eq. 6.11 is reported in Table 6.10. It is possible to observe the limited (0.43%) difference in the hardening parameter when the strain rate moves from $450\,s^{-1}$ to $550\,s^{-1}$. In addition, the difference is of about 3% for strain rates equal to $10^2\,s^{-1}$, while in the range between $10^1\,s^{-1}$ and $10^2\,s^{-1}$ the maximum variation is of about 8%. It is worth noting that these variations are on the safe side, meaning that for strain rates lower than $450\,s^{-1}$ (or $550\,s^{-1}$) the plastic flow stress is underestimated by the implemented Johnson-Cook material model.

On the basis of the definition of the scaled distance (Z), another consideration can be made. Strain rates in the range ($10^2 \div 10^3\,s^{-1}$) were obtained in the numerical model as a consequence of the peak overpressure and impulse due to explosions in the close proximity ($Z = 0.368\,m/kg^{1/3}$ or 20 kg of equivalent TNT @ 1 m). Under this scaled distance the implemented numerical model is valid for blast events between 200°C and 900°C. This is reported graphically in Figure 6.19, where the

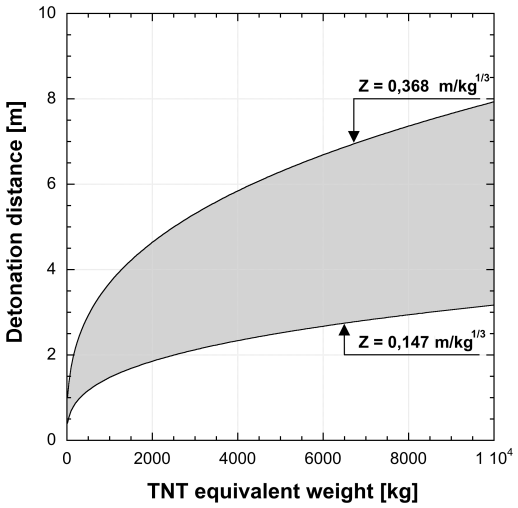

Fig. 6.19 Scaled distance range in which blast loads are expected to generate a rate of deformation from $10^2\,\mathrm{s}^{-1}$ to $10^3\,\mathrm{s}^{-1}$ within steel columns.

value of $Z = 0.147\,\mathrm{m/kg}^{1/3}$ has been imposed as the lower limit of applicability for the spherical air burst [154]. Inside the limits of the grey area the peak overpressure is expected to generate, within steel columns, a rate of deformation between $10^2\,\mathrm{s}^{-1}$ and $10^3\,\mathrm{s}^{-1}$. However, this should be verified performing more numerical simulations by changing the cross section. On the other hand, at room temperature the implemented numerical model is fully valid in a wide range of dynamic events. This is because the material model at room temperature was calibrated from $0.001\,\mathrm{s}^{-1}$ to $850\,\mathrm{s}^{-1}$. As mentioned above, these observations are based on the simplified assumptions that the close-in detonations produce standard overpressure-time curves.

Finally, for a fixed detonation distance, or in other words for the same peak overpressure, an increase of the local strain rate was observed at elevated temperatures. This phenomenon was highlighted also experimentally (Figure 4.11) and is another confirmation of the good reliability of the implemented material model.

Chapter 7

Conclusions and future developments

This chapter summarises the findings, the conclusions as well as the future developments of the research.

7.1 Conclusions

The main objectives of this thesis were, on the one hand to present a comprehensive but simplified approach to progressive collapse of steel structures under the coupled effect of fire and blast, on the other hand to evaluate the applicability and the usability of the material model which has been calibrated after an extensive experimental investigation.

The core idea was to study, by means of a nonlinear dynamic analysis, the blast response of a steel column under fire loadings. To do this, a constitutive material model able to take into account both the strain rate hardening and the thermal softening has been considered. This is the main reason why the real mechanical properties under a wide range of strain rates and temperatures are inevitably necessary to calibrate the material model.

First of all, the available experimental techniques to study the dynamic behaviour of materials have been introduced. Then, after having selected a widely used structural steel in the construction field, namely S355, an extensive experimental investigation was carried out by means of uniaxial tensile tests. A hydro-pneumatic machine was used to perform dynamic tensile tests at room temperature and medium strain-rate regime ($5 \div 25\,\mathrm{s}^{-1}$). In addition, at room temperature a universal electro-mechanical testing machine was used to perform quasi-static tests. On the other hand, a split Hopkinson tensile bar apparatus equipped with a water-cooled induction heating system was used to perform high strain rate tests ($300 \div 850\,\mathrm{s}^{-1}$) in a wide range of temperatures ($20 \div 900\,^{\circ}\mathrm{C}$).

These unique results [8, 9] showed, at room temperature, that the S355 structural steel is moderately strain rate sensitive on both the strength and the fracture strain. However, the material kept its strain hardening capacities with increasing strain rates. At high temperatures, the ratio of the value of a specific mechanical property at elevated temperatures to the corresponding value at room temperature was used to compare dynamic tests at the same testing condition. Even if a marked difference between quasi-static and high strain rate reduction factors is clearly observable (Figure 4.13(a)), the tensile properties do not seem to be strongly influenced by the three different dynamic testing conditions (Figure 4.13 and Figure 4.14). On the other hand, a noticeable increase in the effective strain rate was observed at high temperatures (Figure 4.11). This can be ascribed to the different mechanical

properties of the S355 structural steel at elevated temperatures and leads to an increase of the reflected pulse (Figure 4.12). For the sake of completeness, also the strain energy dependence on both strain rates and high temperatures was evaluated as the area under the true stress versus true strain curve, up to determined value of strains (yield, uniform and fracture strain).

An important consideration of the mechanical behaviour of the structural steel S355 was highlighted at 550°C, where a strength increase with respect to tests performed at 400°C was obtained. This is a common occurrence for carbon steels, known as blue brittleness, ascribed to the dynamic strain aging and caused mainly by the interaction of nitrogen atoms with dislocations.

Among the available material models, this research is focused on the empirical model proposed by Johnson-Cook in the eighties [144]. On the one hand this choice depends on the opportunity to perform extensive experimental investigation. As a consequence the experimental data were used to perform an accurate calibration of the material model. On the other hand, the Johnson-Cook material model is widely used to describe the material strength in numerical analysis of dynamic events, this because it is already implemented in numerous commercial codes.

On the basis of the experimental data the five Johnson-Cook constitutive parameters were evaluated and their ability in fitting the experimental data was represented. However, a critical review of this constitutive law highlighted a perceptible variation of the thermal softening parameter, ranging from $m \approx 0.45 \div 1.00$. This parameter, evaluated at high strain rates, is strongly influenced by the temperature (Figure 5.5). This leads to the conclusion that if a coupled effect of temperature and dynamic loading would be evaluated, the effect of the extreme variation of the thermal softening can not be neglected. Moreover, the use of a single averaged value of m is a limit and could lead to considerable errors. For these reasons, following a fitting approach, a modification of the dimensionless temperature (T^*) was proposed. This modification, due to its step-by-step definition for increasing temperatures, is also able to take into consideration the blue brittleness effect, experimentally highlighted between 400°C and 550°C.

In the end, starting from an example study, the blast response of a steel column under fire conditions was studied by considering different aspects, such as the buckling length configuration, the temperature, the detonation distance as well as

the blast charge. Moreover, a critical analysis of the implemented Johnson-Cook material model was performed.

The residual load bearing capacity was used to investigate the blast effects of a steel column under fire conditions. The obtained results can be of great interest to establish the initial condition that could potentially lead to the onset of progressive collapse in steel framed structures subjected to a combined effect of fire and blast loadings. On the one hand the column failure due to both hazards lead to the critical conditions for triggering a progressive collapse, on the other hand if the column survives to both hazards, and consequently is able to resist its initial axial load, the column would be able to receive additional loads via redistribution from neighbouring columns which had even more damage. In the example study (S355 unprotected HEB260 section, $L = 3.50$ m) a drastic reduction of the residual load bearing capacity was observed in the first 10 minutes of fire loading. Explosions at stand-off distance between 10 m and 2 m did not produce a high level of damage, with the exception of blasts at very high temperature (900°C).

The blue brittleness phenomenon was highlighted in the numerical simulations. This led to an increase of the residual load bearing capacity between 400°C and 550°C. The same behaviour was obtained experimentally and is the first evidence of the good reliability of the implemented material model. In addition, for the same peak overpressure, an increase of the strain rates was observed at high temperatures. This phenomenon was highlighted also during the analysis of the experimental data and it can be regarded as another evidence of the validity of the implemented material model.

The expected strain rates during blast events were obtained only locally (at mid-height of the column) due to the peak overpressure and impulse and as a consequence of explosions in the close proximity. Blast loads at greater stand-off distances led to local strain rates lower than 10^2 s^{-1}. This is an important consideration because it highlights that high strain rates can be reached during a fire induced progressive collapse triggered by a subsequent blast load, even though this can occur for detonations in the close proximity. It is therefore important to know and have an adequate description of the material the properties in these extreme conditions. In this respect, the ability of a material model to represent the coupled effect of the thermal softening at high strain rates plays a key role. Finally, starting from the definition of the scaled distance, a range of applicability graph was proposed.

7.2 Future developments

The proposed approach was necessary to validate the implemented material model and to present a comprehensive but simplified approach to progressive collapse of steel structures under the coupled effect of fire and blast. The transition to a more complex analysis can be the next step to follow in order to increase the reliability of the numerical model. In spite of that, the advantages of more complex simulations may not be proportional to the increment of the computational time.

However, the transition to a more complex analysis can be the next step to follow to improve the robustness assessment in steel structures focusing the attention to the extreme combined effects of high temperatures and dynamic extreme actions.

7.2.1 From the material point of view

Experimental tests at medium strain rates. In the numerical simulations it has been highlighted that high strain rate ($> 10^2\,s^{-1}$) were obtained only locally due to the blast overpressure and as a consequence of explosions in the close proximity. However, a progressive collapse is a very complex process in which a wide range of strain rates are involved. For that reason, it could be interesting to understand the mechanical properties of the S355 structural steel at high temperatures in the range of moderate strain rates ($10^0 \div 10^2\,s^{-1}$). The Hydro-Pneumatic Machine used in this research should be adopted, but some modifications are required in order to use the EASYHEAT induction water-cooled heating systems.

Experimental tests on other structural steels. Perform tests in a wide range of temperatures and strain rates also on other structural steels, such as the high strength steels (HSS) (S500, S620 and S690) and the very high strength steels (VHSS) (S890 and S960). Thanks to the elevated yield strength offered by the HSS and the VHSS, the main design advantages are the reduction of the profile-web thickness as well as a section reduction. This results in a remarkable weight reduction. These steels, already adopted in the automotive field and for off-shore structures, can be used for example for the design of bridges where the key design benefits include greater load carrying capacity as well as lighter or longer spans [165]. Due to the process adopted in the

production of these steels (quenching and tempering), it can be of fundamental importance to understand the effects of the high strain rates on the mechanical properties at high temperatures.

TEM analysis. With the purpose of better understanding the effect of nitrogen atoms with dislocations, experimentally highlighted at high strain rates from 400°C to 550°C, a transmission electron microscopy (TEM) analysis should be performed. This could be helpful for the study of a physics-based constitutive relationship. Furthermore, performing additional tests in the neighbourhood $400 \div 550$°C could lead to a better identification of the dynamic strain ageing at high strain rates.

7.2.2 From the structural point of view

Improvement of the numerical model. It is a matter of fact that a strain rate sensitive material model is required for the numerical simulation of blast events. However, the high strain rates were obtained only locally. The creation of numerical model (e.g. a column) with different material models can be helpful for the improvement of the computational efficiency.

Performing full scale tests. Due to the costs and the time required, these type of problems are often numerically studied or experimentally studied using reduced scale tests. But, in order to have a better validation of the employed numerical model, some full scale tests can be helpful.

Study other structural components. The proposed material model can be implemented in numerical simulations in order to study other structural components subjected to the coupled effect of fire and blast.

Migrate from local to global analysis. The results obtained in this research can be helpful to establish criteria for understanding the level of damage of single column under fire and blast loadings. The level of damage can be used as a starting condition in pushdown analyses for the assessment of robustness in structures where progressive collapse is triggered by the failure of one or more steel columns.

References

[1] F.M. Mazzolani, M. Byfield, and G. De Matteis. Recent development in blast and impact research in europe. In *Proceedings of the Workshop on Structures under Extreme Loading (PROTECT09)*, National Defense Academy Protect Workshop (2009), 9 2009.

[2] F.M. Mazzolani. Urban Habitat Constructions under Catastrophic Events: The COST C26 Action. In *Performance, Protection and Strengthening of Structures under Extreme Loading*, volume 82 of *Applied Mechanics and Materials*, pages 15–25. Trans Tech Publications, 9 2011. doi: 10.4028/www.scientific.net/AMM.82.15.

[3] E. Cadoni and M. di Prisco, editors. *Performance, Protection and Strengthening of Structures under Extreme Loading (PROTECT2011)*, volume 82 of *Applied Mechanics and Materials*. Trans Tech Publications, 2011.

[4] V. Kodur and N. Banthia, editors. *Response of Structures Under Extreme Loading (PROTECT2015)*. DEStech Publications, 2015.

[5] Queen's Printer and Controller of Her Majesty's Stationery Office, editors. *Review of international research on structural robustness and disproportionate collapse*. Building regulations: research and Building regulation. Department for Communities and Local Government, October 2011.

[6] National Consortium for the Study of Terrorism and Responses to Terrorism (START). Global Terrorism Database, (2016). URL https://www.start.umd.edu/gtd.

[7] B.R. Ellingwood, R. Smilowitz, D.O. Dusenberry, D. Duthinh, H.S. Lew, and N.J. Carino. *Best Practices for Reducing the Potential for Progressive Collapse in Buildings*. National Institute of Standards and Technology (NIST), 2007.

[8] D. Forni, B. Chiaia, and E. Cadoni. Strain rate behaviour in tension of S355 steel: Base for progressive collapse analysis. *Engineering Structures*, 119:164 – 173, 2016. ISSN 0141-0296. doi: http://dx.doi.org/10.1016/j.engstruct.2016.04.013. URL http://www.sciencedirect.com/science/article/pii/S0141029616301249.

[9] D. Forni, B. Chiaia, and E. Cadoni. High strain rate response of S355 at high temperatures. *Materials & Design*, 94:467 – 478, 2016. ISSN 0264-1275. doi: http://dx.doi.org/10.1016/j.matdes.2015.12.160. URL http://www.sciencedirect.com/science/article/pii/S0264127515310200.

[10] *Eurocode 1: Actions on structures. Part 1-7: General actions - Accidental actions*. European Standard, 2006.

[11] *Progressive Collapse Analysis and Design Guidelines for New Federal Office Buildings and Major Modernization Projects*. General Service Administration, 2003.

[12] O.M. Banu. *Structural robustness provisions in modern design codes and regulations*. Buletinul Institutului Politehnic, 2001.

[13] M. Haberland and U. Starossek. *Progressive Collapse Nomenclature*, chapter 209, pages 1886–1895. Structures 2009: Don't Mess with Structural Engineers, 2009. doi: 10.1061/41031(341)209. URL http://ascelibrary.org/doi/abs/10.1061/41031%28341%29209.

[14] J.B. Menzies and D.A. Nethercot. Progressive collapse - Preventive measures in the United Kingdom. 1998.

[15] A. Longinow and B.R. Ellinwood. The impact of the Ronan Point collapse - 25 years after. 1998.

[16] C. Pearson and N. Delatte. Ronan point apartment tower collapse and its effect on building codes. *Journal of Performance of Constructed Facilities*, 19(2):172–177, 2005. doi: 10.1061/(ASCE)0887-3828(2005)19:2(172). URL http://dx.doi.org/10.1061/(ASCE)0887-3828(2005)19:2(172).

[17] *Eurocode - Basis of structural design*. European Standard, 2002.

[18] J. Agarwal and J. England. Recent developments in robustness and relation with risk. *Proceedings of the Institution of Civil Engineers: Structures and Buildings*, 161(4):183–188, 8 2008. ISSN 0965-0911. doi: 10.1680/stbu.2008.161.4.183.

[19] T.D.G. Canisius, J. Sorensen, and J.W. Baker. *Robustness of Structural Systems: A new Focus for the Joint Committee on Structural Safety (JCSS)*. Marcel Dekker Incorporated, United States, 2007.

[20] D. Cuoco. Investigation of L'Ambiance Plaza Building collapse. *Journal of Performance of Constructed Facilities*, 8(2), 1992.

[21] A. Kazemi-Moghaddam and M. Sasani. Progressive collapse evaluation of Murrah federal building following sudden loss of column. *Engineering Structures*, 89(0):162 – 171, 2015. ISSN 0141-0296. doi: http://dx.doi.org/10.1016/j.engstruct.2015.02.003. URL http://www.sciencedirect.com/science/article/pii/S0141029615000772.

[22] Z.P. Bazant and Y. Zhou. Why did the World Trade Center collapse? - Simple analysis. *Journal of Engineering Mechanics ASCE*, 128(1):2–6, JAN 2002. ISSN 0733-9399.

[23] Z.P. Bazant and Mathieu Verdure. Mechanics of progressive collapse: Learning from World Trade Center and building demolitions. *Journal of Engineering Mechanics ASCE*, 133(3):308–319, MAR 2007. ISSN 0733-9399. doi: 10.1061/(ASCE)0733-9399(2007)133:3(308).

[24] V. Karlos and G. Solomos. Calculation of blast loads for application to structural components. Technical Report Administrative Arrangement N°JRC 32253-2011 with DG-HOME Activity A5 - Blast Simulation Technology Development, 2013. URL http://publications.jrc.ec.europa.eu/repository/handle/JRC87200.

[25] W.E. Baker. *Explosions in air*. University of Texas Press, 1973. ISBN 9780292720039. URL https://books.google.it/books?id=iv4oAQAAMAAJ.

[26] G.F. Kinney and K.J. Graham. *Explosions in air, Second Edition*. 1985. URL https://www.scopus.com/inward/record.uri?eid=2-s2.0-0022283792&partnerID=40&md5=54060676ec0e290dc4b87522fc154547.

[27] T. Krauthammer. *Modern Protective Structures*. Taylor & Francis Group, 2008.

[28] D. Cormie, G. Mays, and P. Smith. *Blast Effects on Buildings, 2nd edition*. Thomas Telford Ltd, 2009.

[29] *Structures to Resist the Effects of Accidental Explosions, TM 5-1300*. Department of the Army, Washington, D.C., June 1969.

[30] C.N. Kingery and G. Bulmash. *Air Blast Parameters from TNT Spherical Air Burst and Hemispherical Surface Burst*. Technical report ARBRL. U.S. Army Ballistic Research Laboratories, 1984. URL https://books.google.it/books?id=lg6cHAAACAAJ.

[31] William L. Bounds, editor. *Design of Blast-Resistant Buildings in Petrochemical Facilities: Second Edition*. American Society of Civil Engineers, 2010.

[32] *Blast Protection of Buildings*. American Society of Civil Engineers, ASCE/SEI 59-11 edition, 2011. doi: 10.1061/9780784411889. URL http://ascelibrary.org/doi/abs/10.1061/9780784411889.

[33] Single degree of freedom structural response limits for antiterrorism design. Technical Report PDC-TR 06-08, U.S. ARMY Corps of Engineers - Protective Design Center, 2008.

[34] Structures to resist the effects of accidental explosions. Technical Report UFC 3-340-02, Department of Defence - United States of America, 2014.

[35] P.M. Stylianidis, D.A. Nethercot, B.A. Izzuddin, and A.Y. Elghazouli. Study of the mechanics of progressive collapse with simplified beam models. *Engineering Structures*, 117:287–304, 2016. doi: 10.1016/j.engstruct.2016.02.056. URL http://dx.doi.org/10.1016/j.engstruct.2016.02.056.

[36] B.R. Ellingwood and E.V. Leyendecker. Approaches for design against progressive collapse. *Journal of the Structural Division*, 104:413–423, 1978. URL http://cedb.asce.org/CEDBsearch/record.jsp?dockey=0007941.

[37] A. Formisano, R. Landolfo, and F.M. Mazzolani. Robustness assessment approaches for steel framed structures under catastrophic events. *Computers & Structures*, 147:216 – 228, 2015. ISSN 0045-7949. doi: http://dx.doi.org/10.1016/j.compstruc.2014.09.010. URL http://www.sciencedirect.com/science/article/pii/S0045794914002107. CIVIL-COMP.

[38] T.D.G. Canisius. Cost action tu0601 - structural robustness design for practising engineers. Technical report, COST Action TU0601 Robustness of Structures, 2011. URL http://www.cost-tu0601.ethz.ch/Documents/Final%20Report/COST_TU0601_structural_robustness_design_practising_engineers_Version1_2-11Sept11.pdf.

[39] J.W. Baker, M. Schubert, and M.H. Faber. On the assessment of robustness. *Structural Safety*, 30(3):253 – 267, 2008. ISSN 0167-4730. doi: http://dx.doi.org/10.1016/j.strusafe.2006.11.004. URL http://www.sciencedirect.com/science/article/pii/S0167473006000737.

[40] D.M. Frangopol and J.P. Curley. Effects of damage and redundancy on structural reliability. *Journal of Structural Engineering*, 113(7):1533–1549, 1987. doi: 10.1061/(ASCE)0733-9445(1987)113:7(1533).

[41] G. Fu and D.M. Frangopol. Balancing weight, system reliability and redundancy in a multiobjective optimization framework. *Structural Safety*, 7(2):165 – 175, 1990. ISSN 0167-4730. doi: http://dx.doi.org/10.1016/0167-4730(90)90066-X. URL http://www.sciencedirect.com/science/article/pii/016747309090066X.

[42] M.H. Faber, M.A. Maes, D. Straub, and J.W. Baker. On the quantification of robustness of structures. In *Offshore Mechanics and Arctic Engineering*, 2006.

[43] F. Knoll and T. Vogel. *Design for Robustness*, volume 11 of *Structural Engineering Documents*. IABSE, 2009.

[44] P.M. Stylianidis and D.A. Nethercot. Modelling of connection behaviour for progressive collapse analysis. *Journal of Constructional Steel Research*, 113:169 – 184, 2015. ISSN 0143-974X. doi: http://dx.doi.org/10.1016/j.jcsr.2015.06.008. URL http://www.sciencedirect.com/science/article/pii/S0143974X15300134.

[45] P.M. Stylianidis, D.A. Nethercot, B.A. Izzuddin, and A.Y. Elghazouli. Modelling of beam response for progressive collapse analysis. *Structures*, 3: 137 – 152, 2015. ISSN 2352-0124. doi: http://dx.doi.org/10.1016/j.istruc.2015.04.001. URL http://www.sciencedirect.com/science/article/pii/S235201241500048X.

[46] A.G. Vlassis, B.A. Izzuddin, A.Y. Elghazouli, and D.A. Nethercot. Progressive collapse of multi-storey buildings due to sudden column loss - Part II: Application. *ENGINEERING STRUCTURES*, 30:1424–1438, 2008. doi: 10.1016/j.engstruct.2007.08.011. URL http://dx.doi.org/10.1016/j.engstruct.2007.08.011.

[47] B.A. Izzuddin, A.G. Vlassis, A.Y. Elghazouli, and D.A. Nethercot. Progressive collapse of multi-storey buildings due to sudden column loss - part I: Simplified assessment framework. *Engineering Structures*, 30(5):1308 – 1318, 2008. ISSN 0141-0296. doi: http://dx.doi.org/10.1016/j.engstruct.2007.07.011. URL http://www.sciencedirect.com/science/article/pii/S0141029607002805.

[48] S. Szyniszewski and T. Krauthammer. Energy flow in progressive collapse of steel framed buildings. *Engineering Structures*, 42(0):142 – 153, 2012. ISSN 0141-0296. doi: http://dx.doi.org/10.1016/j.engstruct.2012.04.014. URL http://www.sciencedirect.com/science/article/pii/S0141029612002003.

[49] S. Szyniszewski. *Energy flow based progressive collapse studies of moment resisting steel framed buildingsEnergy flow based progressive collapse studies of moment resisting steel framed buildings*. PhD thesis, University of Florida, 2009.

[50] S. Szyniszewski. Dynamic energy based method for progressive collapse analysis. *Structures Congress*, pages 1–10, 2009.

[51] H.S. Lew, J.A. Main, S.D. Robert, F. Sadek, and V.P. Chiarito. Performance of steel moment connections under a column removal scenario. I: Experiments. *Journal of Structural Engineering*, 139(1):98–107, 2013. doi: 10.1061/(ASCE)ST.1943-541X.0000618. URL http://dx.doi.org/10.1061/(ASCE)ST.1943-541X.0000618.

[52] F. Sadek, J.A. Main, H.S. Lew, and S. El-Tawil. Performance of steel moment connections under a column removal scenario. II: Analysis. *Journal of Structural Engineering*, 139(1):108–119, 2013. doi: 10.1061/(ASCE)ST.1943-541X.0000617. URL http://dx.doi.org/10.1061/(ASCE)ST.1943-541X.0000617.

[53] R. Liu, B. Davison, and A. Tyas. A study of progressive collapse in multi-storey steel frames. In *Structures Congress 2005*, pages 1–9. American Society of Civil Engineers, 2005. doi: 10.1061/40753(171)218. URL http://ascelibrary.org/doi/abs/10.1061/40753%28171%29218.

[54] P.M. Stylianidis, D.A. Nethercot, B.A. Izzuddin, and A.Y. Elghazouli. Robustness assessment of frame structures using simplified beam and grillage models. *Engineering Structures*, 115:78 – 95, 2016. ISSN 0141-0296. doi: http://dx.doi.org/10.1016/j.engstruct.2016.02.003. URL http://www.sciencedirect.com/science/article/pii/S0141029616000857.

[55] L. Kwasniewski. Nonlinear dynamic simulations of progressive collapse for a multistory building. *Engineering Structures*, 32(5):1223 – 1235, 2010. ISSN 0141-0296. doi: http://dx.doi.org/10.1016/j.engstruct.2009.12.048. URL http://www.sciencedirect.com/science/article/pii/S0141029609004428.

[56] D.E. Grierson, L. Xu, and Y. Liu. Progressive-failure analysis of buildings subjected to abnormal loading. *Computer-Aided Civil and Infrastructure Engineering*, 20(3):155–171, 2005. ISSN 1467-8667. doi: 10.1111/j.1467-8667.2005.00384.x. URL http://dx.doi.org/10.1111/j.1467-8667.2005.00384.x.

[57] G. Kaewkulchai and E.B. Williamson. Beam element formulation and solution procedure for dynamic progressive collapse analysis. *Computers & Structures*, 82(7–8):639 – 651, 2004. ISSN 0045-7949. doi: http://dx.doi.org/10.1016/j.compstruc.2003.12.001. URL http://www.sciencedirect.com/science/article/pii/S0045794904000045.

[58] J.Y.Richard Liew, L.K. Tang, Tore Holmaas, and Y.S. Choo. Advanced analysis for the assessment of steel frames in fire. *Journal of Constructional Steel Research*, 47(1–2):19 – 45, 1998. ISSN 0143-974X. doi: http://dx.doi.org/10.1016/S0143-974X(98)80004-7. URL http://www.sciencedirect.com/science/article/pii/S0143974X98800047.

[59] C. Fang, B.A. Izzuddin, A.Y. Elghazouli, and D.A. Nethercot. Robustness of steel-composite building structures subject to localised fire. *Fire Safety Journal*, 46(6):348 – 363, 2011. ISSN 0379-7112. doi: http://dx.doi.org/10.1016/j.firesaf.2011.06.001. URL http://www.sciencedirect.com/science/article/pii/S0379711211000804.

[60] C. Fang, B.A. Izzuddin, A.Y. Elghazouli, and D.A. Nethercot. Simplified energy-based robustness assessment for steel-composite car parks under vehicle fire. *Engineering Structures*, 49:719 – 732, 2013. ISSN 0141-0296. doi: http://dx.doi.org/10.1016/j.engstruct.2012.12.036. URL http://www.sciencedirect.com/science/article/pii/S0141029613000060.

[61] R. Sun, Z. Huang, and I.W. Burgess. Progressive collapse analysis of steel structures under fire conditions. *Engineering Structures*, 34:400 – 413, 2012. ISSN 0141-0296. doi: http://dx.doi.org/10.1016/j.engstruct.2011.10.009. URL http://www.sciencedirect.com/science/article/pii/S0141029611004068.

[62] M. Kucz, K. Rzeszut, P. Łukasz, and M. Malendowski. Influence of boundary conditions on the thermal response of selected steel members. *Procedia Engineering*, 57:977 – 985, 2013. ISSN 1877-7058. doi: http://dx.doi.org/10.1016/j.proeng.2013.04.124. URL http://www.sciencedirect.com/science/

article/pii/S1877705813008576. Modern Building Materials, Structures and Techniques.

[63] G.F. Porcari, E. Zalok, and W. Mekky. Fire induced progressive collapse of steel building structures: A review of the mechanisms. *Engineering Structures*, 82:261 – 267, 2015. ISSN 0141-0296. doi: http://dx.doi.org/10.1016/j.engstruct.2014.09.011. URL http://www.sciencedirect.com/science/article/pii/S0141029614005471.

[64] B. Jiang, G.Q. Li, and A. Usmani. Progressive collapse mechanisms investigation of planar steel moment frames under localized fire. *Journal of Constructional Steel Research*, 115:160 – 168, 2015. ISSN 0143-974X. doi: http://dx.doi.org/10.1016/j.jcsr.2015.08.015. URL http://www.sciencedirect.com/science/article/pii/S0143974X15300626.

[65] B.A. Izzuddin and Q. Fang. Rate-sensitive analysis of framed structures part i: model formulation and verification. *Structural Engineering and Mechanics*, 5:221–237, 1997. doi: 10.12989/sem.1997.5.3.221.

[66] B.A Izzuddin, L Song, A.S Elnashai, and P.J Dowling. An integrated adaptive environment for fire and explosion analysis of steel frames - Part II: verification and application. *Journal of Constructional Steel Research*, 53 (1):87 – 111, 2000. ISSN 0143-974X. doi: http://dx.doi.org/10.1016/S0143-974X(99)00041-3. URL http://www.sciencedirect.com/science/article/pii/S0143974X99000413.

[67] H. Chen and J.Y. Liew. Explosion and fire analysis of steel frames using mixed element approach. *Journal of Engineering Mechanics*, 131(6):606–616, 2005. doi: 10.1061/(ASCE)0733-9399(2005)131:6(606). URL http://dx.doi.org/10.1061/(ASCE)0733-9399(2005)131:6(606).

[68] J.Y. Richard Liew. Survivability of steel frame structures subject to blast and fire. *Journal of Constructional Steel Research*, 64(7–8):854 – 866, 2008. ISSN 0143-974X. doi: http://dx.doi.org/10.1016/j.jcsr.2007.12.013. URL http://www.sciencedirect.com/science/article/pii/S0143974X07001976. <ce:title>International Colloquium on Stability and Ductility of Steel Structures 2006</ce:title>.

[69] TM5-1300. Structures to resist the effects of accidental explosions, US army manual. 1990.

[70] *Eurocode 3 - Design of steel structures. Part 1-2: General rules - Structural fire design*. European Standard, 2005.

[71] L. Song, B.A. Izzuddin, A.S. Elnashai, and P.J. Dowling. An integrated adaptive environment for fire and explosion analysis of steel frames - Part I: Analytical models. *Journal of Constructional Steel Research*, 53(1):63 – 85, 2000. ISSN 0143-974X. doi: http://dx.doi.org/10.1016/S0143-974X(99)00040-1. URL http://www.sciencedirect.com/science/article/pii/S0143974X99000401.

[72] Y. Ding, M. Wang, Z. Li, and H. Hao. Damage evaluation of the steel tubular column subjected to explosion and post-explosion fire condition. *Engineering Structures*, 55:44 – 55, 2013. ISSN 0141-0296. doi: http://dx.doi.org/10.1016/j.engstruct.2012.01.013. URL http://www.sciencedirect.com/science/article/pii/S0141029612000351. Analysis and Design of Protective Structures.

[73] M.S. Seif, J.A. Main, and F. Sadek. Behavior of structural steel moment connections under fire loading. In *Annual Stability Conference Structural Stability Research Council*, 2015.

[74] S. Marjanishvili and E. Agnew. Comparison of various procedures for progressive collapse analysis. *JOURNAL OF PERFORMANCE OF CONSTRUCTED FACILITIES*, 20(4):365–374, NOV 2006. ISSN 0887-3828. doi: 10.1061/(ASCE)0887-3828(2006)20:4(365).

[75] F. Fu. Progressive collapse analysis of high-rise building with 3-D finite element modeling method. *JOURNAL OF CONSTRUCTIONAL STEEL RESEARCH*, 65(6):1269–1278, JUN 2009. ISSN 0143-974X. doi: 10.1016/j.jcsr.2009.02.001.

[76] *Progressive Collapse: Case studies Using Nonlinear Analysis*, 2005. Structures Congress 2005. doi: 10.1061/40753(171)216. URL http://dx.doi.org/10.1061/40753(171)216.

[77] S. Kokot, A. Anthoine, P. Negro, and G. Solomos. Static and dynamic analysis of a reinforced concrete flat slab frame building for progressive collapse. *Engineering Structures*, 40:205 – 217, 2012. ISSN 0141-0296. doi: http://dx.doi.org/10.1016/j.engstruct.2012.02.026. URL http://www.sciencedirect.com/science/article/pii/S014102961200096X.

[78] E. Masoero, F.K. Wittel, H.J. Herrmann, and B.M. Chiaia. Progressive collapse mechanisms of brittle and ductile framed structures. *Journal of Engineering Mechanics*, 136(8):987–995, 2010. doi: 10.1061/(ASCE)EM.1943-7889.0000143. URL http://www.scopus.com/inward/record.url?eid=2-s2.0-77955648379&partnerID=40&md5=6d92b61ced02628e72c131cd274374ee.

[79] E. Masoero, F.K. Wittel, H.J. Herrmann, and B.M. Chiaia. Hierarchical structures for a robustness-oriented capacity design. *Journal of Engineering Mechanics*, 138(11):1339–1347, 2012. doi: 10.1061/(ASCE)EM.1943-7889.0000437. URL http://www.scopus.com/inward/record.url?eid=2-s2.0-84877794788&partnerID=40&md5=4aa56980e7e3f4f7fd058850e34a8bbe.

[80] E. Masoero, P. Darò, and B.M. Chiaia. Progressive collapse of 2D framed structures: An analytical model. *Engineering Structures*, 54:94–102, 2013. doi: 10.1016/j.engstruct.2013.03.053. URL http://www.scopus.com/inward/record.url?eid=2-s2.0-84877815639&partnerID=40&md5=0bf535638927293b5bc4fda17396a428.

[81] J.Y. Richard Liew and Hong Chen. Explosion and fire analysis of steel frames using fiber element approach. *Journal of Structural Engineering*, 130(7): 991–1000, 2004. doi: 10.1061/(ASCE)0733-9445(2004)130:7(991). URL http://dx.doi.org/10.1061/(ASCE)0733-9445(2004)130:7(991).

[82] F. Xi, Q.M. Li, and Y.H. Tan. Dynamic response and critical temperature of a steel beam subjected to fire and subsequent impulsive loading. *Computers & Structures*, 135:100 – 108, 2014. ISSN 0045-7949. doi: http://dx.doi.org/10.1016/j.compstruc.2014.01.014. URL http://www.sciencedirect.com/science/article/pii/S004579491400025X.

[83] F. Xi. Large deflection response of restrained steel beams under fire and explosion loads. *SpringerPlus*, 5(1):752, 2016. ISSN 2193-1801. doi: 10.1186/s40064-016-2509-6. URL http://dx.doi.org/10.1186/s40064-016-2509-6.

[84] T. Ngo, P. Mendis, A. Gupta, and J. Ramsay. Blast loading and blast effects on structures – an overview. *Electronic Journal of Structural Engineering*, 7: 76–91, 2007.

[85] J.C. Yang, M. Bundy, J. Gross, A. Hamins, F. Sadek, and A. Raghunathan. International r&d roadmap for fire resistance of structures summary of nist/cib workshop. Technical report, NIST, March 2015. URL http://dx.doi.org/10.6028/NIST.SP.1188.

[86] D. Asprone, E. Cadoni, and A. Prota. Tensile high strain-rate behavior of reinforcing steel from an existing bridge. *ACI Structural Journal*, 106(4):523–529, 2009. URL https://www.scopus.com/inward/record.uri?eid=2-s2.0-70449381393&partnerID=40&md5=654dc9090e4b77ca8a9e901f039c44bb.

[87] H. Petroski. *To Forgive Design: Understanding Failure*. Harvard University Press, 2012. ISBN 9780674065840. URL http://www.jstor.org/stable/j.ctt2jbqv9.

[88] F. Hamdan. Design guide for steel at elevated temperature and high strain rate. Technical report, FABIG - The steel construction institute, 2001.

[89] N.K. Singh, E. Cadoni, M.K. Singha, and N.K. Gupta. Dynamic tensile and compressive behaviors of mild steel at wide range of strain rates. *Journal of Engineering Mechanics*, 139(9):1197–1206, 2013. doi: 10.1061/(ASCE)EM.1943-7889.0000557. URL http://dx.doi.org/10.1061/(ASCE)EM.1943-7889.0000557.

[90] J. Outinen, J. Kesti, and P. Mäkeläinen. Fire design model for structural steel s355 based upon transient state tensile test results. *Journal of Constructional Steel Research*, 42(3):161 – 169, 1997. ISSN 0143-974X. doi: http://dx.doi.org/10.1016/S0143-974X(97)00018-7. URL http://www.sciencedirect.com/science/article/pii/S0143974X97000187.

[91] J. Outinen and P. Makelainen. Mechanical properties of structural steel at elevated temperatures and after cooling down. *Second International Workshop «Structures in Fire»*, 2002.

[92] J.B. Yan, J.Y.R. Liew, M.H. Zhang, and J.Y. Wang. Mechanical properties of normal strength mild steel and high strength steel {S690} in low temperature relevant to arctic environment. *Materials & Design*, 61(0):150 – 159, 2014. ISSN 0261-3069. doi: http://dx.doi.org/10.1016/j.matdes.2014.04.057. URL http://www.sciencedirect.com/science/article/pii/S026130691400332X.

[93] J. Chen, B. Young, M. ASCE, B Uy, and M ASCE. Behavior of high strength structural steel at elevated temperatures. *JOURNAL OF STRUCTURAL ENGINEERING*, 2006.

[94] British Standard Institution BSI (1998). Structural use of steelwork in building - Part 8: Code of practice for fire resistant design." BS 5950-8:1990, London. 2005.

[95] A. Heidarpour, N.S. Tofts, A.H. Korayem, X. Zhao, and C.R. Hutchinson. Mechanical properties of very high strength steel at elevated temperatures. *Fire Safety Journal*, 64:27 – 35, 2014. ISSN 0379-7112. doi: http://dx.doi.org/10.1016/j.firesaf.2014.01.006. URL http://www.sciencedirect.com/science/article/pii/S0379711214000174.

[96] X. Qiang, F.S.K. Bijlaard, and H. Kolstein. Post-fire mechanical properties of high strength structural steels S460 and S690. *Engineering Structures*, 35:1 – 10, 2012. ISSN 0141-0296. doi: http://dx.doi.org/10.1016/j.engstruct.2011.11.005. URL http://www.sciencedirect.com/science/article/pii/S0141029611004433.

[97] X. Qiang, F.S.K. Bijlaard, and H. Kolstein. Post-fire performance of very high strength steel S960. *Journal of Constructional Steel Research*, 80:235 – 242, 2013. ISSN 0143-974X. doi: http://dx.doi.org/10.1016/j.jcsr.2012.09.002. URL http://www.sciencedirect.com/science/article/pii/S0143974X1200209X.

[98] X. Qiang, F. Bijlaard, and H. Kolstein. Dependence of mechanical properties of high strength steel S690 on elevated temperatures. *Construction and Building Materials*, 30:73 – 79, 2012. ISSN 0950-0618. doi: http://dx.doi.org/10.1016/j.conbuildmat.2011.12.018. URL http://www.sciencedirect.com/science/article/pii/S0950061811006957.

[99] American Institute of Steel Construction (AISC). Specification for Structural steel buildings – an American national standard. 2010.

[100] M. Mirmomeni, A. Heidarpour, X. Zhao, C.R. Hutchinson, J.A. Packer, and C. Wu. Mechanical properties of partially damaged structural steel induced by high strain rate loading at elevated temperatures – an experimental investigation. *International Journal of Impact Engineering*, 76:178 – 188, 2015. ISSN 0734-743X. doi: http://dx.doi.org/10.1016/j.ijimpeng.2014.10.001. URL http://www.sciencedirect.com/science/article/pii/S0734743X14002334.

[101] M. Mirmomeni, A. Heidarpour, X. Zhao, C.R. Hutchinson, J.A. Packer, and C. Wu. Fracture behaviour and microstructural evolution of structural mild steel under the multi-hazard loading of high-strain-rate load followed by elevated temperature. *Construction and Building Materials*, 122:760 – 771, 2016. ISSN 0950-0618. doi: http://dx.doi.org/10.1016/j.conbuildmat.2016.06.122. URL http://www.sciencedirect.com/science/article/pii/S0950061816310601.

[102] A. Krabiell and W. Dahl. Influence of strain rate and temperature on the tensile and fracture properties of structural steels. *Fracture Toughness under dynamic loading*, 1981.

[103] M. Knobloch, J. Pauli, and M. Fontana. Influence of the strain-rate on the mechanical properties of mild carbon steel at elevated temperatures. *Materials & Design*, 49:553 – 565, 2013. ISSN 0261-3069. doi: http://dx.doi.org/10.1016/j.matdes.2013.01.021. URL http://www.sciencedirect.com/science/article/pii/S0261306913000356.

[104] T. Børvik, O.S. Hopperstad, S. Dey, E.V. Pizzinato, M. Langseth, and C. Albertini. Strength and ductility of weldox 460 e steel at high strain rates, elevated temperatures and various stress triaxialities. *Engineering Fracture Mechanics*, 72(7):1071 – 1087, 2005. ISSN 0013-7944. doi: http://dx.doi.org/10.1016/j.engfracmech.2004.07.007. URL http://www.sciencedirect.com/science/article/pii/S0013794404001614.

[105] W. Moćko and L. Kruszka. Results of strain rate and temperature on mechanical properties of selected structural steels. *Procedia Engineering*, 57:789 – 797, 2013. ISSN 1877-7058. doi: http://dx.doi.org/10.1016/j.proeng.2013.04.100. URL http://www.sciencedirect.com/science/article/pii/S1877705813008333.

[106] G. Solomos, C. Albertini, K. Labibes, V. Pizzinato, and B. Viaccoz. Strain rate effects in nuclear steels at room and higher temperatures. *Nuclear Engineering and Design*, 229(2–3):139 – 149, 2004. ISSN 0029-5493. doi: http://dx.doi.org/10.1016/j.nucengdes.2003.10.006. URL http://www.sciencedirect.com/science/article/pii/S0029549303003650.

[107] W. Luecke, S.W. Banovic, and J.D. McColskey. High-temperature tensile constitutive data and models for structural steels in fire. Technical report, NIST, 2011. URL https://dx.doi.org/10.6028/NIST.TN.1714.

[108] S. Walley and D. Eakins. Introduction. *Philosophical Transactions of the Royal Society of London A: Mathematical, Physical and Engineering Sciences*, 372(2015), 2014. ISSN 1364-503X. doi: 10.1098/rsta.2013.0220. URL http://rsta.royalsocietypublishing.org/content/372/2015/20130220.

[109] J.E. Field, S.M. Walley, N. Bourne, and J. Huntley. Experimental methods at high rates of strain. *Journal de Physique IV*, 04(C8):C8–3–C8–22, 1994. doi: 10.1051/jp4:1994801. URL https://hal.archives-ouvertes.fr/jpa-00253331.

[110] J.E. Field, S.M. Walley, W.G. Proud, H.T. Goldrein, and C.R. Siviour. Review of experimental techniques for high rate deformation and shock studies. *International Journal of Impact Engineering*, 30(7):725 – 775, 2004. ISSN 0734-743X. doi: http://dx.doi.org/10.1016/j.ijimpeng.2004.03.005. URL http://www.sciencedirect.com/science/article/pii/S0734743X04000521. Fifth International Symposium on Impact Engineering.

[111] G.T. Gray. Classic Split-Hopkinson pressure bar testing. *ASM Handbook*, 8: 462–476, 2000.

[112] B.A. Gama, S.L. Lopatnikov, and J.W. Gillespie (Jr). Hopkinson bar experimental technique: A critical review. *Applied Mechanics Reviews*, 57:223–250, 2004. doi: http://dx.doi.org/10.1115/1.1704626.

[113] W. Chen and B. Song. *Split Hopkinson (Kolsky) bar: Design, Testing and Applications*. Springer, New York, 2011.

[114] EN10025:2 (2005) - Hot rolled products of structural steels. 2005.

[115] E. Cadoni, M. Dotta, D. Forni, and P. Spaetig. Strain-rate behavior in tension of the tempered martensitic reduced activation steel Eurofer97. *Journal of Nuclear Materials*, 414(3):360 – 366, 2011. ISSN 0022-3115. doi: 10.1016/j.jnucmat.2011.05.002. URL http://www.sciencedirect.com/science/article/pii/S0022311511004338.

[116] E. Cadoni, M. Dotta, D. Forni, N. Tesio, and C. Albertini. Mechanical behaviour of quenched and self-tempered reinforcing steel in tension under high strain rate. *Materials & Design*, 49(0):657 – 666, 2013. ISSN 0261-3069. doi: 10.1016/j.matdes.2013.02.008. URL http://www.sciencedirect.com/science/article/pii/S0261306913001040.

[117] H. Kolsky. An investigation of the mechanical properties of materials at very high rates of loading. *Proceedings of the Physical Society. Section B*, 62(11): 676, 1949. URL http://stacks.iop.org/0370-1301/62/i=11/a=302.

[118] B. Hopkinson. A method of measuring the pressure produced in the detonation of high explosives or by the impact of bullets. *Philosophical Transactions of the Royal Society of London A: Mathematical, Physical and Engineering Sciences*, 213(497-508):437–456, 1914. ISSN 0264-3952. doi: 10.1098/rsta.1914.0010.

[119] E. Volterra. Alcuni risultati di prove dinamiche sui materiali. *La Rivista del Nuovo Cimento*, 4:1–28, 1948.

[120] G.I. Taylor. The testing of materials at high rates of loadings. *Journal of the Institution of Civil Engineers*, 26(8):486–519, 1946. doi: 10.1680/ijoti.1946.13699.

[121] R.M. Davies. A critical study of the hopkinson pressure bar. *Philosophical Transactions of the Royal Society of London A: Mathematical, Physical and Engineering Sciences*, 240(821):375–457, 1948. ISSN 0080-4614. doi: 10.1098/rsta.1948.0001.

[122] J.M. Krafft, A.M. Sullivan, and C.F. Tipper. The effect of static and dynamic loading and temperature on the yield stress of iron and mild steel in compression. *Proceedings of the Royal Society of London A: Mathematical, Physical and Engineering Sciences*, 221(1144):114–127, 1954. ISSN 0080-4630. doi: 10.1098/rspa.1954.0009. URL http://rspa.royalsocietypublishing.org/content/221/1144/114.

[123] U.S. Lindholm. Some experiments with the split hopkinson pressure bar. *Journal of the Mechanics and Physics of Solids*, 12(5):317 – 335, 1964. ISSN 0022-5096. doi: http://dx.doi.org/10.1016/0022-5096(64)90028-6. URL http://www.sciencedirect.com/science/article/pii/0022509664900286.

[124] C. Albertini and M. Montagnani. Testing techniques based on the SHPB. In *Institute of Physics Conference series*, volume 21, pages 22–32, 1974.

[125] C. Albertini and M. Montagnani. Dynamic material properties of several steels for fast breeder reactor safety analysis. Technical Report EUR 5787 EN, Joint Research Centre Ispra Establishment — Italy Applied Mechanics Division, 1977.

[126] C. Albertini and M. Montagnani. Constitutive laws of materials in dynamics—outline of a programme of testing on small and large specimens for containment of extreme dynamic loading conditions. *Nuclear Engineering and Design*, 68(2):115 – 128, 1982. ISSN 0029-5493. doi: http://dx.doi.org/10.1016/0029-5493(82)90025-5. URL http://www.sciencedirect.com/science/article/pii/0029549382900255.

[127] C. Albertini. Material properties for reactor pressure vessels and containment shells under dynamic loading. *Nuclear Engineering and Design*, 174 (2):135 – 141, 1997. ISSN 0029-5493. doi: http://dx.doi.org/10.1016/S0029-5493(97)00077-0. URL http://www.sciencedirect.com/science/article/pii/S0029549397000770.

[128] M. Quik, K. Labibes, C. Albertini, T. Valentin, and P. Magain. Dynamic mechanical properties of automotive thin sheet steel in tension, compression and shear. *J. Phys. IV France*, 07:C3–379–C3–384, 1997. doi: 10.1051/jp4:1997366. URL http://dx.doi.org/10.1051/jp4:1997366.

[129] R. Kapoor and S. Nemat-Nasser. Determination of temperature rise during high strain rate deformation. *Mechanics of Materials*, 27(1):1 – 12, 1998. ISSN 0167-6636. doi: http://dx.doi.org/10.1016/S0167-6636(97)00036-7. URL http://www.sciencedirect.com/science/article/pii/S0167663697000367.

[130] J. Perez-Castellanos. Temperature increase associated with plastic deformation under dynamic compression: application to aluminum alloy AL-6082. *Journal of theoretical and applied mechanics*, 50(2):377–398, 2012.

[131] P.W. Bridgman. *Studies in large plastic flow and fracture*. McGraw-Hill, 1952.

[132] J.M. Fransen and P. Vila Real. *Fire Design of Steel Structures 2nd Edition*. ECCS - European Cnvention for Constructional Steelwork, 2015.

[133] F.R.N. Nabarro. Mechanical effects of carbon in iron. *Royal Society Warren Research Fellow*, 1948. URL http://hdl.handle.net/10539/1194.

[134] J. Su, W. Guo, W. Meng, and J. Wang. Plastic behavior and constitutive relations of DH-36 steel over a wide spectrum of strain rates and temperatures under tension. *Mechanics of Materials*, 65:76 – 87, 2013. ISSN 0167-6636. doi: http://dx.doi.org/10.1016/j.mechmat.2013.06.002. URL http://www.sciencedirect.com/science/article/pii/S0167663613001075.

[135] S. Nemat-Nasser and W. Guo. Flow stress of commercially pure niobium over a broad range of temperatures and strain rates. *Materials Science and Engineering: A*, 284(1–2):202 – 210, 2000. ISSN 0921-5093. doi: http://dx.doi.org/10.1016/S0921-5093(00)00740-1. URL http://www.sciencedirect.com/science/article/pii/S0921509300007401.

[136] W.G. Guo. Dynamic strain aging during the plastic flow of metals. *Engineering Plasticity and Its Applications*, pages 823–828, 2007. doi: 10.4028/www.scientific.net/KEM.340-341.823.

[137] C. Albertini, E. Cadoni, and G. Solomos. Advances in the hopkinson bar testing of irradiated/non-irradiated nuclear materials and large specimens. *Philosophical Transactions of the Royal Society A: Mathematical, Physical and Engineering Sciences*, 372(2015), 2014. doi: 10.1098/rsta.2013.0197. URL http://www.scopus.com/inward/record.url?eid=2-s2.0-84898952892&partnerID=40&md5=2c52ec605764c70af74f3d20eb279c40.

[138] B. Banerjee. An evaluation of plastic flow stress models for the simulation of high-temperature and high-strain-rate deformation of metals. *eprint arXiv:cond-mat/0512466*, December 2005.

[139] F.J. Zerilli and R.W. Armstrong. Dislocation mechanics based constitutive relations for material dynamics calculations. *Journal of Applied Physics*, 61 (5):1816–1825, 1987. doi: http://dx.doi.org/10.1063/1.338024. URL http://scitation.aip.org/content/aip/journal/jap/61/5/10.1063/1.338024.

[140] P.S. Follansbee and U.F. Kocks. A constitutive description of the deformation of copper based on the use of the mechanical threshold stress as an internal state variable. *Acta Metallurgica*, 36(1):81–93, 1988. doi: 10.1016/0001-6160(88)90030-2.

URL http://www.scopus.com/inward/record.url?eid=2-s2.0-0023862814&partnerID=40&md5=47070cd11dd7f27367cdc2bd7e6e8455.

[141] D.L. Preston, D.L. Tonks, and D.C. Wallace. Model of plastic deformation for extreme loading conditions. *Journal of Applied Physics*, 93(1):211–220, 2003. doi: 10.1063/1.1524706. URL http://www.scopus.com/inward/record.url?eid=2-s2.0-0037245893&partnerID=40&md5=a6fe70a316c6f63edfc6fe5fedc4a487.

[142] D.J. Steinberg, S.G. Cochran, and M.W. Guinan. A constitutive model for metals applicable at high-strain rate. *Journal of Applied Physics*, 51(3):1498–1504, 1980. doi: 10.1063/1.327799. URL http://www.scopus.com/inward/record.url?eid=2-s2.0-0018986762&partnerID=40&md5=4da2b49e429ef4a6446d831903e13332.

[143] D. J. Steinberg and C. M. Lund. A constitutive model for strain rates from 0.0001 to 1000000 1/s. *Journal of Applied Physics*, 65(4):1528–1533, 1989. doi: http://dx.doi.org/10.1063/1.342968. URL http://scitation.aip.org/content/aip/journal/jap/65/4/10.1063/1.342968.

[144] G.R. Johnson and W.H. Cook. Fracture characteristics of three metals subjected to various strains, strain rates, temperatures and pressures. *Engineering Fracture Mechanics*, 21(1):31–48, 1985. doi: 10.1016/0013-7944(85)90052-9. URL http://www.scopus.com/inward/record.url?eid=2-s2.0-0021787534&partnerID=40&md5=fd5ca23d9196eaf6c95c12c34d9d796c.

[145] J.D. Seidt and A. Gilat. Plastic deformation of 2024-t351 aluminum plate over a wide range of loading conditions. *International Journal of Solids and Structures*, 50(10):1781 – 1790, 2013. ISSN 0020-7683. doi: http://dx.doi.org/10.1016/j.ijsolstr.2013.02.006. URL http://www.sciencedirect.com/science/article/pii/S0020768313000711.

[146] H.M. Elsanadedy, T.H. Almusallam, Y.R. Alharbi, Y.A. Al-Salloum, and H. Abbas. Progressive collapse potential of a typical steel building due to blast attacks. *Journal of Constructional Steel Research*, 101(0):143 – 157, 2014. ISSN 0143-974X. doi: http://dx.doi.org/10.1016/j.jcsr.2014.05.005. URL http://www.sciencedirect.com/science/article/pii/S0143974X14001400.

[147] L. Gambirasio and E. Rizzi. An enhanced johnson–cook strength model for splitting strain rate and temperature effects on lower yield stress and plastic flow. *Computational Materials Science*, 113:231 – 265, 2016. ISSN 0927-0256. doi: http://dx.doi.org/10.1016/j.commatsci.2015.11.034. URL http://www.sciencedirect.com/science/article/pii/S0927025615007417.

[148] N. Kotkunde, A.D. Deole, A.K. Gupta, and S.K. Singh. Comparative study of constitutive modeling for ti–6al–4v alloy at low strain rates and elevated temperatures. *Materials & Design*, 55:999 – 1005, 2014. ISSN 0261-3069. doi: http://dx.doi.org/10.1016/j.matdes.2013.10.089. URL http://www.sciencedirect.com/science/article/pii/S0261306913010327.

[149] G.R. Cowper and P.S. Symonds. *Strain-hardening and strain-rate effects in the impact loading of cantilever beams*. Division of Applied Mathematics, Brown University, 1957.

[150] G. Riganti and E. Cadoni. Numerical simulation of the high strain-rate behavior of quenched and self-tempered reinforcing steel in tension. *Materials and Design*, 57:156–167, 2014. doi: 10.1016/j.matdes.2013.12.049. URL http://www.scopus.com/inward/record.url?eid=2-s2.0-84892184661&partnerID=40&md5=06f63cf072cc9ef6fb40f6d4b1689143.

[151] A. Dorogoy and D. Rittel. Determination of the johnson-cook material parameters using the scs specimen. *Experimental Mechanics*, 49(6):881–885, 2009. doi: 10.1007/s11340-008-9201-x. URL https://www.scopus.com/inward/record.uri?eid=2-s2.0-71449098058&partnerID=40&md5=11bc1b90373c8280909cbc6dd8593e9e.

[152] D. Forni, B. Chiaia, and E. Cadoni. Blast effects on steel columns under fire conditions. *Journal of Constructional Steel Research*, 2017. doi: 10.1016/j.jcsr.2017.04.012.

[153] Y. Han and H. Liu. Finite element simulation of medium-range blast loading using LS-DYNA. *Shock and Vibration*, vol. 2015, Article ID 631493, 9 pages, 2015. doi: 10.1155/2015/631493.

[154] *LS-DYNA Keyword User's Manual, Vol. II Material Models. LS-DYNA R7.1.1. Livermore Software Technology Corporation*.

[155] P. Vila Real, C. Couto, and N. Lopes. Tables for section factors of unprotected and protected steel profiles. Technical Report T09027, LERF, University of Aveiro, 2009.

[156] *ISO 834 Fire Resistance Tests – Elements of building construction*. International Organization for Standardization, 2002.

[157] B.M. Luccioni and D. Ambrosini. Numerical assessment of blast effects scaling procedures. *Mecánica Computacional*, vol. XXIX:1161–1179, 2010.

[158] U.S.ARMY. *TM 5-855-1 Design and analysis of hardened structures to conventional weapons effects*, November 1986.

[159] J. Pauli, D. Somaini, M. Knobloch, and M. Fontana. Experiments on steel columns under fire conditions. Technical report, Institute of Structural Engineering - Swiss Federal Institute of Technology, Zurich, October 2012.

[160] L.K. Steward. *Testing and analysis of structural steel columns subjected to blast loads*. PhD thesis, UC San Diego, 2010.

[161] J.M. Chambers, W.S. Cleveland, B. Kleiner, and P.A. Tukey. *Graphical Methods for Data Analysis*. Duxbury Press (Boston), 1983.

[162] J. Shin, A.S. Whittaker, and D. Cormie. Incident and normally reflected overpressure and impulse for detonations of spherical high explosives in free air. *Journal of Structural Engineering*, 141(12), 2015. doi: 10.1061/(ASCE) ST.1943-541X.0001305.

[163] S.E. Rigby, A. Tyas, S.D. Clarke, S.D. Fay, J.J. Reay, J.A. Warren, M. Gant, and I. Elgy. Observations from preliminary experiments on spatial and temporal pressure measurements from near-field free air explosions. *International Journal of Protective Structures*, 6(2):175–190, 2015. doi: 10.1260/2041-4196.6.2.175.

[164] V. Karlos, G. Solomos, and M. Larcher. Analysis of the blast wave decay coefficient using the Kingery-Bulmash data. *International Journal of Protective Structures*, 7(3):409–429, 2016. doi: 10.1177/2041419616659572.

[165] E. Gogou. Use of high strength steel grades for economical bridge design. Master's thesis, TU - Delft, 2012.

This page intentionally left blank.

Appendix A

Dynamic test results

A.1 Results at room temperature

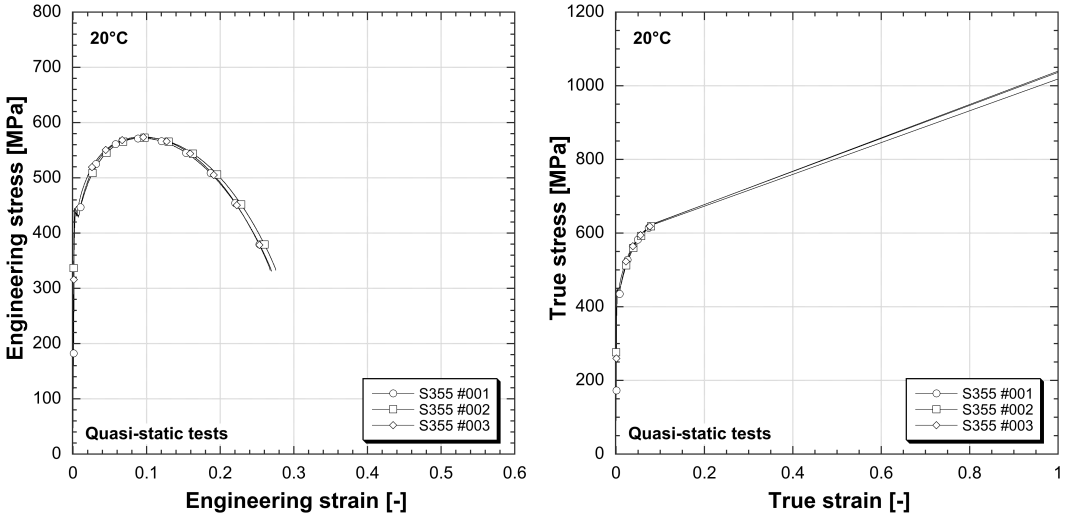

(a) Engineering stress-strain curves (b) True stress-strain curves

Fig. A.1 Results in quasi-static conditions (20 °C)

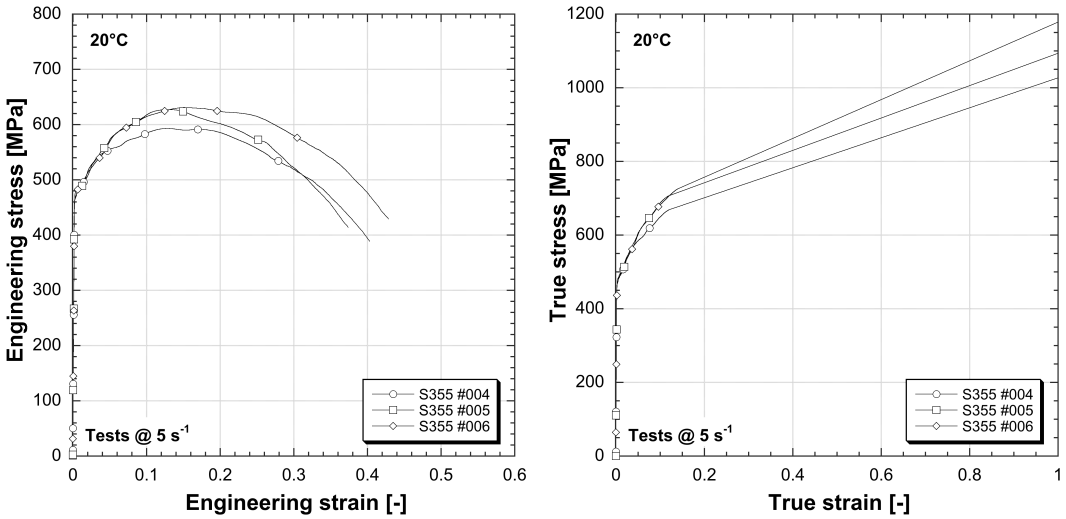

(a) Engineering stress-strain curves (b) True stress-strain curves

Fig. A.2 Results at $5\,s^{-1}$ (20 °C)

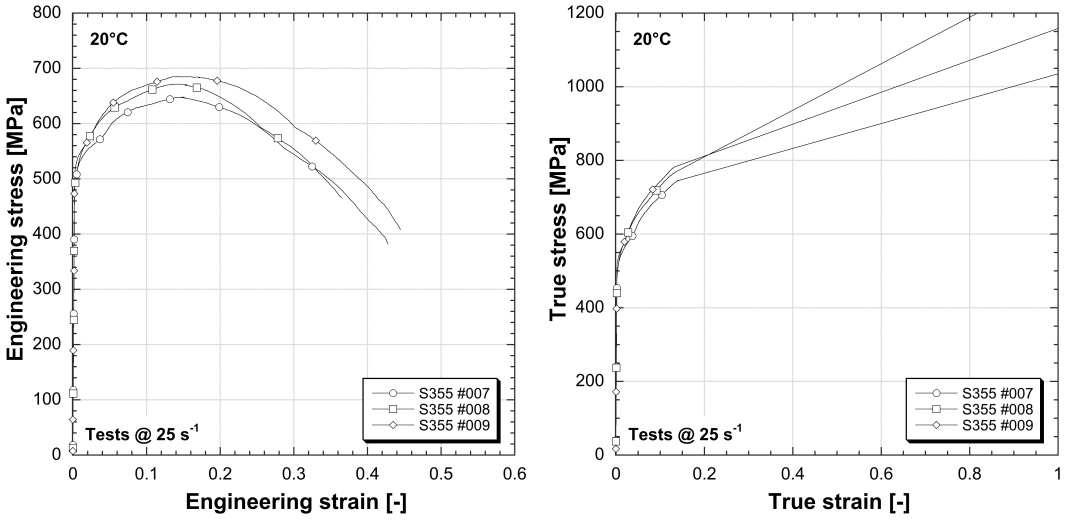

(a) Engineering stress-strain curves (b) True stress-strain curves

Fig. A.3 Results at $25\,\mathrm{s}^{-1}$ (20 °C)

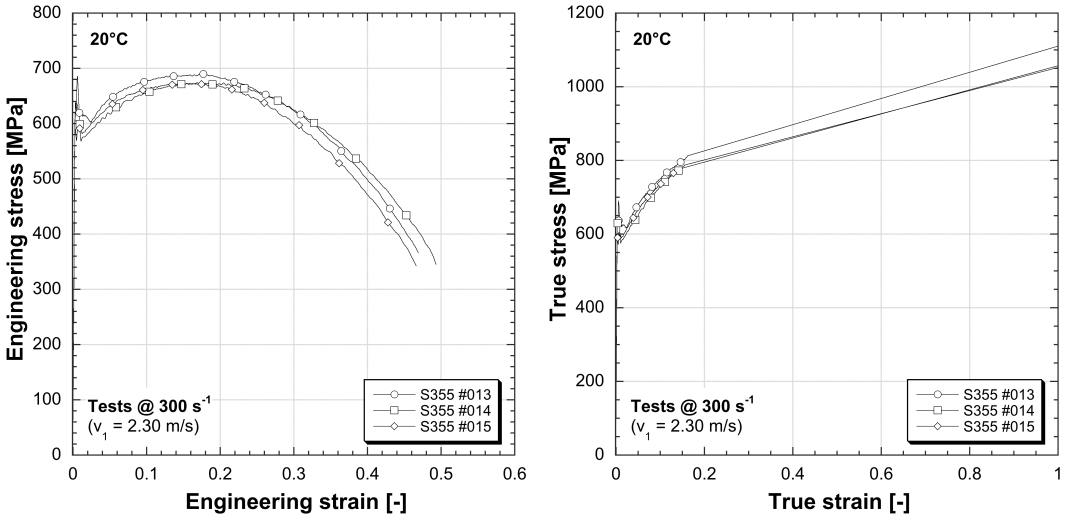

(a) Engineering stress-strain curves (b) True stress-strain curves

Fig. A.4 Results at $300\,\mathrm{s}^{-1}$ (20 °C)

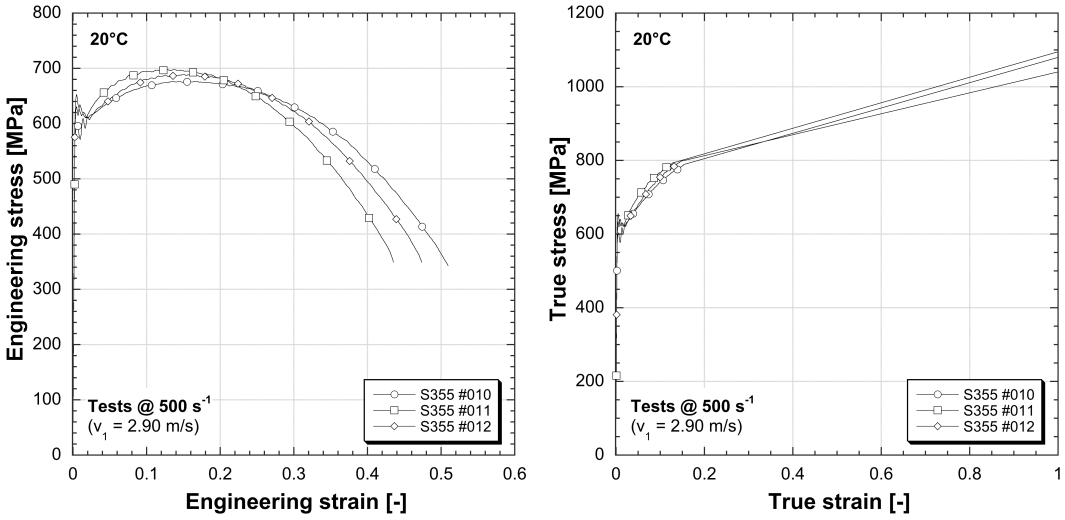

(a) Engineering stress-strain curves (b) True stress-strain curves

Fig. A.5 Results at $500\,\mathrm{s}^{-1}$ (20 °C)

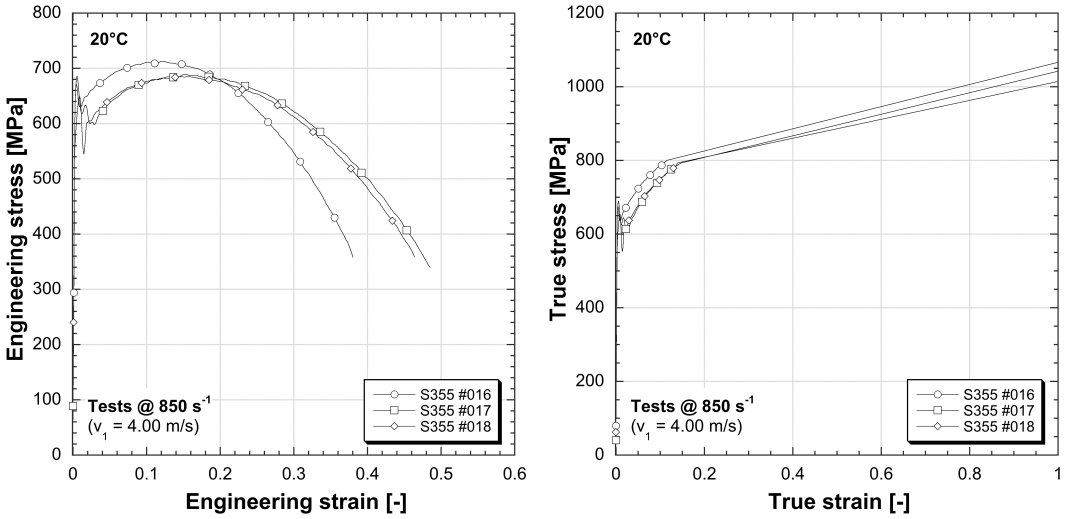

(a) Engineering stress-strain curves (b) True stress-strain curves

Fig. A.6 Results at $850\,\mathrm{s}^{-1}$ (20 °C)

Strain rate, $\dot{\varepsilon}$ (s^{-1})	0.001	5	25	300	500	850
Reduction of area, Z (%)	79 ± 0.3	75 ± 0.2	74 ± 0.4	76 ± 0.3	76 ± 0.9	75 ± 0.4
Upper yield strength, $f_{y,up}$ (MPa)	n.r.	n.r.	n.r.	741 ± 175	628 ± 27	668 ± 18
Lower yield strength, $f_{y,low}$ (MPa)	n.r.	n.r.	n.r.	584 ± 17	600 ± 25	591 ± 43
Proof strength, $f_{p,0.2\%}$ (MPa)	441 ± 5	469 ± 13	514 ± 19	614 ± 41	626 ± 28	653 ± 44
Eff. yield strength, $f_{y,0.5\%}$ (MPa)	437 ± 10	473 ± 12	518 ± 16	617 ± 40	626 ± 26	655 ± 36
Eff. yield strength, $f_{y,1.0\%}$ (MPa)	449 ± 15	488 ± 2	539 ± 8	598 ± 18	609 ± 32	633 ± 3
Eff. yield strength, $f_{y,2.0\%}$ (MPa)	495 ± 8	505 ± 12	566 ± 26	595 ± 15	613 ± 3	624 ± 25
Eff. yield strength, $f_{y,5.0\%}$ (MPa)	554 ± 3	565 ± 9	616 ± 20	631 ± 14	650 ± 14	656 ± 27
Eff. yield strength, $f_{y,10.0\%}$ (MPa)	573 ± 1	605 ± 18	654 ± 19	665 ± 11	680 ± 13	687 ± 21
Eff. yield strength, $f_{y,15.0\%}$ (MPa)	552 ± 3	615 ± 22	668 ± 19	677 ± 9	686 ± 11	693 ± 12
Ultimate tensile strength, f_u (MPa)	573 ± 1	614 ± 32	671 ± 30	679 ± 10	688 ± 11	695 ± 15
Uniform strain, ε_u (%)	9 ± 0.3	13 ± 2	14 ± 0.3	17 ± 1	15 ± 2	14 ± 2
Fracture strength, f_f (MPa)	332 ± 1	404 ± 32	423 ± 60	351 ± 13	347 ± 4	352 ± 11
Fracture strain, ε_f (%)	27 ± 0.4	40 ± 3	41 ± 4	48 ± 2	47 ± 4	44 ± 6
True fracture strength, $f_{f,true}$ (MPa)	1270 ± 19	1261 ± 97	1269 ± 102	1217 ± 42	1218 ± 55	1147 ± 37
True fracture strain, $\varepsilon_{f,true}$ (%)	1.54 ± 0.02	1.35 ± 0.02	1.35 ± 0.02	1.43 ± 0.01	1.45 ± 0.04	1.38 ± 0.01
Strain energy, U_y (MJ/m^3)	0.5 ± 0.01	0.5 ± 0.03	0.6 ± 0.05	0.9 ± 0.12	0.9 ± 0.08	1.0 ± 0.13
Strain energy, U_u (MJ/m^3)	49 ± 2	71 ± 10	89 ± 2	107 ± 8	101 ± 9	95 ± 10
Strain energy, U_f (MJ/m^3)	1423 ± 25	1275 ± 83	1363 ± 129	1410 ± 73	1393 ± 41	1301 ± 43
Avg. strain rate, $\varepsilon_{avg.}$ (s^{-1})	n.r.	4.7 ± 0.4	39 ± 2	289 ± 21	495 ± 49	797 ± 98

Table A.1 Experimental results at room temperature.

A.2 Results at high temperatures

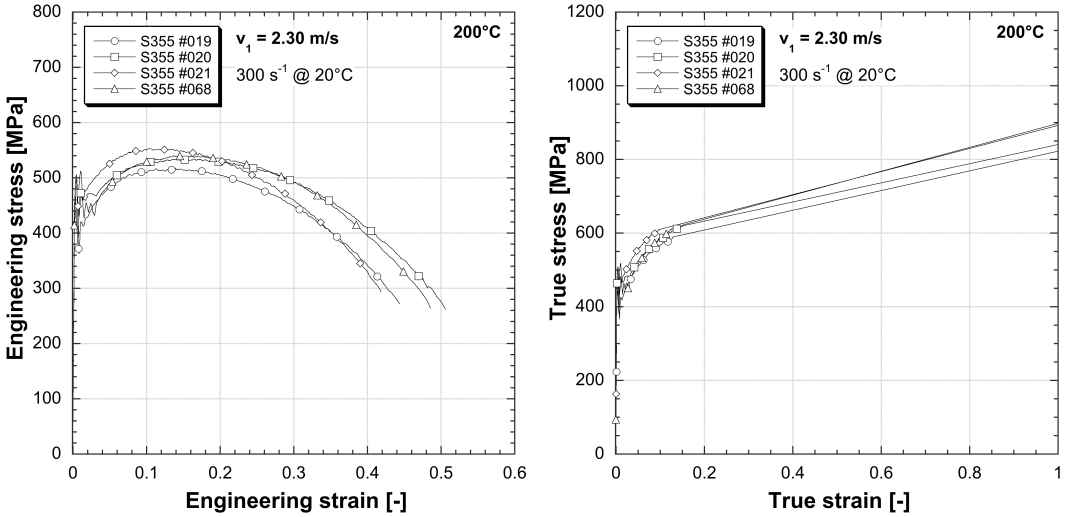

(a) Engineering stress-strain curves (b) True stress-strain curves

Fig. A.7 Results for preloading condition v_1 (200 °C)

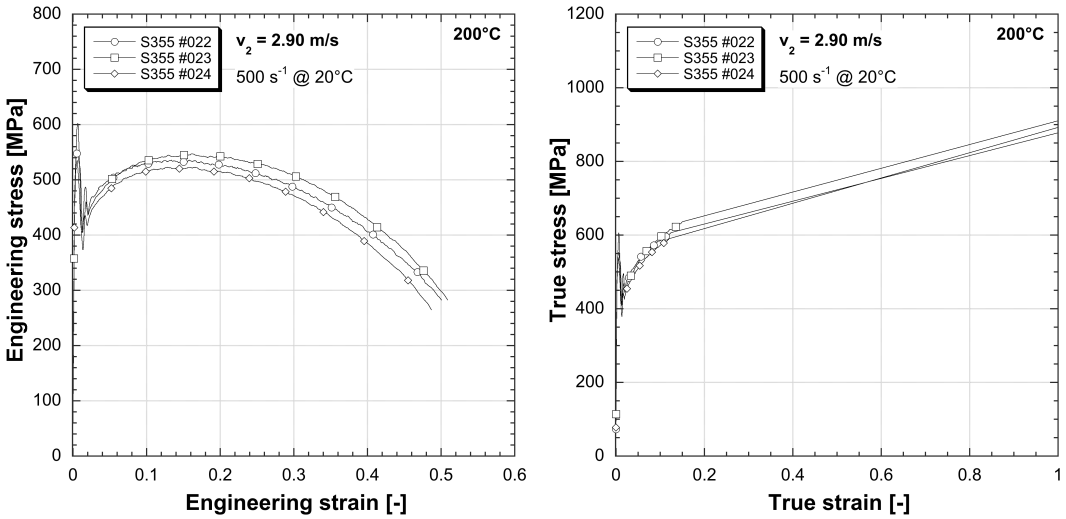

(a) Engineering stress-strain curves (b) True stress-strain curves

Fig. A.8 Results for preloading condition v_2 (200 °C)

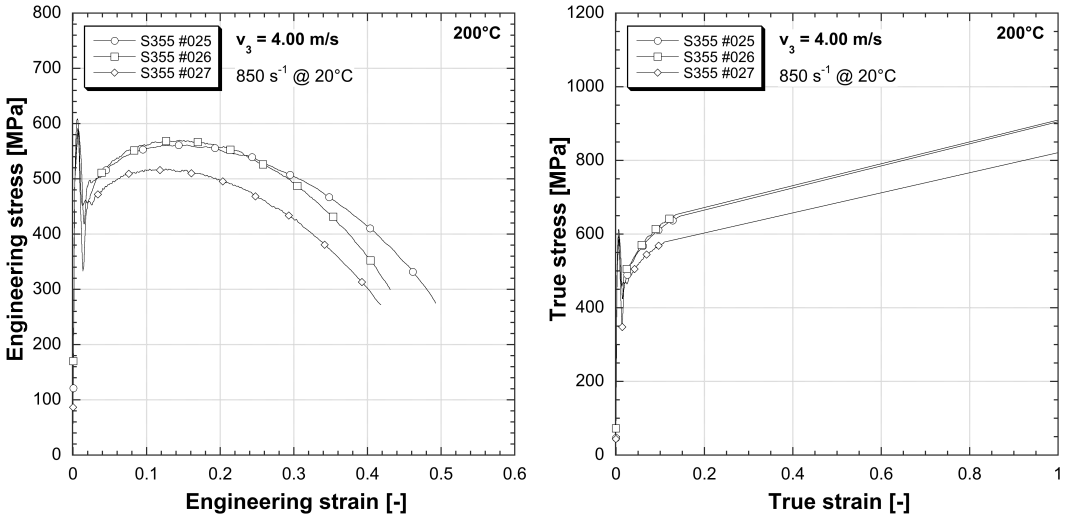

(a) Engineering stress-strain curves (b) True stress-strain curves

Fig. A.9 Results for preloading condition v_3 (200 °C)

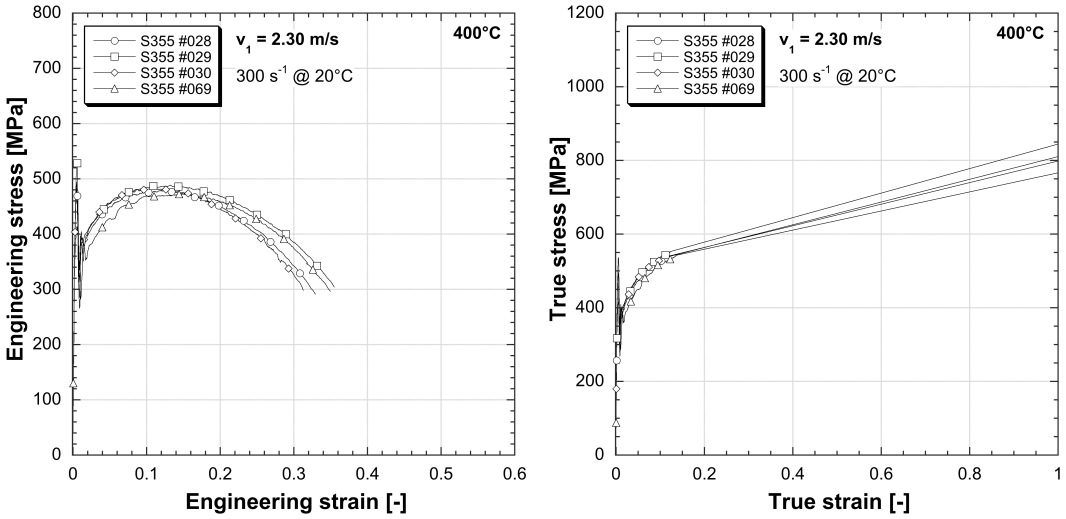

(a) Engineering stress-strain curves (b) True stress-strain curves

Fig. A.10 Results for preloading condition v_1 (400 °C)

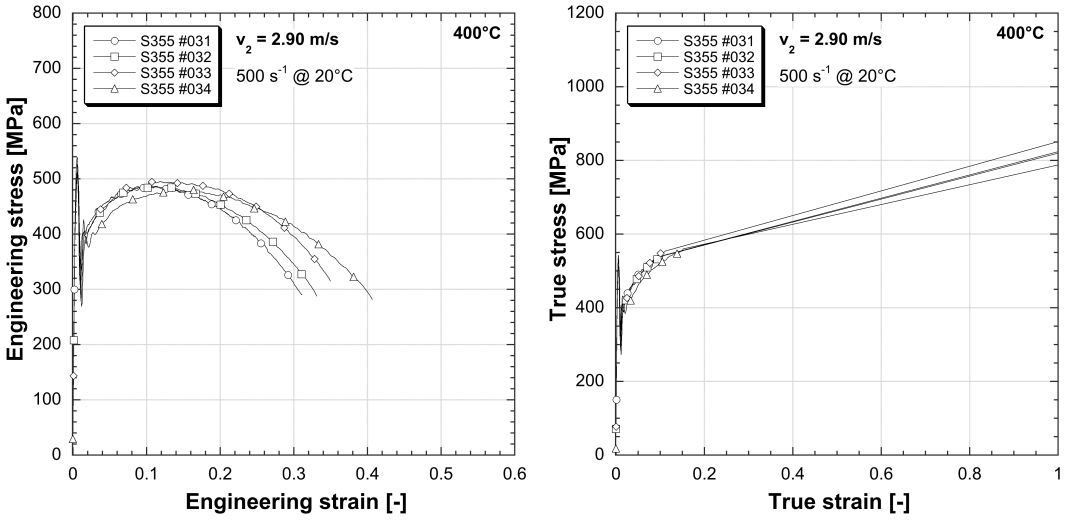

(a) Engineering stress-strain curves (b) True stress-strain curves

Fig. A.11 Results for preloading condition v_2 (400 °C)

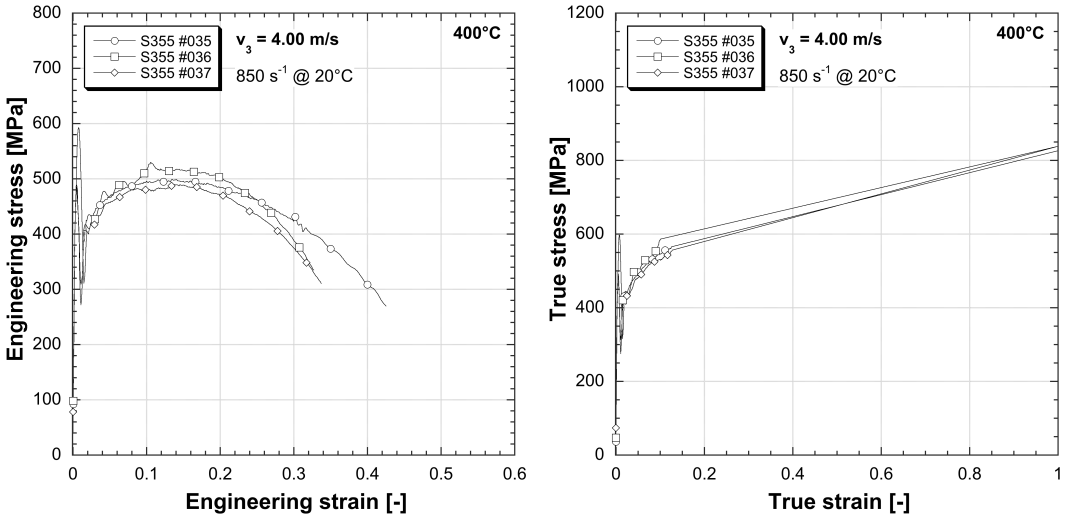

(a) Engineering stress-strain curves (b) True stress-strain curves

Fig. A.12 Results for preloading condition v_3 (400 °C)

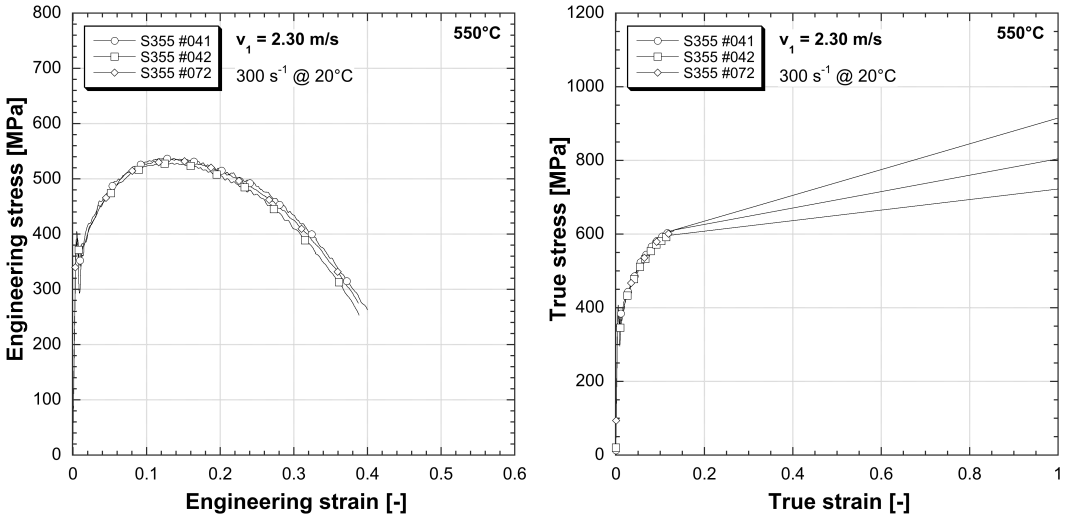

(a) Engineering stress-strain curves (b) True stress-strain curves

Fig. A.13 Results for preloading condition v_1 (550 °C)

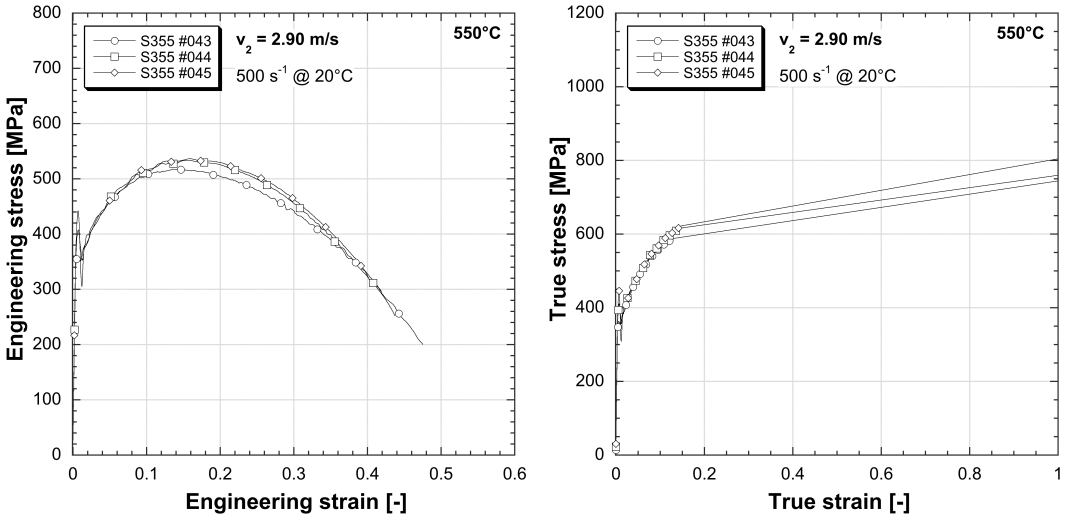

(a) Engineering stress-strain curves (b) True stress-strain curves

Fig. A.14 Results for preloading condition v_2 (550 °C)

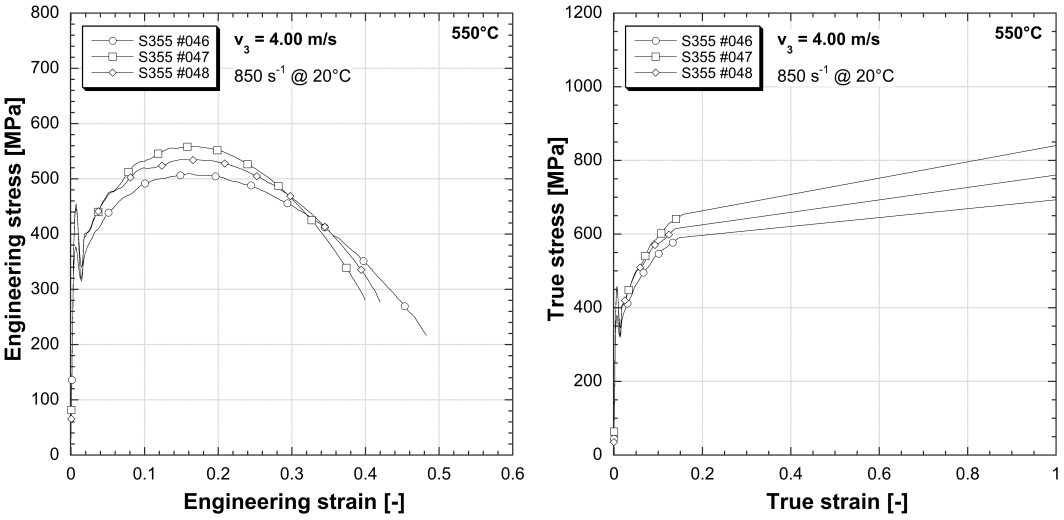

(a) Engineering stress-strain curves (b) True stress-strain curves

Fig. A.15 Results for preloading condition v_3 (550 °C)

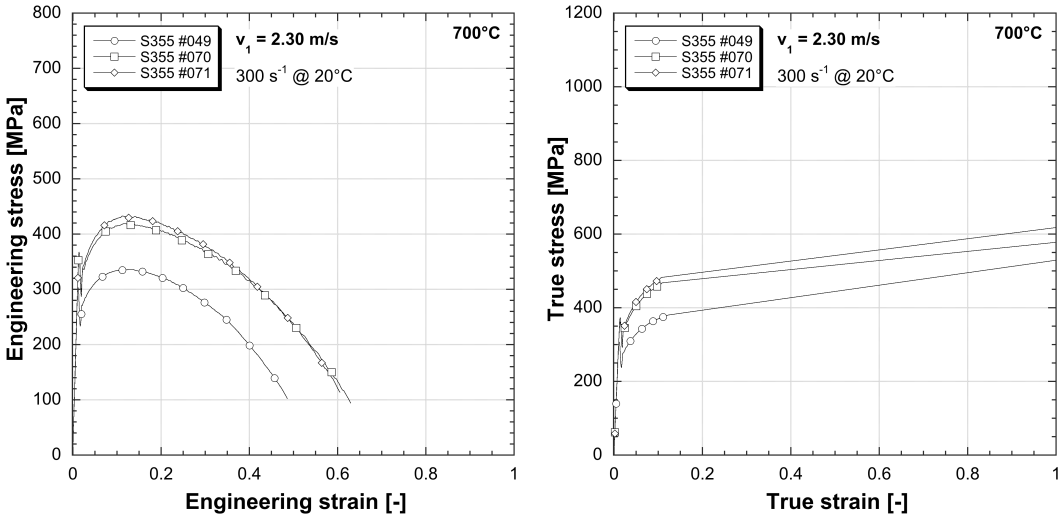

(a) Engineering stress-strain curves (b) True stress-strain curves

Fig. A.16 Results for preloading condition v_1 (700 °C)

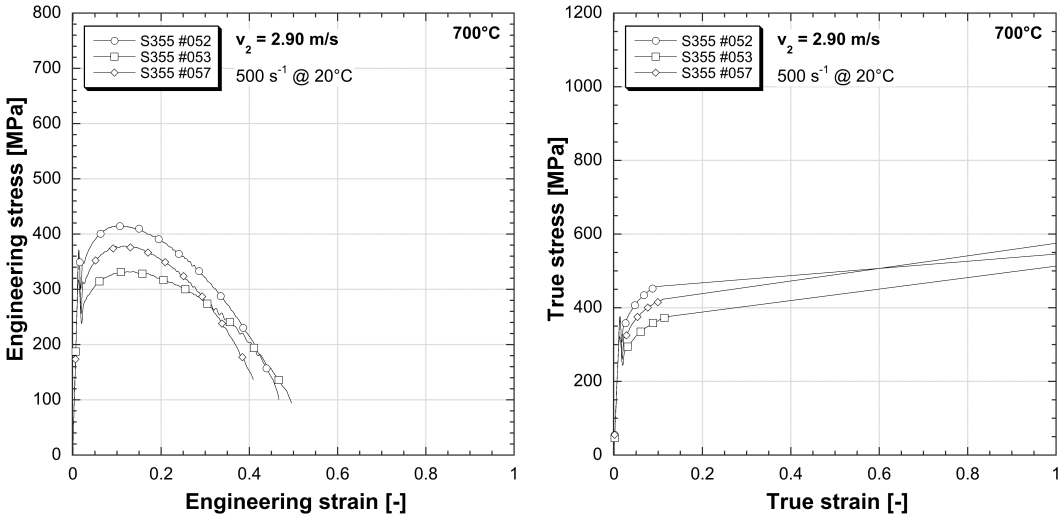

(a) Engineering stress-strain curves (b) True stress-strain curves

Fig. A.17 Results for preloading condition v_2 (700 °C)

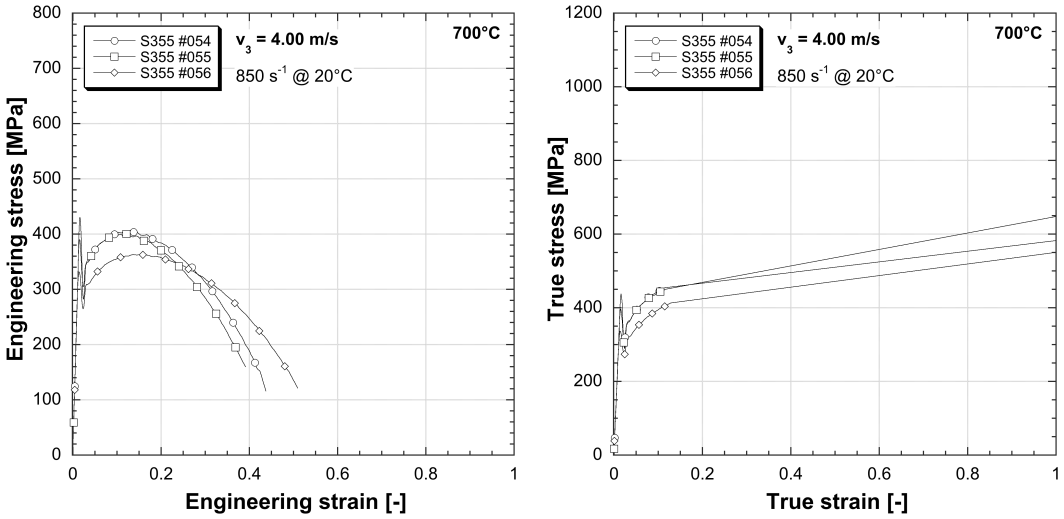

(a) Engineering stress-strain curves (b) True stress-strain curves

Fig. A.18 Results for preloading condition v_3 (700 °C)

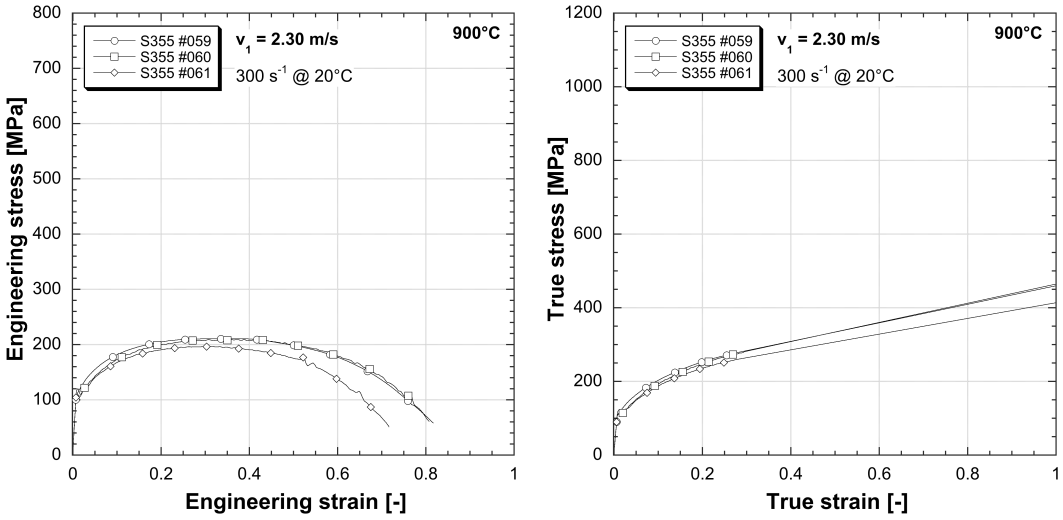

(a) Engineering stress-strain curves (b) True stress-strain curves

Fig. A.19 Results for preloading condition v_1 (900 °C)

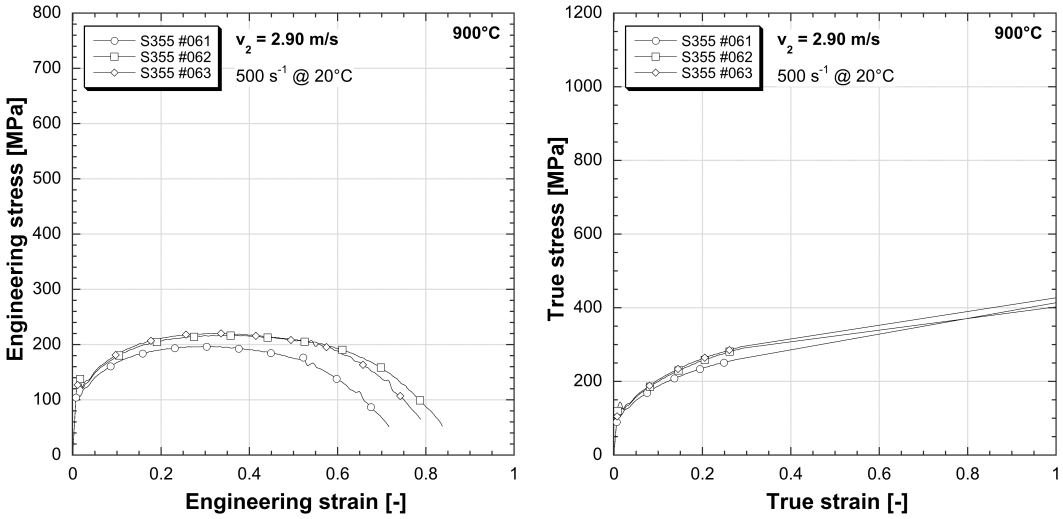

(a) Engineering stress-strain curves (b) True stress-strain curves

Fig. A.20 Results for preloading condition v_2 (900 °C)

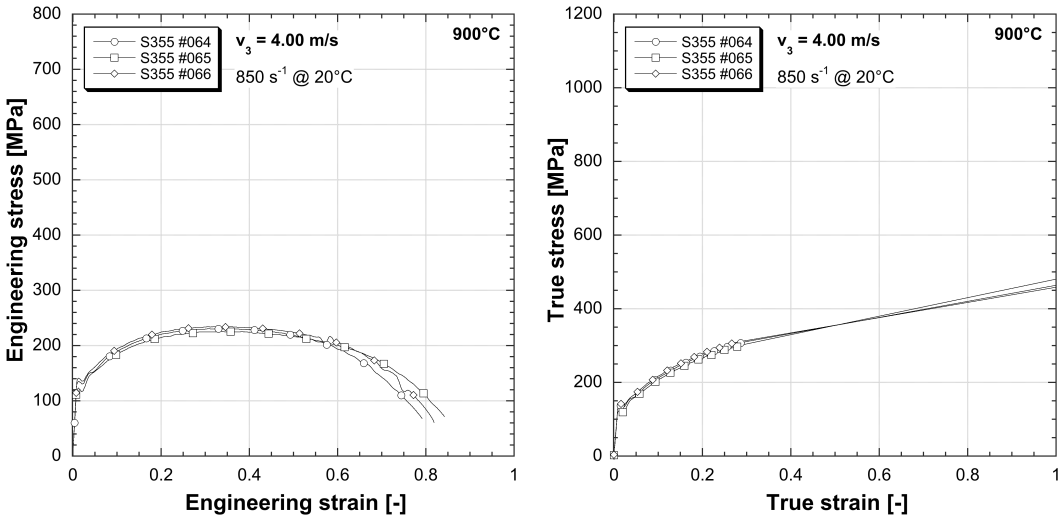

(a) Engineering stress-strain curves (b) True stress-strain curves

Fig. A.21 Results for preloading condition v_3 (900 °C)

Temperature, T (°C)	200	400	550	700	900
Reduction of area, Z (%)	78 ± 2	73 ± 2	76 ± 4	88 ± 1	95 ± 1
Upper yield strength, $f_{y,up}$ (MPa)	493 ± 19	471 ± 45	387 ± 13	339 ± 34	110 ± 7
Lower yield strength, $f_{y,low}$ (MPa)	400 ± 32	309 ± 26	350 ± 25	285 ± 29	108 ± 6
Proof strength, $f_{p,0.2\%}$ (MPa)	473 ± 34	476 ± 52	392 ± 5	338 ± 32	110 ± 8
Eff. yield strength, $f_{y,0.5\%}$ (MPa)	466 ± 37	476 ± 47	391 ± 12	145 ± 6	71 ± 1
Eff. yield strength, $f_{y,1.0\%}$ (MPa)	465 ± 40	329 ± 48	341 ± 25	286 ± 4	111 ± 7
Eff. yield strength, $f_{y,2.0\%}$ (MPa)	465 ± 24	392 ± 18	405 ± 8	297 ± 23	120 ± 7
Eff. yield strength, $f_{y,5.0\%}$ (MPa)	498 ± 19	477 ± 13	476 ± 4	362 ± 10	150 ± 7
Eff. yield strength, $f_{y,10.0\%}$ (MPa)	528 ± 17	477 ± 6	526 ± 4	392 ± 51	179 ± 5
Eff. yield strength, $f_{y,15.0\%}$ (MPa)	533 ± 14	476 ± 6	531 ± 5	393 ± 53	195 ± 5
Ultimate tensile strength, f_u (MPa)	536 ± 16	481 ± 6	534 ± 5	396 ± 52	211 ± 2
Uniform strain, ε_u (%)	14 ± 2	13 ± 2	13 ± 1	12 ± 1	32 ± 3
Fracture strength, f_f (MPa)	272 ± 15	297 ± 5	264 ± 11	103 ± 10	59 ± 2
Fracture strain, ε_f (%)	46 ± 4	34 ± 2	39 ± 1	57 ± 8	78 ± 5
True fracture strength, $f_{f,true}$ (MPa)	1.53 ± 0.09	1.31 ± 0.07	1.44 ± 0.18	2.14 ± 0.11	2.96 ± 0.09
True fracture strain, $\varepsilon_{f,true}$ (-)	1017 ± 72	926 ± 29	931 ± 191	714 ± 18	914 ± 111
Strain energy, U_y (MJ/m^3)	0.6 ± 0.08	0.8 ± 0.10	0.8 ± 0.01	2.1 ± 0.39	0.43 ± 0.06
Strain energy, U_u (MJ/m^3)	68 ± 12	57 ± 6	63 ± 4	41 ± 2	59 ± 5
Strain energy, U_f (MJ/m^3)	1206 ± 124	961 ± 37	929 ± 70	1205 ± 75	1665 ± 195
Avg. strain rate, $\varepsilon_{avg.}$ (s^{-1})	397 ± 12	393 ± 29	367 ± 13	476 ± 16	576 ± 45

Table A.2 Averaged experimental results ($\dot{\varepsilon}^* = 300\,\mathrm{s}^{-1}$ at 20°C)

Temperature, T (°C)	200	400	550	700	900
Reduction of area, Z (%)	79 ± 2	74 ± 1	76 ± 5	87 ± 2	94 ± 1
Upper yield strength, $f_{y,up}$ (MPa)	556 ± 33	511 ± 17	394 ± 39	347 ± 29	125 ± 16
Lower yield strength, $f_{y,low}$ (MPa)	394 ± 21	325 ± 20	360 ± 19	300 ± 40	121 ± 11
Proof strength, $f_{p,0.2\%}$ (MPa)	546 ± 22	518 ± 20	401 ± 41	343 ± 22	124 ± 15
Eff. yield strength, $f_{y,0.5\%}$ (MPa)	557 ± 28	515 ± 23	390 ± 35	148 ± 3	74 ± 2
Eff. yield strength, $f_{y,1.0\%}$ (MPa)	471 ± 38	319 ± 24	355 ± 24	291 ± 9	123 ± 14
Eff. yield strength, $f_{y,2.0\%}$ (MPa)	432 ± 7	399 ± 15	390 ± 8	277 ± 45	119 ± 7
Eff. yield strength, $f_{y,5.0\%}$ (MPa)	494 ± 10	453 ± 12	461 ± 4	348 ± 42	147 ± 6
Eff. yield strength, $f_{y,10.0\%}$ (MPa)	526 ± 10	481 ± 8	512 ± 6	373 ± 43	176 ± 8
Eff. yield strength, $f_{y,15.0\%}$ (MPa)	532 ± 12	481 ± 8	527 ± 11	371 ± 41	193 ± 12
Ultimate tensile strength, f_u (MPa)	535 ± 12	487 ± 6	529 ± 11	375 ± 42	211 ± 13
Uniform strain, ε_u (%)	14 ± 2	13 ± 3	15 ± 1	12 ± 2	33 ± 1
Fracture strength, f_f (MPa)	276 ± 11	294 ± 15	250 ± 48	110 ± 23	56 ± 8
Fracture strain, ε_f (%)	50 ± 1	35 ± 4	44 ± 3	46 ± 5	78 ± 6
True fracture strength, $f_{f,true}$ (MPa)	1.55 ± 0.07	1.43 ± 0.03	1.44 ± 0.23	2.05 ± 0.16	2.83 ± 0.17
True fracture strain, $\varepsilon_{f,true}$ (-)	1072 ± 42	927 ± 30	860 ± 38	692 ± 38	758 ± 81
Strain energy, U_y (MJ/m^3)	0.8 ± 0.06	0.9 ± 0.07	0.8 ± 0.17	2.2 ± 0.28	0.6 ± 0.13
Strain energy, U_u (MJ/m^3)	71 ± 11	58 ± 12	71 ± 7	39 ± 2	60 ± 5
Strain energy, U_f (MJ/m^3)	1263 ± 87	960 ± 22	924 ± 54	1116 ± 55	1295 ± 16
Avg. strain rate, $\varepsilon_{avg.}$ (s^{-1})	632 ± 12	571 ± 70	596 ± 23	604 ± 48	785 ± 16

Table A.3 Averaged experimental results ($\dot{\varepsilon}^* = 500\,\mathrm{s}^{-1}$ at 20°C)

Temperature, T (°C)	200	400	550	700	900
Reduction of area, Z (%)	77 ± 1	73 ± 4	74 ± 2	86 ± 1	94 ± 1
Upper yield strength, $f_{y,up}$ (MPa)	583 ± 17	501 ± 65	422 ± 45	374 ± 43	132 ± 9
Lower yield strength, $f_{y,low}$ (MPa)	408 ± 54	316 ± 24	341 ± 14	331 ± 28	130 ± 9
Proof strength, $f_{p,0.2\%}$ (MPa)	566 ± 29	508 ± 39	423 ± 44	381 ± 46	131 ± 10
Eff. yield strength, $f_{y,0.5\%}$ (MPa)	578 ± 28	494 ± 14	413 ± 39	146 ± 13	74 ± 2
Eff. yield strength, $f_{y,1.0\%}$ (MPa)	494 ± 59	383 ± 132	377 ± 32	285 ± 8	130 ± 9
Eff. yield strength, $f_{y,2.0\%}$ (MPa)	466 ± 18	415 ± 15	389 ± 19	324 ± 32	128 ± 10
Eff. yield strength, $f_{y,5.0\%}$ (MPa)	514 ± 20	464 ± 6	460 ± 19	356 ± 27	156 ± 4
Eff. yield strength, $f_{y,10.0\%}$ (MPa)	543 ± 25	497 ± 17	514 ± 21	385 ± 26	189 ± 5
Eff. yield strength, $f_{y,15.0\%}$ (MPa)	548 ± 30	500 ± 14	533 ± 25	385 ± 20	208 ± 5
Ultimate tensile strength, f_u (MPa)	550 ± 28	506 ± 21	534 ± 25	389 ± 23	230 ± 4
Uniform strain, ε_u (%)	14 ± 2	13 ± 1	16 ± 1	13 ± 1	34 ± 2
Fracture strength, f_f (MPa)	282 ± 15	305 ± 33	258 ± 36	132 ± 24	67 ± 6
Fracture strain, ε_f (%)	45 ± 4	36 ± 5	43 ± 4	45 ± 6	82 ± 3
True fracture strength, $f_{f,true}$ (MPa)	1.55 ± 0.07	1.43 ± 0.03	1.44 ± 0.23	2.05 ± 0.16	2.83 ± 0.17
True fracture strain, $\varepsilon_{f,true}$ (-)	1072 ± 42	927 ± 30	860 ± 38	692 ± 38	758 ± 81
Strain energy, U_y (MJ/m^3)	0.9 ± 0.09	0.9 ± 0.14	0.9 ± 0.19	2.7 ± 0.64	0.6 ± 0.09
Strain energy, U_u (MJ/m^3)	1187 ± 89	884 ± 72	957 ± 103	1142 ± 64	1520 ± 58
Strain energy, U_f (MJ/m^3)	1019 ± 37	930 ± 43	827 ± 94	759 ± 68	866 ± 51
Avg. strain rate, $\varepsilon_{avg.}$ (s^{-1})	904 ± 44	872 ± 90	934 ± 64	967 ± 76	1120 ± 6

Table A.4 Averaged experimental results ($\dot{\varepsilon}^* = 850\,\mathrm{s}^{-1}$ at 20°C)